Use Authorization

In presenting this dissertation in partial fulfillment of the requirements for an advanced degree at Idaho State University, I agree that the Library shall make it freely available for inspection. I further state that permission to download and/or print my dissertation for scholarly purposes may be granted by the Dean of the Graduate School, Dean of my academic division, or by the University Librarian. It is understood that any copying or publication of this dissertation for financial gain shall not be allowed without my written permission.

Signature ________________________

Date ________________________

AN EXPERIMENTAL INVESTIGATION OF NEUTRON-FISSION FRAGMENT CORRELATIONS IN PHOTOFISSION

by

Oleksiy Kosinov

A dissertation

submitted in a partial fulfilment

of the requirenments for the degree of

Doctor of Philosophy in the Department of Physics

Idaho State University

Spring 2016

Committee Approval

To the Graduate Faculty:

The members of the committee appointed to examine the dissertation of Oleksiy Kosinov find it satisfactory and recommend that it be accepted.

Dr. Daniel Dale,
Major Advisor

Dr. Tony Forest,
Committee Member

Dr. Mahbub Khandaker,
Committee Member

Dr. Valeriia Starovoitova,
Committee Member

Dr. Marco Schoen,
Graduate Faculty Represantative

Contents

List of Figures

List of Tables

Abstract

This doctoral dissertation describes an approach to the investigation of the experimental signatures of kinematical correlations between fission fragments and neutrons in photofission. Such correlations are expected to arise due to the unique kinematical features of photofission which are predominantly characterized by binary fission followed by the subsequent emission of neutrons by the fully accelerated fragments.

Key elements of this work include:

- Measurements of two neutron correlations in photofission of uranium.
- The successful construction and testing of a linearly polarized gamma source.
- Measurements of the azimuthal distribution of neutrons in photofission with linearly polarized gammas.

Chapter 1

Overview of neutron-fission fragment correlations in nuclear photofission

1.1 The main properties of the fission process

The nuclear fission process has been explored by many scientists around the world [1, 2]. Since Chadwick's discovery of the neutron in 1932 [3], it was noticed that under neutron irradiation of heavy transuranic nuclei intermediate-mass nuclei were formed and a large amount of energy ($\approx$ 100 MeV) was released. In 1939 Meitner and Frisch suggested that heavy nuclei absorbing neutrons become highly unstable and split (fission) to produce two secondary nuclei with masses of about one half of the mass of the initial nucleus each (binary fission) [4, 5]. There is also a probability to see three fragments in the final state after the fission process, the so called ternary fission process. Two of the fragments created in the process of ternary fission are heavy nuclei with asymmetric masses and the third fragment has small mass and charge in the range $Z \approx 1-18$. However, the probability of this process is lower than 1% with respect to binary fission and decreases even more with the increase of the mass of the third light fragment [6]. In the process called true ternary fission, it is possible to observe decay of a nucleus into three fission fragments of almost equal mass [6]. The probability of true ternary fission is about 10^{-3} with respect to binary fission [7].

The fission process can be understood in the framework of the liquid drop model as a result of the competition between the nuclear attraction forces and Coulombic repulsion forces. The nuclear binding energy can be described by the Weizsacker formula [8]:

$$\begin{aligned} E(N,Z) = a_v(1+\kappa_v I^2)A + a_s(1+\kappa_s I^2)A^{\frac{2}{3}} + ... \\ + c_d Z(Z-1)A^{-\frac{1}{3}} + c_{ex} Z^{\frac{4}{3}} A^{-1} + ... \\ + P(N,Z) + \delta E(N,Z), \end{aligned} \tag{1.1}$$

where $A = N + Z$ and $I = \frac{N-Z}{A}$. The coefficients a_v and a_s are the volume and surface energies, κ_v and κ_s are the asymmetry coefficients, c_d and c_{ex} represent the direct and exchange Coulomb energies, a pairing energy is represented by $P(N,Z)$ which has the relatively small value of around ± 2 MeV, and δE is the shell-correction energy. The binding energy is roughly proportional to A, while the Coulombic repulsion energy is proportional to Z^2 and increases faster than the binding energy. One has to take into account the deformation energy when Eq. (1.1) is applied to the fission process. The deformation energy of a nucleus can be written as:

$$\delta E^{def} = E^{def}(\beta) - E^{def}(\beta = 0), \tag{1.2}$$

where $E^{def}(\beta)$ is the energy at a given deformation and $E^{def}(\beta = 0)$ is the energy of a spherical nucleus when the deformation parameter $\beta = 0$. The deformation energy at a given deformation can be written as a sum of Coulomb and surface terms excluding the volume term because the nuclear matter can be considered as incompressible:

$$E^{def}(\beta) = E_{surf}(\beta) + E_{Coul}(\beta). \tag{1.3}$$

Using these terms, $E_{surf}(\beta)$ and $E_{Coul}(\beta)$, it is possible to define the critical parameter or fissility parameter X as:

$$X = \frac{E_{Coul}(0)}{2E_{surf}(0)}, \text{where} \begin{cases} E_{Coul}(0) = \frac{3}{5}\frac{Z^2e^2}{R_0}, R_0 = r_0 A^{\frac{1}{3}} \\ E_{surf}(0) = 4\pi R_0^2 \tau, \tau = \frac{a_s(1+\kappa_s I^2)}{4\pi r_0^2}. \end{cases}$$

Combining the above equations, the fissility parameter can be written as $X = \frac{(Z^2/A)}{(Z^2/A)_{crit}}$. If one uses the empirical values for the constants $a_s \simeq 18$ MeV and $\kappa_s \simeq -2.5$, then the fissility condition can be presented as:

$$\left(\frac{Z^2}{A}\right)_{crit} \approx 45 - 50. \tag{1.4}$$

In the current representation it is convenient to represent the radius of a nucleus as a multipole expansion of the deformed surface that is a function of the polar and azimuthal angles θ and ϕ:

$$R(\theta, \phi) = R_0 \left[1 + \sum_{\lambda,\mu} a_{\lambda,\mu} Y_{\lambda,\mu}(\theta, \phi)\right], \tag{1.5}$$

where the set $\{a_{\lambda\mu}\}$ represents the set of the possible deformation parameters β. The liquid drop model makes a number of predictions. When $X < 1$, then a nucleus has a spherical configuration which has a stable local minimum (prediction of spherical ground states). When $X > 1$ then the spherical nucleus becomes unstable with respect to quadrupole deformation which means that the unstable nucleus starts spontaneously deforming itself until it reaches the point where it fissions (prediction of spontaneous fission). In the range of values $0.7 \leq X < 1$ the energy of surface deformation has a saddle point. The presence of the saddle point with positive energy E_f with respect to the ground state energy means that there is a fission barrier with height E_f. However, the liquid drop model does not predict the right shape of the potential barrier and does not explain the existence of the fission isomers. Also, this model does not explain the asymmetric mass of fission fragments created in fission nor does it explain the ground state deformations. In order to be able to explain the above mentioned effects, one needs to take into account quantum mechanical effects in the context of the shell model of the nucleus.

As a result of the deformation of the fissioning nucleus, the potential energy of the nucleus may increase with the increase of the deformation parameter and have the shape of a barrier (fission barrier), reducing the probability of the fission process. Taking into account the presence of the fission barrier, the nuclear fission process can be considered in the following way. If one thinks of the fission process, *i.e.*, emission of two secondary nuclei, in analogy to α-particle emission in α-decay, then it can be said that heavy nuclei may have different probabilities of the fission barrier penetration depending on their excitation energy. Hence, the fission can occur either spontaneously (naturally) through the penetration of the fission barrier or it can be induced by the process of absorption of a particle [neutrons or photons (real, virtual)]. After a particle has been absorbed, the excited states of the compound nucleus are populated and their energy is high enough to provide fission directly or to make the probability of the barrier penetration higher.

As mentioned above, right after the fission process (the scission point) we have two fission fragments. These fission fragments are in highly deformed excited states [9, p. 541]. Most of the energy of the excited states is stored in the form of excitation energy and deformation energy of the fission fragments and Coulomb energy of mutual repulsion. The repulsion energy can be roughly estimated to be $Z_1 Z_2 e^2/D \approx 210$ MeV, if $Z_1 = 50$, $Z_2 = 44$ and the distance between two fragments is $D = 15$ fm. Because of this repulsion energy the fission fragments move away from each other, gaining velocity and approaching their equilibrium shapes at the same time. At a distance $D = 150$ fm, the value of the Coulomb energy goes down to 21 MeV and the rest of the energy goes to the excitation energy. This Coulomb repulsion energy corresponds to a velocity of the fission fragments of the order of 10^9 $\mathrm{cm \cdot s^{-1}}$. By 10^{-20} s after passing the scission point the fission fragments gain 90% of the maximum value of their kinetic energy.

Each of the fission fragments is neutron rich. The ratio of the neutrons to protons increases with the increase of atomic number A of a nucleus and it is very high for the fission fragments. At a time $\sim 10^{-13}$ s after the moment of scission the fission fragments emit around two to four neutrons [9, p. 542]. According to the US Department of Energy neutron classification, these neutrons are called prompt neutrons and compose over 99% of the total yield of neutrons produced in the fission event [10, p. 29]. The direction of propagation of these neutrons is peaked forward in the laboratory frame in the direction of the initial motion of the fission fragments. It is this correlation between the kinematics of the fission fragment, and that of the neutrons which we seek to study in the present work. In the rest frame of the fission fragments the neutron angular distribution is assumed to be close to isotropic [11] and the modelled prompt neutron energy spectra based on this assumption follow the experimental data (see Fig. 1.1). This fact supports the idea that prompt neutrons are emitted by the accelerated fission fragments after the scission point has been passed. The energy spectrum of prompt neutrons has the form of a Maxwellian distribution. Each neutron carries away around 2 MeV of energy on average.

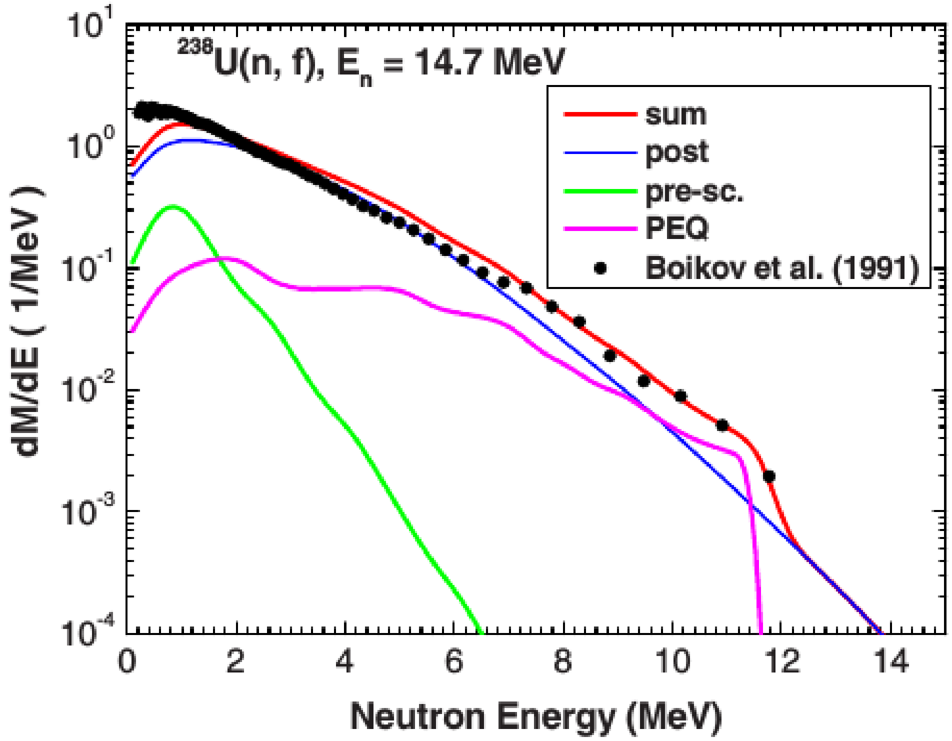

Fig. 1.1. Comparison of the modelled prompt neutron spectrum (red line) and the experimental data (black dots) from [12]. The plot was taken from [11].

At a time of 10^{-11} s, the excitation energy of the fission fragments is below the prompt neutron emission threshold and further deexcitation goes through the emission of gamma rays. Moreover, the fission fragments are still far from the β-stability valley because their charges have not been rearranged yet. So, the stable final end products are formed via the slow (10^{-2} s) β-decay of neutron rich fission products. The process of β-decay may lead to states which are neutron unstable and thus emit delayed neutrons. The yield of delayed neutrons is around 1% of the total neutron yield [13].

1.1.1 The photofission process

Photofission is the process where the energy of the nuclear excitation comes from the interaction of photons with nuclei. The photofission process happens when a photon gets absorbed and its energy is delivered to the whole nucleus. After redistribution of the absorbed energy, it might be energetically favourable to form an unstable nuclear system, the so called compound nucleus, which splits generally into two fission fragments which are nuclei with different masses. If the incident photon breaks a nucleus into its components, the process of photodisintegration takes place. A well known example of this process is the photodisintegration of the deuteron, when in the final state one can observe an unbound neutron and proton.

It has been observed that the cross sections in some photonuclear reactions, such as (γ, n) or photodisintegration and photofission, have a resonance nature in a specific range of energies of the incident photon (see Figs. 1.2 and 1.3). A more detailed plot of the photofission cross section for ^{238}U, including cross sections for (γ, n) and $(\gamma, 2n)$ direct processes, is presented in Fig. 1.4.

The maximum of the cross section of the photofission reaction in the case of uranium is around $E_\gamma = 15$ MeV and it sharply goes to zero above and below the resonance energy. A possible explanation for this is that there was an interplay between the increase in nuclear energy level density and the competition of other

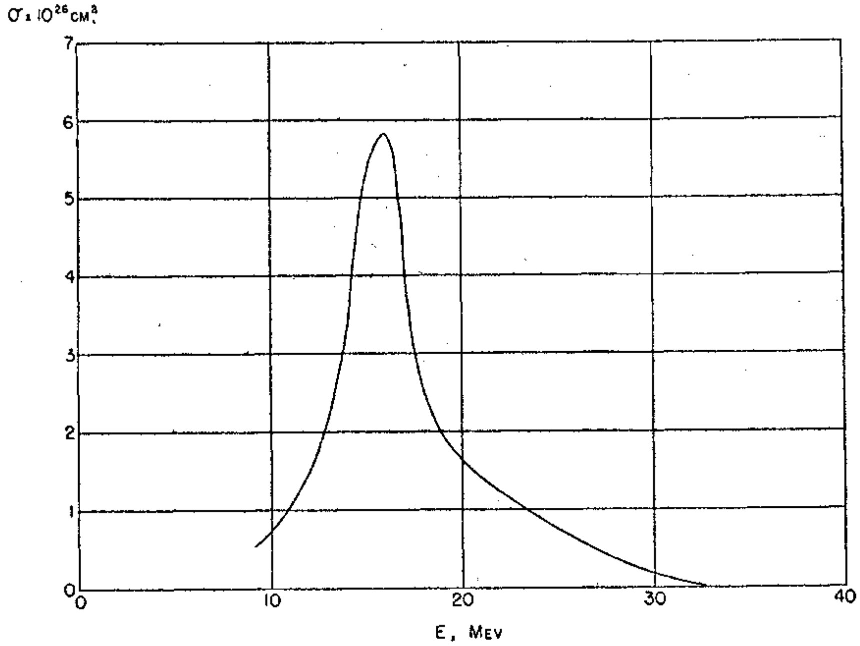

Fig. 1.2. Uranium oxide photofission cross section. The plot was taken from [14].

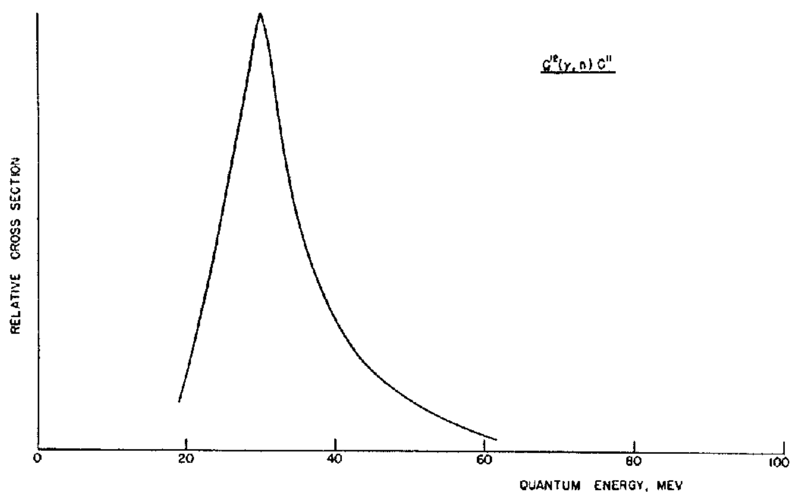

Fig. 1.3. Resonance (γ, n) reaction on ^{12}C. The plot was taken from [15].

possible reaction channels, for instance, $(\gamma, 2n)$ [16]. Goldhaber and Teller in [16] proposed a different explanation for the resonance nature of the photonuclear reactions. They suggested that the incident photons induce motion inside a nucleus in which all the protons oscillate relative to the neutrons. The motion of neutrons is in the opposite direction to the motion of the protons and this effect was called the dipole vibration. This kind of vibration has a resonance nature with peak at relatively high photon energy ($\sim$ 15 MeV) because neutrons and protons are strongly bound and it is necessary to provide high energy radiation to make them vibrate relative to each other. The energy of the dipole vibration can be transferred into other modes of nuclear motion and thus other resonance states are possible to observe.

The width of the giant resonance peak in the Goldhaber-Teller and Steinwedel-Jensen models is attributed to damping effects inside the nucleus [17]. One kind of damping effect takes place as a result of viscous effects originating during the neutron-proton relative motion inside the nucleus. Another kind of damping of the Goldhaber-Teller collective mode happens when the different collective mode components reflect in a different way from the surface of the nucleus, and hence are out of phase. If the inter-particle forces are introduced, then the width of the giant dipole resonance peak is defined by both the coherent part of the nuclear interactions (the viscous and collective mode effects) and by the incoherent part which represents inelastic collisions of neutrons and protons within neutron-proton matter.

1.2 Fission fragment angular distributions

The fission fragment angular distribution can be described in terms of two quantities [2, p. 180]: (a) the incident particle angular momentum and (b) the part of the momentum of the incident particle which is transferred into orbital angular

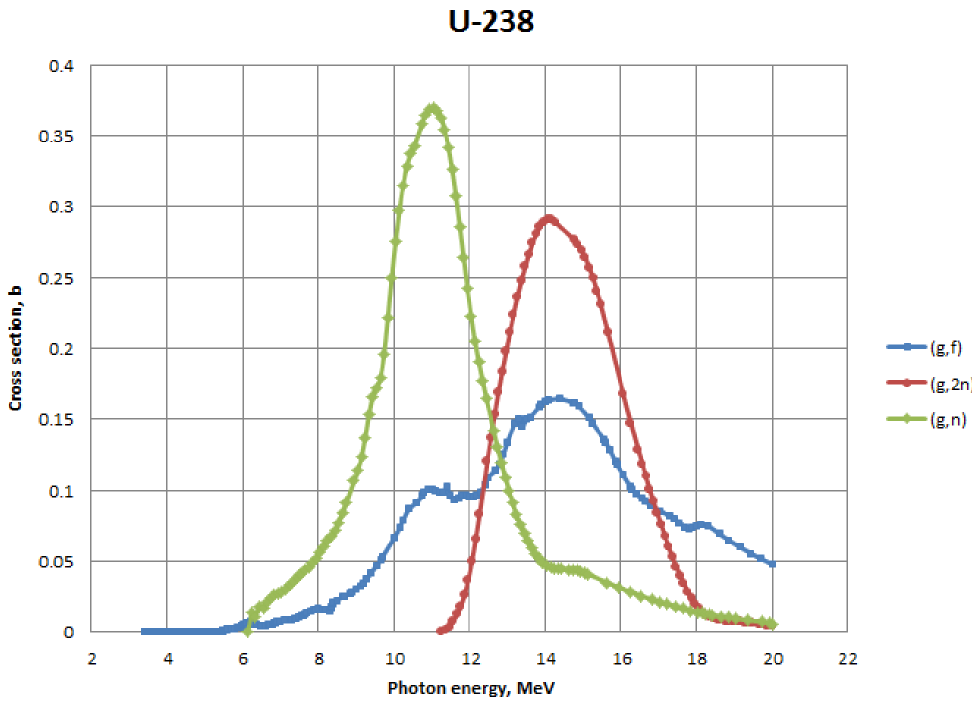

Fig. 1.4. ^{238}U photofission (γ, f) cross section together with (γ, n) and $(\gamma, 2n)$ cross sections as a function of the incident photon energy. Data are from ENDF [18].

momentum of the fission fragments. The latter is defined by the projection of the total angular momentum of the nucleus on its symmetry axis, K.

In order to describe the fragment angular distribution, two assumptions have to be made. The first one is that the fission fragments are separated along the symmetry axis of the nucleus and the second assumption is that although K is not a good quantum number for the transition stage between the original nucleus and the saddle point, it is still a good quantum number after the saddle point was passed because the value(s) of K of the compound nucleus is not related to the K value of the transition nucleus. Taking into account the last two assumptions, it can be said that the angular dependence of the fission fragments' emission from a transitional state described by the quantum numbers J and M is defined uniquely [2, p. 110].

The fission fragment emission probability from a transition state characterized by quantum numbers J, M, and K at a specific angle θ into the conical volume cut by the angular range $d\theta$ is described by [2]:

$$P^J_{M,K}(\theta) = [(2J+1)/4\pi R^2]|d^J_{M,K}(\theta)|^2 \pi R^2 \sin\theta d\theta. \tag{1.6}$$

The probability is normalized such that it is equal to unity if integrated from 0 to π. The functions $d^J_{M,K}(\theta)$ are defined as [2]:

$$\begin{aligned} d^J_{M,K}(\theta) &= \sqrt{(J+M)!\,(J-M)!\,(J+K)!\,(J-K)!} \\ \times \sum_{X=0,1,2,3\ldots} &\frac{(-1)^X [\sin(\theta/2)]^{K-M+2X} [\cos(\theta/2)]^{2J-K+M-2X}}{(J-K-X)!\,(J+M-X)!\,(X+K-M)!\,X!}. \end{aligned} \tag{1.7}$$

The fission fragment angular distribution $W^J_{M,K}(\theta)$ can be obtained by dividing $P^J_{M,K}(\theta)$ by $\sin(\theta)$:

$$W^J_{M,K}(\theta) = [(2J+1)/2]|d^J_{M,K}(\theta)|^2. \tag{1.8}$$

Using the fission fragment angular distribution $W^J_{M,K}(\theta)$, one can calculate the differential cross section of fission fragment emission for the specific channel (J,π,K,M,θ) at angle θ as:

$$\frac{d\sigma_f}{d\Omega}(J,\pi,K,M,\theta) = \frac{W^J_{M,K}(\theta)}{2\pi}\sigma_f(J,\pi,K,M,\theta). \tag{1.9}$$

In the case of photofission of an even-even nucleus, the fission angular anisotropy has simple features. The spin-parity of the ground state of an even-even nucleus is $J^\pi = 0^+$. The main channel of the absorption of photons is the electric dipole absorption and, hence, after the absorption of a photon a compound nucleus is in the state $J^\pi = 1^-$ and $M = \pm 1$. If the excitation energy is not sufficient to break nucleon pairs, the nucleus is subject only to collective excitations. The highly deformed even-even transition nucleus being in the ground state with quadrupole deformation is expected to have $K = 0$ [2]. In this case of the transition state ($J^\pi = 1^-$, $M = \pm 1$, $K = 0$), the fission fragment angular distribution can be expressed as:

$$\begin{aligned} W^{J=1}_{M=\pm 1, K=0}(\theta) = \frac{1}{2}(2J+1)\{&P(J=1, M=+1)|d^1_{1,0}(\theta)|^2 \\ &+P(J=1, M=-1)|d^1_{-1,0}(\theta)|^2\} \\ &= \frac{3}{2}\{\frac{1}{2}|d^1_{1,0}(\theta)|^2 + \frac{1}{2}|d^1_{-1,0}(\theta)|^2\}. \end{aligned} \tag{1.10}$$

After the evaluation of $d^J_{M,K}(\theta)$ functions the angular distribution gives:

$$W^{J=1}_{M=\pm 1, K=0}(\theta) = \frac{3}{4}\sin^2\theta. \tag{1.11}$$

Similar calculation of fission fragment angular distributions for the transition nucleus in the state with $K = 1$ gives the following [2]:

$$W^{J=1}_{M=\pm 1, K=\pm 1}(\theta) = \frac{3}{4} - \frac{3}{8}\sin^2\theta. \tag{1.12}$$

If linearly polarized photons are used to induce fission, the angular distribution of fission fragments is dependent both on the azimuthal angle and the polar angle $W^J_{M,K}(\theta) \to W^J_{M,K}(\theta, \phi)$.

A theoretical prediction of the angular distribution function for fission fragments obtained as a result of photofission of even-even nuclei is given by [1]:

$$W(\theta, \phi) = A_0 + A_2(P_2(\cos\theta) + P_\gamma f_2(1,1)\cos 2\phi P_2^2(\cos\theta)), \tag{1.13}$$

where the coefficients A_0 and A_2 depend on the quantum numbers of the transition state (J, K) and are equal to: $A_0 = 1/2$, $A_2 = -1/2$ for $(1, 0)$ state; $A_0 = 1/2$, $A_2 = 1/4$ for $(1, 1)$ state. P_γ is the polarization degree, $P_2 = \frac{1}{2}(2 - 3\sin 2\theta)$.

A graphical representation of the angular distribution function given by Eq. (1.13) is shown below in Fig. 1.5 for the case of dipole excitation, where the value of the polarization degree was chosen to be 30%.

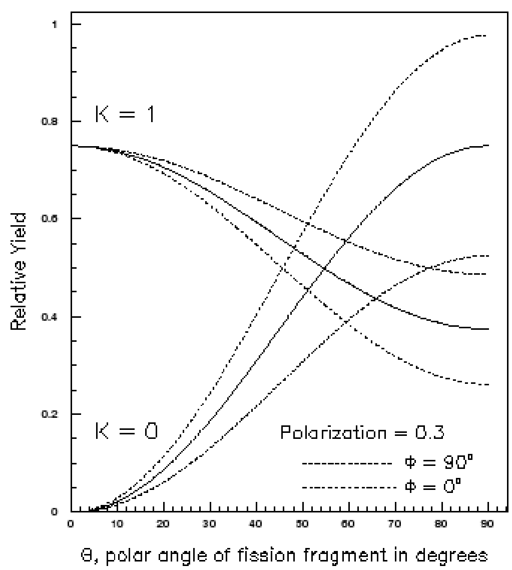

Fig. 1.5. Asymmetry of fission fragments (plotted by [19]).

1.3 Prompt neutrons

While the above discussion refers to the kinematics of the fission fragments, in this section we will consider how the fission fragment angular distribution impacts the angular distribution of the prompt neutrons.

After the scission point has passed, the fission fragments are highly energetic and neutron rich. The energy of the fission fragments may exist in the form of internal energy or deformation energy. The deformation energy is transformed into excitation energy when the fission fragments approach their equilibrium shapes. A part of the energy released in the fission process which was not transferred into kinetic energy of the fission fragments appears in the form of prompt neutron emission. If the fission fragments emit neutrons at a time ($\sim 10^{-13}$ s) longer than the time needed for the fission fragments to reach the full acceleration ($\sim 10^{-20}$ s), the prompt neutron angular distribution will be correlated with the fission fragment angular distribution. Some neutrons can be emitted at a stage when the fission fragments are not fully accelerated [20]. The time of emission of these neutrons, called scission neutrons, is $\sim 10^{-21}$ s. At this stage the fission fragments are assumed to be at rest. The fission fragments at rest will evaporate scission neutrons isotropically. The assumption in this work is that the two neutron angular correlations will not be observed for the scission neutrons. However, there are arguments that the angular distribution of the scission neutrons might not be isotropic [21].

A Monte-Carlo simulation of the azimuthal angular distribution of neutrons emitted by fission fragments is presented in Fig. 1.6. The simulation was done under the following assumptions:

1. the mass of the fission fragment was sampled uniformly in the range $85 < A < 105$ and $130 < A < 150$;

2. a kinetic energy of 175 MeV was shared between the two fission fragments;

3. neutrons were emitted isotropically (in the fission fragment center-of-mass frame) by the fission fragment with the following energy distribution $N(E) = \sqrt{E}e^{-E/0.75}$;

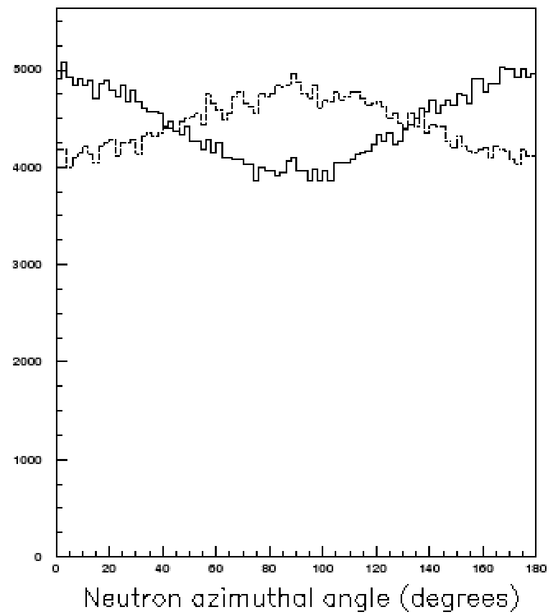

Fig. 1.6. Asymmetry of neutron emission (plotted by [19]). ϕ distribution at $\theta = 90^0$ for K=0 (solid) and K=1 (dashed).

4. the angular distribution of the fission fragments was sampled according to Eq. (1.13);

5. the value of the prompt neutron asymmetry A^{sim} was calculated for the degree of the polarization $P_\gamma = 30\%$.

The value of A^{sim} was defined as a ratio of neutron yields:

$$A^{sim} = \frac{N(\theta = \pi/2, \phi = 0)}{N(\theta = \pi/2, \phi = \pi/2)} \tag{1.14}$$

observed at polar and azimuthal angles $(\theta = \pi/2, \phi = 0)$ and $(\theta = \pi/2, \phi = \pi/2)$. The ratio was equal to 1.25 (pure $K = 0$) and 0.84 (pure $K = 1$) for the ϕ-distribution shown in Fig. 1.6. No neutron energy cut was applied.

During the experiment, a non monoenergetic photon beam with a fixed end point energy was used to induce photofission and, hence, generate fission fragments inside a fissionable target that emitted detectable prompt neutrons. In experiments implementing bremsstrahlung photon beams, it would be hard to separate different fission channels because the fission process may go in parallel through multiple channels which are possible due to the broad energy spectrum of the photons. As a consequence, the prompt neutron angular asymmetries in the experiments performed and described in this paper were averaged over possible channels. Also in the case of the ^{238}U target, there is a chance to produce neutrons directly via the (γ, n) reaction because the energy ranges of (γ, n) and photofission reaction (γ, f) cross sections overlap (see Fig. 1.4). This effect may introduce an additional contamination to the angular asymmetries in the experiments where single neutron rates are observed. In this paper, the angular distribution of the prompt neutrons was investigated and compared to the predicted angular distribution of the fission fragments. According to the simulation, a ϕ asymmetry was expected in the angular distribution of neutrons emitted by fission fragments which were created via polarized photons in the fissionable target. This asymmetry may potentially serve as a signature of the fission event. However, what was obtained is the integral asymmetry. In order to obtain the angular asymmetry for a specific channel and to be able to make direct comparison of the experimental data and the theoretical prediction it will be necessary to develop the technique of deconvolution of the experimental angular distributions. This technique is out of the scope of the current work and will not be discussed in this paper.

Chapter 2

Two neutron correlations in photofission

2.1 Motivation

Information on the kinematics of the post fission products may be useful in many different ways. Some properties such as the angular correlation of the prompt fission neutrons and the prompt gamma rays can provide information on the physics of the fission process near the scission point [22]. Comparison of the neutron multiplicity, *i.e.*, the number of neutrons emitted per fission event obtained in experiments, to a Monte-Carlo model can provide important information on the fission process in general [22–24]. Also, information on the prompt neutrons' energy spectra can improve the quality of the output data obtained via transport simulations of nuclear reactor physics [22].

In the absence of experimental data on the two neutron correlations in the photofission process, one needs to investigate the kinematics of the fission process in order to estimate the angular correlation effect in prompt neutron emission.

As mentioned above, we have an incoming photon beam produced by the interaction of electrons with a bremsstrahlung converter. The end point energy of the bremsstrahlung photons (10.5 MeV in our case) could be adjusted to cover the giant dipole resonance region of the fissionable target. The beam interacts with either a heavy actinide target causing the fission of nuclei during the data production runs or a light water/deuterated water target to tune up the experimental equipment. According to [25, p. 486], in the photofission process we have on average 2.3 neutrons per fission event for most of the fissionable isotopes with an energy distribution described by a Watt spectrum in the fission fragment's center-of-mass [25, p. 493]. Depending on the photon beam properties and the experimental detector setup, one can study different correlation effects in the angular distribution of the prompt neutrons.

2.1.1 Two neutron correlations

The following stages of a nucleus undergoing the fission process can be considered: (a) pre-equilibrium stage, (b) pre-saddle stage, (c) saddle-to-scission stage, (d) near scission stage, (e) post scission stage [11]. At stage (a), the prompt fission neutrons can be emitted at the stage of compound nucleus formation. Stage (b) describes the evaporation of the prompt fission neutrons during the fission chances formation. The fission chance can be considered in the following way. When the neutrons with energy higher than 1 MeV, for instance, interact with a nucleus of ^{238}U and the height of the fission barrier is greater than the energy of neutron separation, the excitation function shown in Fig. 2.1 has a stairstep pattern. The first rise and flat part in the excitation function correspond to the (n, f) reaction, the second rise and flat part in the excitation function correspond

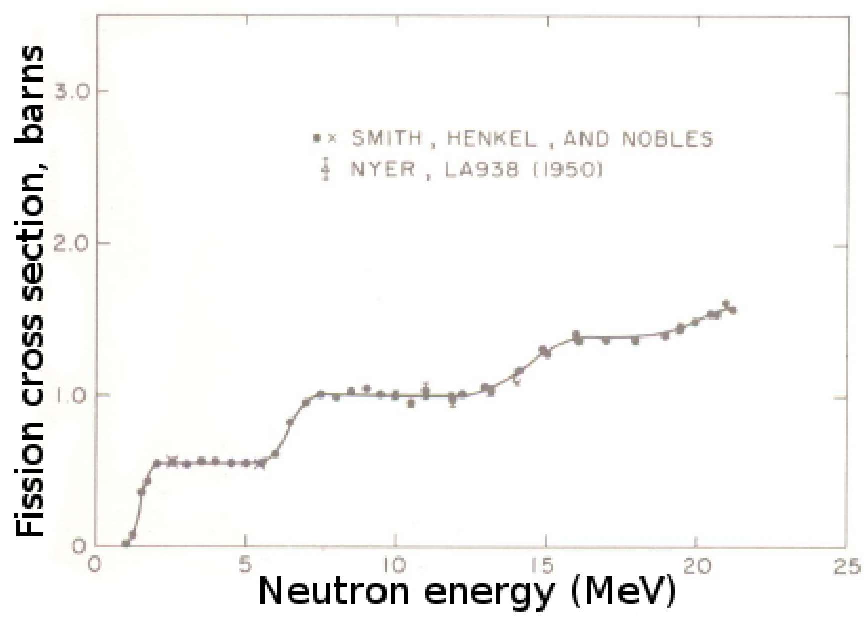

Fig. 2.1. Cross section of neutron induced fission for ^{238}U. Picture was taken from [2].

to the (n, nf) reaction (so-called second-chance fission), the third rise and flat part in the excitation function correspond to the $(n, 2nf)$ reaction (third-chance fission) and so on. With the increase of the energy of incident neutrons the presaddle neutron emission will contribute proportionally to the probability of different fission chances [11]. When the incident neutron energy is greater than 10 MeV the pre-equilibrium emission starts playing an important role.

At stage (c) the prompt fission neutrons are evaporated when the fissioning nucleus is descending from the saddle point to the scission point. At the early moments of the saddle-to-scission transition of a fissioning nucleus, the Coulomb repulsion inside the nucleus is compensated by the nuclear attraction. At this point only a small amount of nucleons are being excited, with the deformation increasing due to weak coupling between collective and intrinsic degrees of freedom [26]. These conditions of equilibrium start breaking down when the fissioning nucleus is close to the scission point. Before the fissioning nucleus reaches the scission point, the two fission fragments are joined by a neck that is composed of a nuclear matter.

At stage (d) the emission of the prompt neutrons happens when the fissioning nucleus undergoes rapid dynamical changes around the scission point. At the scission point, the neck joining the fission fragments ruptures. The fission fragments absorb the remaining parts of the neck. At this moment the nucleons inside the fission fragments are highly excited and there is the possibility for the emission of the nucleons from the not yet fully accelerated, due to the Coulomb repulsion, fission fragments. Shortly after [$\sim 10^{-13}$ s, the last stage (e)], when the fragments are fully accelerated and still highly excited, there are chances for the emission of prompt neutrons. The prompt fission neutrons are emitted from the moving fission fragments which can be described in terms of a temperature.

According to kinematic considerations, the neutrons emitted at the scission point are isotropic while the prompt neutrons emitted from the fully accelerated fission fragments are anisotropic and are emitted preferentially along the momentum of the fission fragments. According to the energy balance, the scission nucleons should be the major particles emitted in the fission process.

In the photofission process, it is possible that each fission fragment emits one prompt neutron per fission or only one fission fragment emits two neutrons and the other fission fragment does not emit any prompt neutrons. The kinematics of the fission process described above implies that the opening angle between two prompt neutrons should have some asymmetry depending on the relative direction of emission of the two neutrons with respect to the fission fragment momentum. Special care should be taken about accidental two-neutron coincidences in the study of two neutron angular correlations. The end point energy of the bremsstrahlung photon spectrum has to be set to a value which does not allow the direct $(\gamma, 2n)$ reaction in which the correlation is washed out. Also cross talk between neighbouring neutron detectors should be avoided by constructing appropriate neutron shielding around the detectors.

2.1.2 Fissile material signature in photofission reaction

Fissile material can be potentially detected using data on the two neutron opening angle asymmetry produced in the process of photofission with unpolarized photons. Also, fissile material can potentially be detected by observing the angular asymmetry of the prompt neutrons created in the photofission process initiated by the polarized photon beam. While such applications may be developed in the future, the goal of the present work is to establish and quantify the potential physical signatures of such correlations.

2.2 Past work on two neutron correlations

As previously mentioned, in order to understand the physics of the photofission process one needs to investigate all possible stages of the process. Many new predictions can be made based on the fission kinematics. Prompt neutrons and photons may reveal important information on the fission process around the scission point [22]. In particular, the experimental observation of n-n angular correlations of prompt neutrons can be a sign that the prompt neutrons are mostly emitted after the scission point has been passed, and the two fully accelerated fission fragments have been created.

One such experiment [27] investigated the n-n correlations of prompt neutrons produced in the process of spontaneous fission of ^{252}Cf. An advantage of the n-n correlation experiments is that there is no need to detect the fission fragments, and the fissionable target or the source may be thick enough to absorb the fission fragments. However, in this case the observed opening angle between the prompt neutrons is averaged over the orientation of the axis of the fissioning nuclei and one looses some details of the process. The authors used a 2μg ^{252}Cf source shaped into 15 mm long, 1 mm in diameter rod cladded with Pt-Ir. They used two neutron detectors, one made of liquid scintillator and the other one made of anthracene crystal, attached to photomultiplier tubes. In order to reject photons coming from the source, the pulse shape discrimination technique was used. The threshold on the detectors was set to 0.7 MeV which corresponds to a proton detection threshold. One detector was fixed and the other detector was moved with respect to it. The distance from the source to the two detectors was 30 cm for angles greater or equal to 40 degrees. At angles less than 40 degrees, one detector was moved back by 40-50 cm in order to insert additional shielding and prevent detector cross talk $-$ a situation when a neutron produces a signal in one detector and then scatters into the other detector causing a false coincidence. The single neutron count rates in each detector (N_1 and N_2) and the neutron count rate in coincidence mode $N_c(\theta)$ at some specific angle θ were measured. The single neutron count rates were defined as:

$$N_1 = \Omega_1 \epsilon_1 \bar{\nu} N_f / 4\pi \text{ and } N_2 = \Omega_2 \epsilon_2 \bar{\nu} N_f / 4\pi, \tag{2.1}$$

where $\Omega_{1,2}$ are the solid angles subtended by the neutron detectors, $\epsilon_{1,2}$ are average efficiencies of the neutron detectors, and $\bar{\nu}$ is the average neutron yield per fission event and N_f is the fission rate. The coincidence rate was defined as:

$$N_c(\theta) = \Omega_1 \Omega_2 \epsilon_1 \epsilon_2 \bar{\nu} N_f P(\theta)/4\pi, \tag{2.2}$$

where $P(\theta)$ evaluates the number of neutrons emitted during the fission process in a unit solid angle at the angle θ in coincidence with the ν_{th} neutron. The ratio of the coincidence rate to the product of single neutron count rates was found:

$$R(\theta) = N_c(\theta)/N_1 N_2 = 4\pi P(\theta)/\bar{\nu} N_f \tag{2.3}$$

and plotted (see Fig. 2.2).

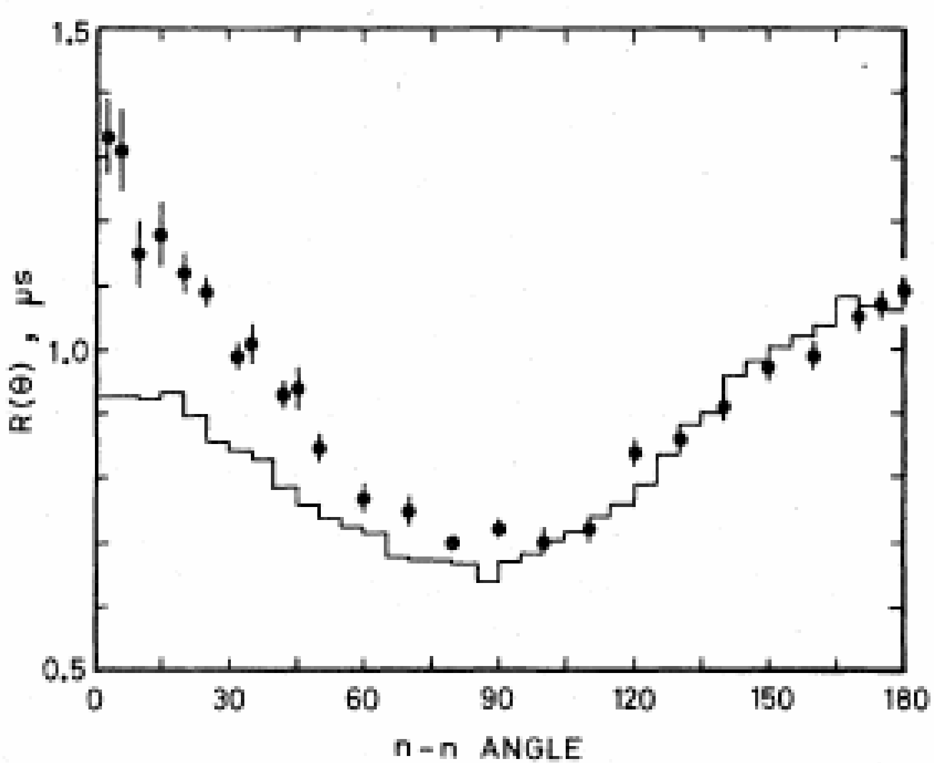

Fig. 2.2. The two neutron opening angle distribution for spontaneous fission of ^{252}Cf (dots) and a Monte-Carlo simulation of the two neutron opening angle (histogram). Picture was taken from [27].

The dots in Fig. 2.2 represent the result of the experiment, while the histogram is the result of a Monte-Carlo simulation based on the evaporation model where 10% of the neutrons came from the moment of scission and the rest of the neutrons originated by the evaporation from fully accelerated fission fragments. The discrepancy between the Monte-Carlo simulation results and the experimental data was attributed to the model used to describe the neutron evaporation process which needed to take into account the additional mechanism boosting neutrons in the direction of the fission axis.

Similar experiments were done by [28]. The authors looked for the sign of the scission neutrons investigating n-n angular correlations ^{252}Cf spontaneous fission and in the thermal neutron induced fission of ^{235,233}U and ^{239}Pu. The PNPI WWR-M Reactor was used as a source of the thermal neutrons [29]. Also, the angular correlations of n-γ and γ-γ were observed. In the experiment, two identical detectors based on stilbene crystals attached to photo multiplier tubes were used. The coincidence rates of n-n, n-γ and γ-γ pairs emitted at some specific opening angles were measured. The relative angle of observation varied from 12.5 degrees to 180 degrees with 2.5 degree increments. The time-of-flight (TOF) technique was used together with the pulse-shape discrimination technique to separate prompt fission neutrons from gammas. As an example of the experimental data obtained in [28], a plot of the angular correlation of n-n, n-γ, and γ-γ pairs in the case of thermal neutron fission of ^{235}U when the detection threshold on the prompt neutrons was set to 425 keV is presented in Fig. 2.3. No angular dependence is observed for the n-γ and γ-γ coincidence pairs.

Monte-Carlo simulations for this experiment were based on the evaporation model with an added mechanism of possible neutron emission during the fission

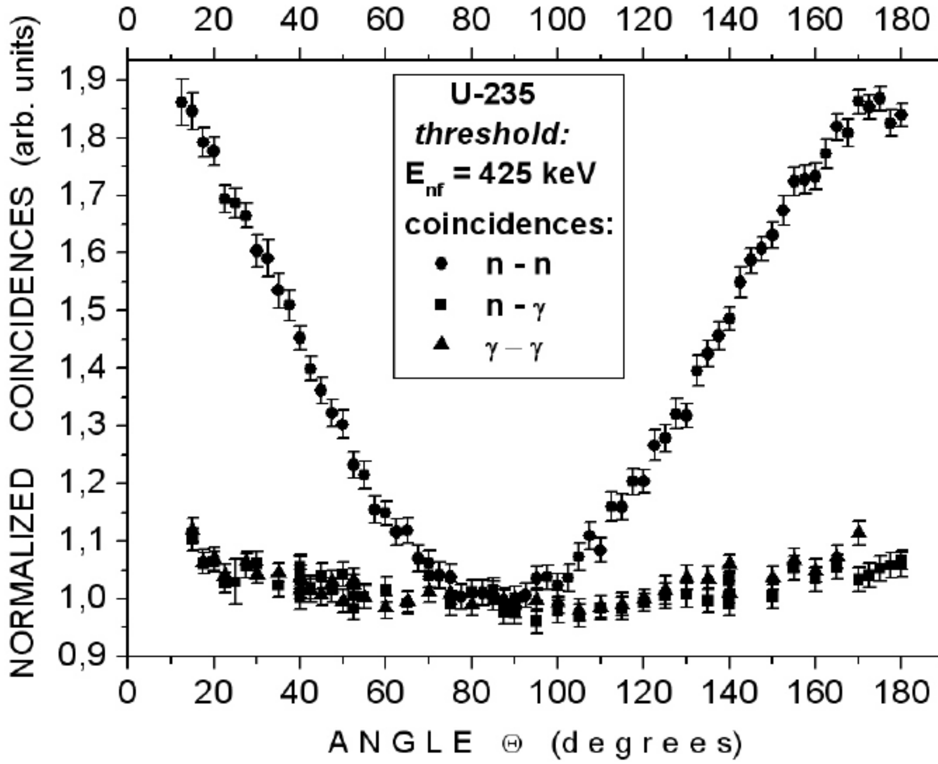

Fig. 2.3. The two neutron opening angle for thermal neutron fission of ^{235}U. Picture was taken from [28].

process. The neutrons were emitted by fully accelerated fission fragments and had a Maxwellian spectrum while the neutrons coming from the scission point had a Weisskopf distribution. There were two free parameters to be adjusted - the fraction of scission neutrons and the temperature. The comparison of the experimental data and a fit to the experimental data is presented in Fig. 2.4. The authors of [28] claimed that according to the comparison of the experimental data and Monte-Carlo simulations, around 5-15% of all neutrons were emitted isotropically in the laboratory reference frame at the moment of scission.

Additional information on the two neutron correlations in spontaneous fission of ^{252}Cf is provided in [30]. The authors measured the opening angle distribu-

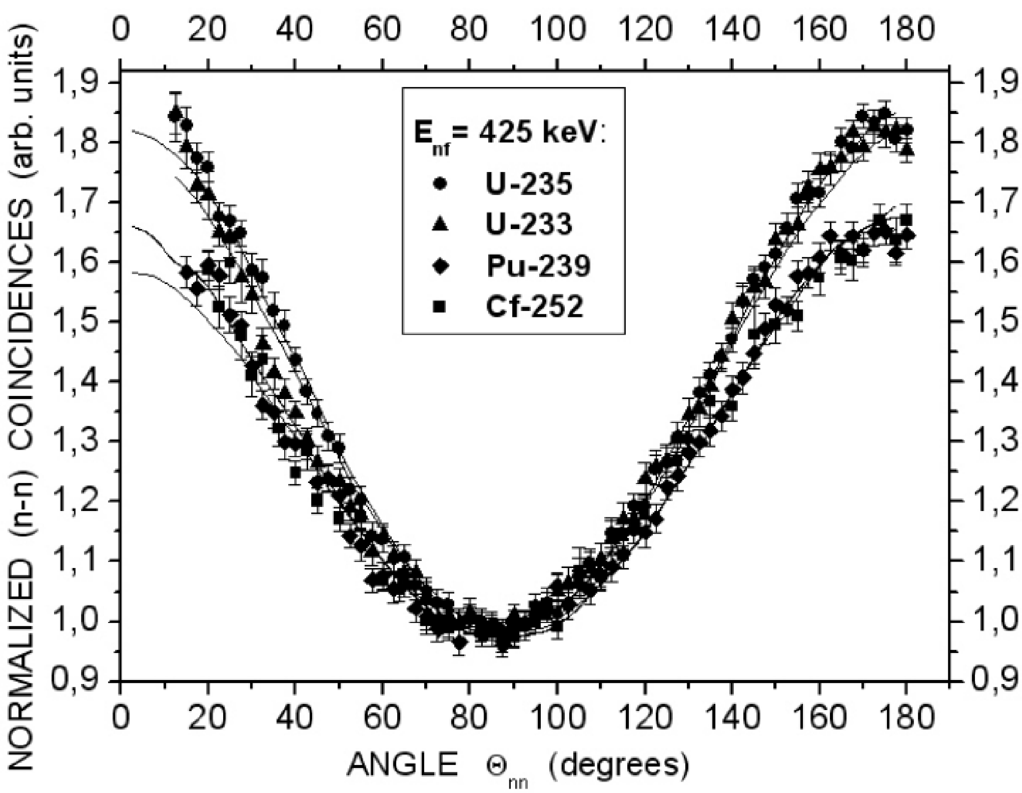

Fig. 2.4. The two neutron opening angle defined in the process of thermal neutron fission of ^{235}U. Picture was taken from [28].

tion of prompt neutrons created in the spontaneous fission of ^{252}Cf and compared the experimental data to the results of Monte-Carlo modelling (MCNPX, MCNPX-PoliMi [31]) of the process of prompt neutron emission where the neutron multiplicity, neutron energy, and neutron angular distributions were taken into account. The experimental setup consisted of 14 liquid organic scintillators attached to photomultiplier tubes and placed in a ring shape around the ^{252}Cf source positioned in the center. The setup allowed the authors to measure the relative opening angle between two neutrons being equal to 26, 51, 77, 103, 128, 153, and 180 degrees with the variance of the angle correlation $\sigma^2 = 6.5^2$ due to the finite acceptance of the detectors. In order to separate photons from prompt neutrons created in the process of ^{252}Cf spontaneous fission, the pulse-shape discrimination technique and fast timing analysis were utilized. The moment of a fission event was not observed directly via the tagging technique. Rather, the time-dependent neutron-neutron cross-correlation functions were measured. These functions represented the time difference of the neutron events selected using the pulse-shape discrimination technique and fast timing analysis for a specific pair of the detectors/angles. The cross-correlation functions had the maximum number of counts per fission when the time difference between the correlated neutron signals was equal to zero. Integration of the cross-correlation functions gave the authors the distribution of correlated angles between two prompt neutrons. The experimental data obtained in [30] are shown in Fig. 2.5 (solid lines)

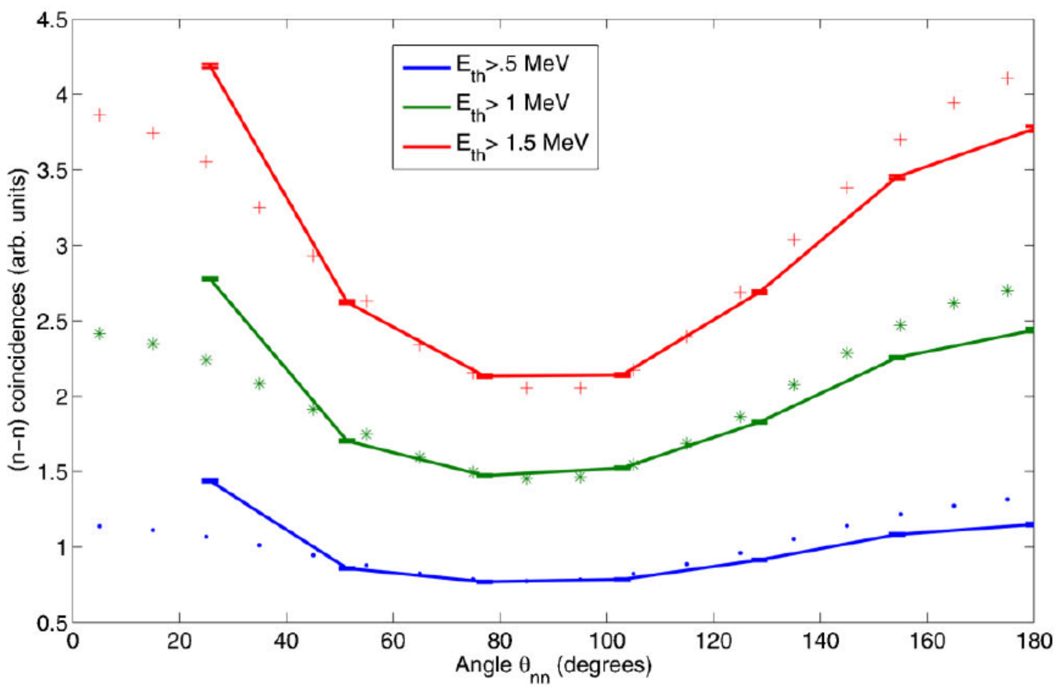

Fig. 2.5. The two neutron opening angle defined in the process of spontaneous fission of ^{252}Cf. Picture was taken from [30].

together with the data obtained using theoretical results of [32] (symbols) for different neutron energy thresholds. The discrepancy of the experimental data and the modeling at small angles was attributed to the cross talk between weakly shielded detectors when a single neutron may be scattered producing a detectable signal in the active volume of a detector and then being scattered in the active volume of the neighbouring detector producing false correlation events in the data stream for [30].

The first step in the investigation of the prompt neutron angular correlation is to know the dependence of the fission fragment masses and fission fragment kinetic energy as a function of the incident photon energy. In Ref. [23], the authors made an experimental investigation of the fission fragment yield as a function of their mass and as a function of the bremsstrahlung end point energy in ^{238}U photofission. They also measured the average total fragment kinetic energy and corresponding dispersion as a function of the fission fragments' mass and the bremsstrahlung end point energy. The dispersion of the average total fragment kinetic energy was equal for heavy and light fission fragments as a result of the symmetrization around mass $A/2$.

The average energy of the ^{238}U compound nucleus excitation was calculated for different bremsstrahlung end point energies:

$$< E_{exc}(E_e) >= \frac{\int_0^{E_e} k\sigma_{\gamma,f}(k)\phi(E_e,k)\,dk}{\int_0^{E_e} \sigma_{\gamma,f}(k)\phi(E_e,k)\,dk}, \tag{2.4}$$

where k and E_e are the photon and electron energies, $\phi(E_e,k)$ is the bremsstrahlung spectrum (Schiff form used), and $\sigma_{\gamma,f}(k)$ is the photofission cross section for ^{238}U.

The authors of [23] noticed that (a) the peak-to-valley ratio in the dependence of the fission fragment yield as a function of mass A decreases with the increase of

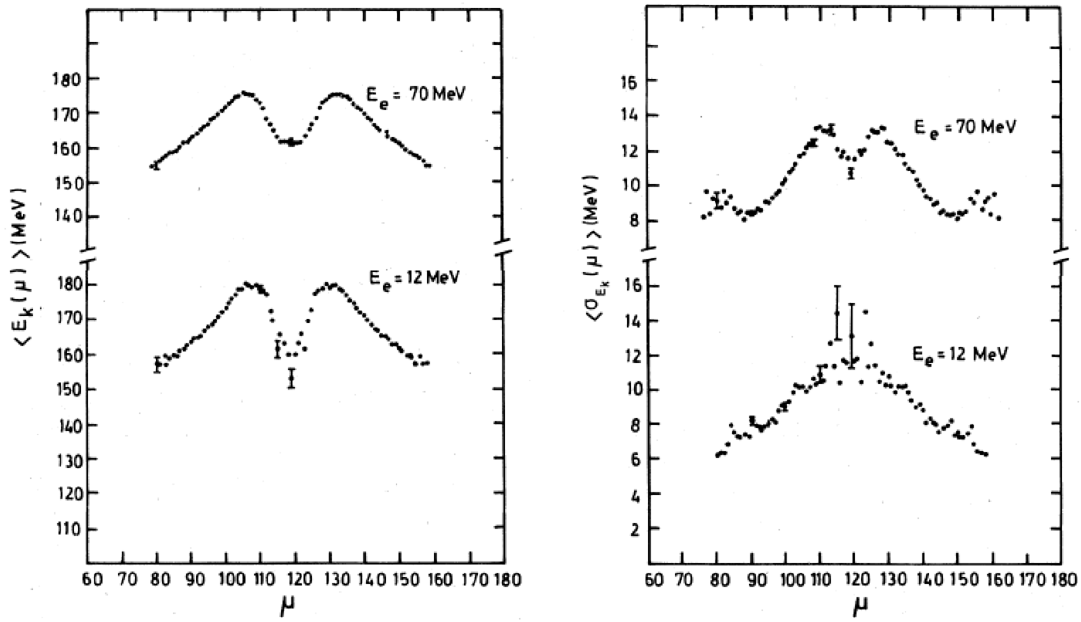

(A) **(B)**

Fig. 2.6. Average total kinetic energy of a fragment (A) and its dispersion (B) for bremsstrahlung end point energies of 70 MeV (top) and 12 MeV (bottom) in the case of ^{238}U photofission. Picture was taken from [23].

the excitation energy of the compound nucleus (see Fig. 2.7), (b) with the increase in the excitation energy of the compound nucleus, the average total kinetic energy of the fission fragment decreases, (c) the dispersion of the average total fragment kinetic energy and the average masses of the light and heavy fission fragments are almost constant with the increase of the compound nucleus excitation energy, (d) the dispersion of the average total fragment kinetic energy has an important dependence on the average fission fragment mass with a maximum that moves from higher to lower values with the decrease of the bremsstrahlung end point energy [Fig. 2.6(B)].

Using experimentally determined parameters of the fission process, it is possible to implement the data in the Monte-Carlo modelling procedure and predict

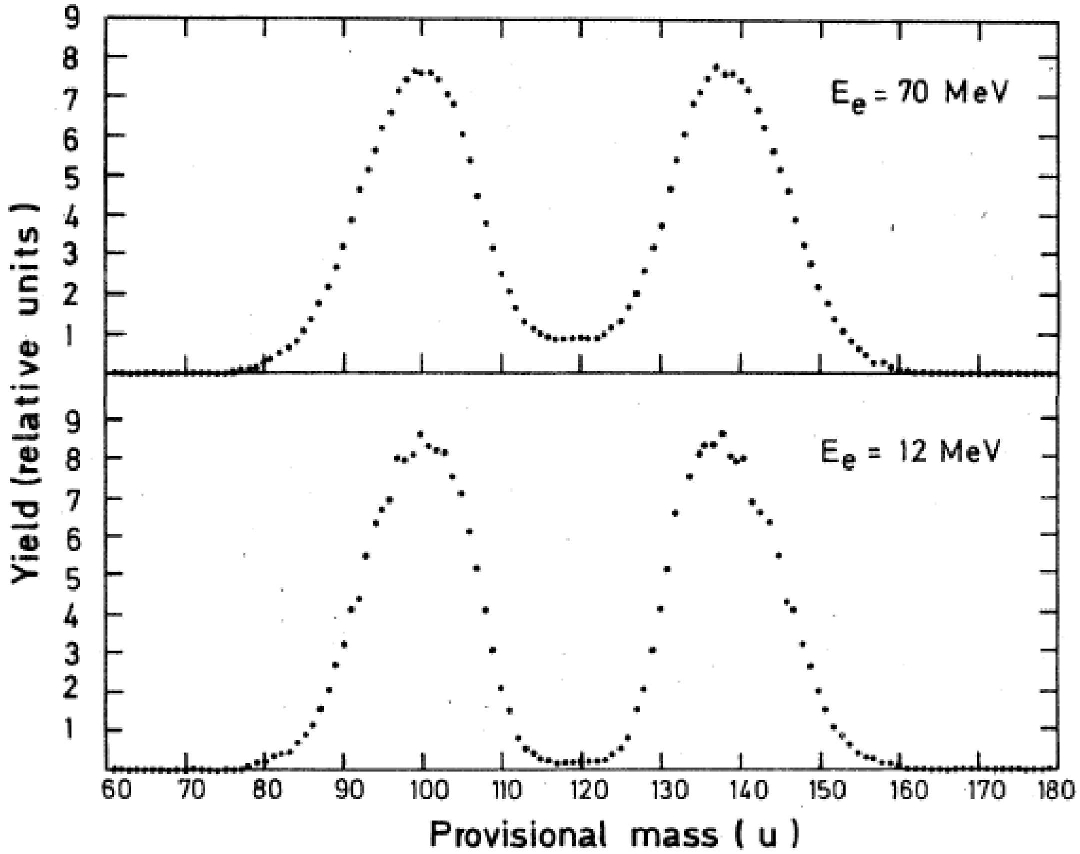

Fig. 2.7. Fission fragment mass distribution in the case of bremsstahlung end point energy of 70 MeV (top) and 12 MeV (bottom) in the case of ^{238}U photofission. Picture was taken from [23].

the dynamics of the post fission products. As mentioned above, the information obtained from the modelling can be used in many different areas such as nuclear nonproliferation applications and nuclear engineering, for instance.

The authors of [22] used the data on the fission process induced by thermal and fast neutrons to create a program based on the Monte-Carlo technique which can generate the data on the post fission products kinematics. As an input they used experimentally obtained fission fragment mass yields $Y(A)$ in neutron induced fission of ^{239}Pu, the average total kinetic energy (TKE), and the dispersion of the average total kinetic energy of the fission fragments as a function of fission fragment mass, $P(TKE|A)$. They also defined the dependence of the fission fragment mass as a function of their charge, $P(Z|A)$. The final fragment distribution was given by [22]:

$$Y(A, Z, TKE) \simeq Y(A) \times P(Z|A) \times P(TKE|A). \tag{2.5}$$

The result of the Monte-Carlo sampling for data on the thermal neutron-induced fission of ^{239}Pu is presented below (see Fig. 2.8). The average total ki-

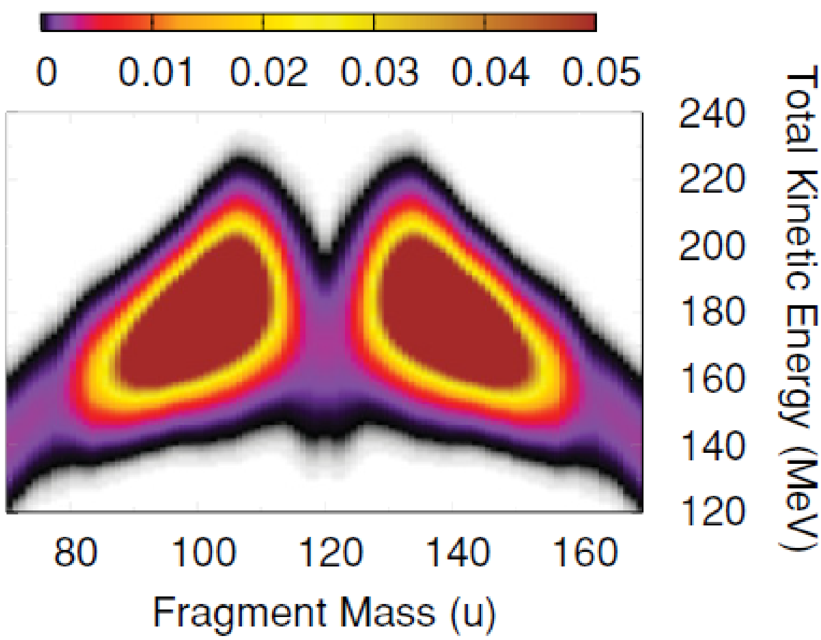

Fig. 2.8. The fission fragment yield after thermal neutron-induced fission of ^{239}Pu as a function of fission fragment mass and the total kinetic energy. Picture was taken from [22].

netic energy released in neutron-induced fission was obtained to be $< TKE >=$ 177.57 MeV. They predicted that the total kinetic energy increases as the fragment mass increases.

2.2.1 Two neutron opening angle simulation

The data from the previous section on the fission fragment mass-energy distribution generated in the process of fast neutron fission allow one to reconstruct the two neutron opening angle of prompt neutrons emitted in the fission process. The similarity of the neutron induced fission and photon (unpolarized) induced fission kinematics was suggested.

In order to obtain the neutron opening angle distribution, the prompt neutron energy distribution $N(E_n)$ was first sampled in the rest frame of the fission fragment. This spectrum is expected to follow the Maxwellian distribution [2]:

$$N(E_n) = \sqrt{E_n} \cdot e^{\frac{-E_n}{0.75}}. \tag{2.6}$$

Next, the energy and mass of heavy fission fragments (Hff) and light fission fragments (Lff) were sampled using the data plotted in Fig. 2.9. Also, the angular distributions of Hff and Lff in the lab frame were sampled with respect to the incident neutron direction assuming that only dipole fission is relevant $W(\theta) = a + b \cdot \sin^2(\theta)$. The energies of the prompt neutrons and their momenta were boosted into the laboratory frame according to the momenta and angular distribution of the fission fragments in the laboratory frame. The energy spectra of the neutrons emitted in the Lff rest frame and neutron energy boosted by the motion of the Lff is shown in Fig. 2.10.

The neutron multiplicity was set to 2 and the distribution of the emitted prompt neutrons was assumed to be the following: in 50% of the fission events each of the fragments emitted one neutron, in 30% of the events two neutrons were emitted by Lff, and in 20% of the events two neutrons were emitted by the Hff. This assumption is rather qualitative and was based on nuclear shell model

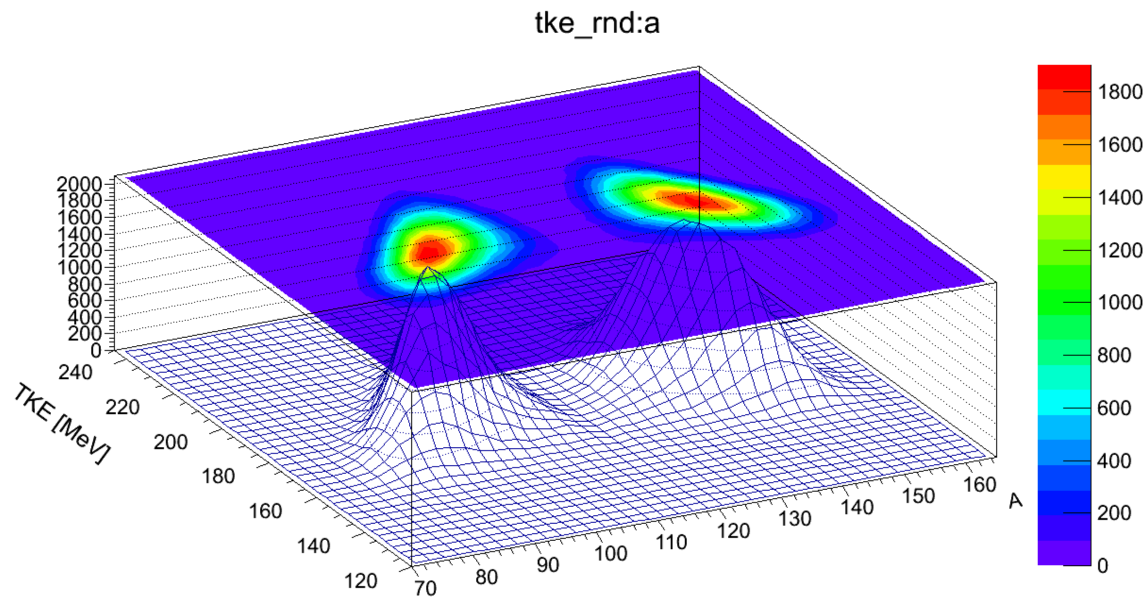

Fig. 2.9. Reproduction of the data on the fragment mass-energy distribution from [22].

considerations which predict that the light fission fragments are less bound with respect to the mass change and should emit more neutrons than the heavy fission fragments since there is not even a singly magic nucleus in the region of masses of light fission fragments. Also, it can be seen from Fig. 2.11 that the average neutron multiplicity for the heavy fission fragments is less than the one for the light fission fragments.

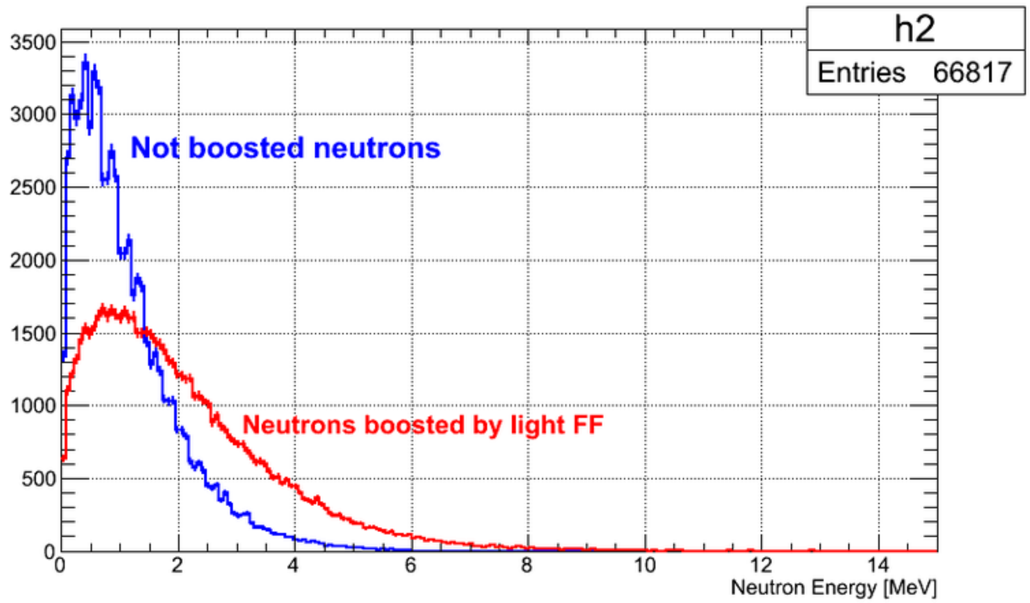

Fig. 2.10. The energy spectra of the neutrons emitted in the light fission fragment rest frame and neutron energy boosted by the motion of the light fission fragment.

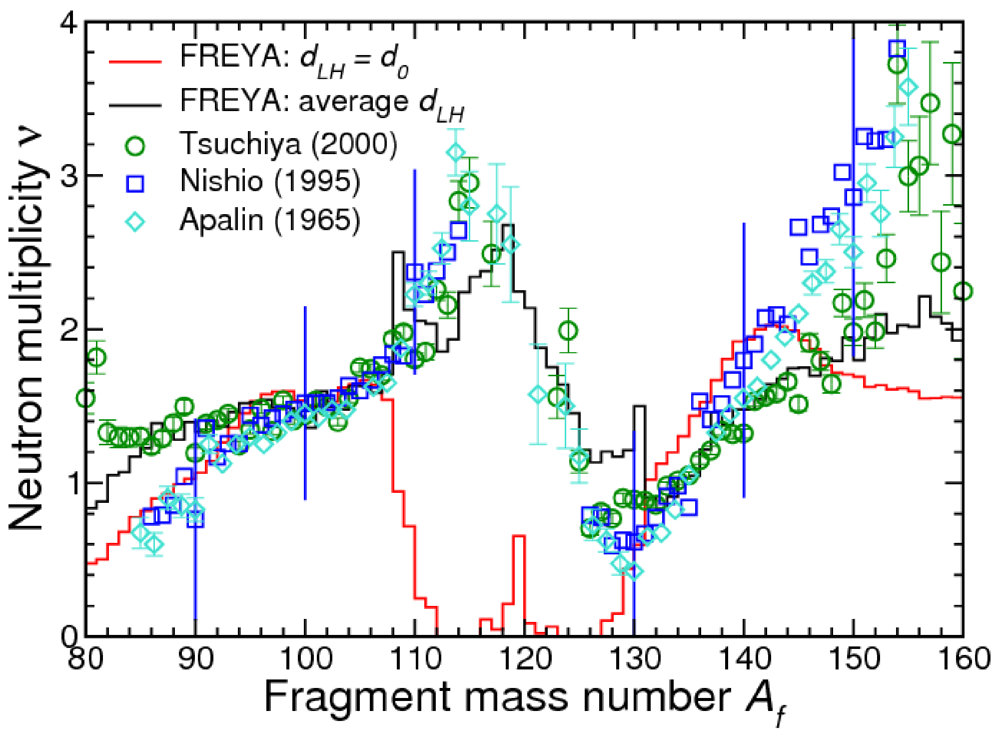

Fig. 2.11. The average neutron multiplicity as a function of the fission fragment mass for the ^{239}Pu(n, f) reaction. Picture was taken from [33].

The result of this simulation gave us the angular distribution of the opening angle between the two prompt neutrons as presented in Fig. 2.12. The qualitative expected angular distribution of the two neutron opening angles was obtained. It can be seen that the relative yield of small two neutron opening angles (~ 5 degrees) and large two neutron opening angles (~ 170 degrees) is greater than the relative yield of the opening angles with intermediate values (~ 90 degrees). This means that there is a correlation between the prompt neutron kinematics and the fission fragment kinematics: the momenta of neutrons emitted by the fission fragments are boosted in the direction of the accelerated fission fragments momenta. Increased relative yield of two neutron opening angles with small values indicates that the two neutrons were emitted by a single fission fragment and their momenta are boosted in the direction of the fission fragment momentum leading to a small opening angle. When during the fission event the fission fragments emit one neutron per fragment, then the two neutron opening angle takes greater values since the fission fragments move back-to-back along the nucleus symmetry axis and the momenta of prompt neutrons tend to be directed in opposite directions.

It should be noted that the experimental setup used to measure the two neutron opening angle distribution in this work had a finite acceptance and the opening angle distribution could not be measured beyond 90 degrees. Hence, in order to verify the prompt neutron opening angle distribution for angles greater than 90 degrees, the geometry of the setup and the number of neutron detectors need to be modified.

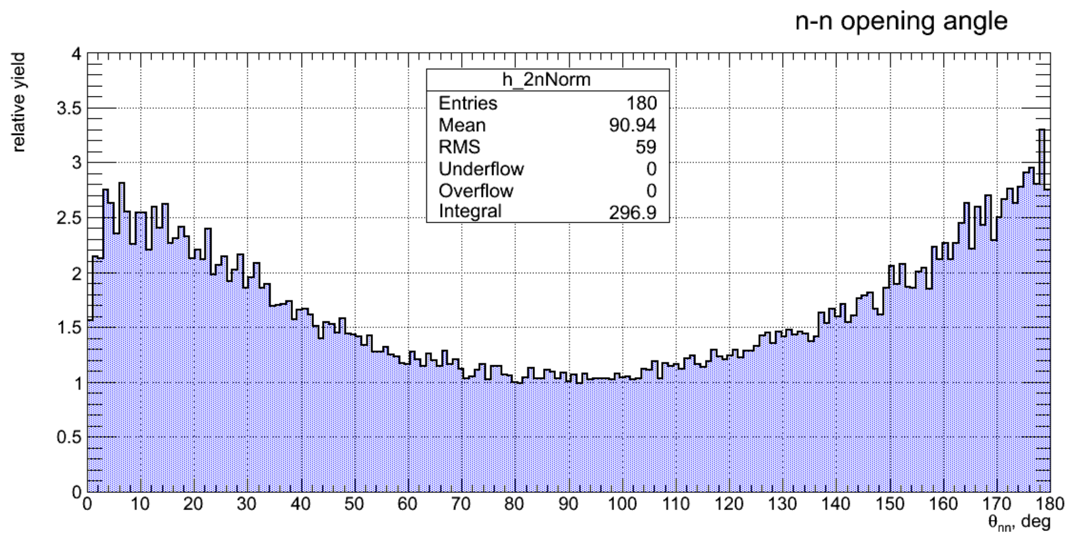

Fig. 2.12. Two neutron opening angle distribution. Picture was generated using data from [22].

2.3 Relative yield of the correlated neutrons

Here, we develop the approach of how to extract the relative yield of correlated two neutron events as a function of the neutron opening angle.

Obtaining the relative neutron yield of the correlated n-n events as a function of the opening angle θ_{op} required the analysis of two different kinds of data sets. First, we analysed "same pulse" (sp) data for the sequence of High Repetition Rate Linear accelerator (HRRL) pulses combined into runs of different duration. The same pulse data contain the following types of events:

1. correlated n-n events, both neutrons belong to the same fission event $[Y^{corr}_{nn}(\theta_{op})]$;

2. correlated γ-n events, the neutron and the photon belong to the same fission event $[Y^{corr}_{\gamma n}(\theta_{op})]$;

3. correlated γ-γ events, both photons belong to the same fission event $[Y^{corr}_{\gamma\gamma}(\theta_{op})]$;

4. accidental n-n events, both neutrons come from different fission events if there is more than one fission per pulse $[Y^{acc}_{nn}(\theta_{op})]$;

5. n-γ accidentals, which give false events in the n-n coincidence spectrum when there is imperfect γ-n separation $[Y^{acc}_{\gamma n}(\theta_{op})]$;

6. γ-γ accidentals, which give false events in the n-n coincidence spectrum, again when there is imperfect γ-n discrimination $[Y^{acc}_{\gamma\gamma}(\theta_{op})]$.

The combined neutron yield for the same pulse data set $Y^{sp}(\theta_{op})$ can be represented as a sum of the components described above [see Appendix A.1, Eq. (i)]. The correlated γ-γ and γ-n events were eliminated by setting appropriate timing cuts on the neutron time-of-flight spectra.

The experimental yield as a function of opening angle for the events attributed to the same pulse $Y^{SPD}(\theta_{op})$ [see Appendix A.1, Eq. (ii)] is shown in Fig. 2.13. There are correlated events together with uncorrelated events in the distribution. It is necessary to eliminate uncorrelated events in $Y^{SPD}(\theta_{op})$ to determine the true correlated events coming from the same fission event. The shape of this distribution is influenced by both the physics as well as the experimental acceptance of this particular detector system.

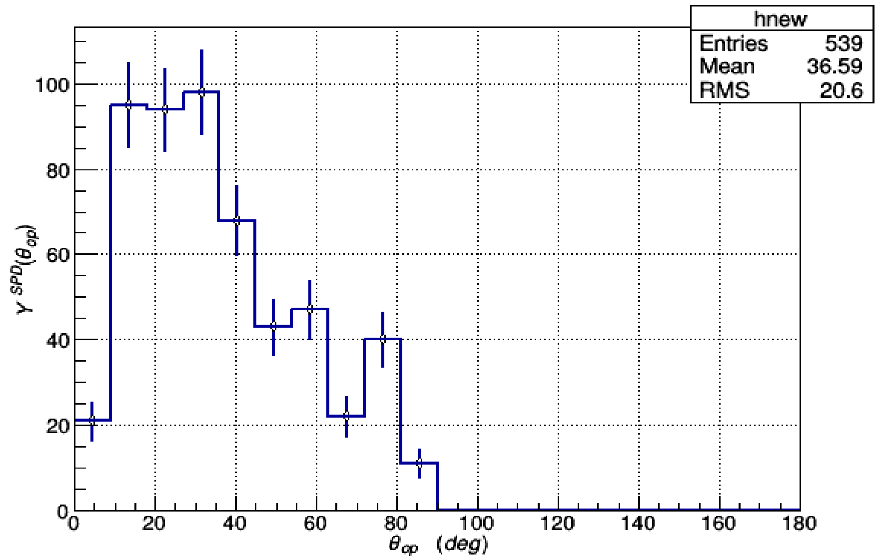

Fig. 2.13. The total yield of pairs of events originating from the same pulse as a function of the opening angle. Error bars represent statistical uncertainty.

The second kind of data was estimated using two different HRRL beam pulses (dp) that belong to the same set of data but are separated in time by 1/300 of a second. The data that can be obtained from the analysis of two different beam pulses are presented below:

1. uncorrelated n-n events, with both neutrons coming from different fission events which happened at two different moments in time [$Y_{nn}^{uncorr}(\theta_{op})$];

2. uncorrelated n-γ events, neutron and photon were produced by uncorrelated sources [$Y_{n\gamma}^{uncorr}(\theta_{op})$];

3. uncorrelated γ-γ events, both photons were produced by the sources not correlated in time [$Y_{\gamma\gamma}^{uncorr}(\theta_{op})$].

The total yield distribution of two uncorrelated events originating from two different pulses $Y^{DPD}(\theta_{op})$ can be represented as a sum of the components described above [see Appendix A.1, Eq. (iii)]. The experimental opening angle distribution for events attributed to different pulses is shown in Fig. 2.14.

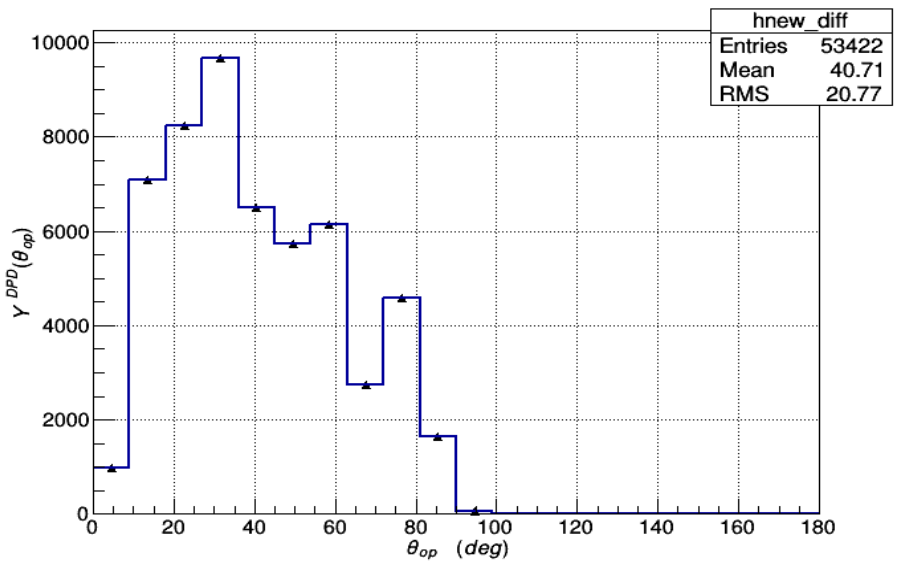

Fig. 2.14. The yield of uncorrelated pairs of events originating from two different pulses.

Since the same background effect was present in the two neutron opening angle distributions obtained in the case of the same pulse data and different pulse data, it was possible to eliminate the background using an appropriate data normalization procedure developed by [19] (see Appendix A.1) and taking the ratio which will be called the two neutron correlation function:

$$Y^{2n}_{corr}(\theta_{op}) = \frac{Y^{SPD}_{norm}(\theta_{op})}{Y^{DPD}_{norm}(\theta_{op})}, \tag{2.7}$$

where $Y^{SPD}_{norm}(\theta_{op})$ is the normalized $Y^{SPD}(\theta_{op})$ distribution and $Y^{DPD}_{norm}(\theta_{op})$ is the normalized $Y^{DPD}(\theta_{op})$ distribution. This two neutron correlation function is plotted in Fig. 2.30 and will be discussed in greater detail later in this chapter. The information obtained from two different pulses allowed us to subtract the effect of the background events contaminating the true correlated events occurring in the same fission event and observe the net effect of the correlated neutron yield:

$$Y^{2n}(\theta_{op}) = \frac{Y^{SPD}_{norm}(\theta_{op}) - Y^{DPD}_{norm}(\theta_{op})}{Y^{DPD}_{norm}(\theta_{op})} \tag{2.8}$$

which is plotted as a function of two neutron opening angle in Fig. 2.31. This procedure obviates the need for a detailed knowledge of the efficiencies and acceptances of the individual detectors, as the efficiency of the overall system detecting a given θ_{nn} bin cancels in the ratio [see Eq. (2.8)]. Since the same pulse and different pulse data were taken in an interspersed fashion, the measurement is largely insensitive to experimental drifts which occur over time scales of milliseconds or greater.

2.4 Experimental methods

2.4.1 Neutron detection principles

Generally, in order to detect a particle, it should interact with the material of the detector. One can detect the residual effects of the interaction which are ionization, nuclear reactions which produce ionization and/or light, and direct light production via excitation of the active admixture added to the bulk material of the detector. Each of the secondary effects can be observed and the signal proportional to the energy deposited by the incident particle or particle flux can be measured.

For neutron detection in the current experiment, the plastic scintillating material BC-420 was chosen. Plastic scintillator is a polymer matrix containing a substance which possesses fluorescent properties called fluor. BC-420 has excellent scintillation properties due to the presence of the fluor so that the light produced by the incident particle can be detected and the information about a particle can be obtained via supplementing devices. Neutrons do not have electric charge, and therefore cannot interact via the Coulomb field and directly produce ionization. Rather, neutrons interact with the detector material via the strong interaction. Being able to interact effectively with hydrogen nuclei, *i.e.*, protons, neutrons cause ionization via knocking out protons which interact with the active material of the detector and produce secondary ionization. In order to maximize the effect of ionization, it is desirable that the atomic weight of the detector material be close to the atomic weight of a neutron, *i.e.*, it should be light. This can be seen from the kinematics of the elastic collisions of two balls when one of the balls is at rest ($V_2 = 0$). Then the velocity of the second ball after scattering V_2^* expressed in terms of initial velocity of the first ball V_1 can be written as:

$$V_2^* = 2\frac{m_1}{m_1 + m_2}V_1. \tag{2.9}$$

Hence the second ball will get maximum speed when the masses of the two balls are equal. Therefore, the bulk material of the detector should be composed of light elements. According to the Saint-Gobain Crystals manufacturer data sheet [34], the plastic scintillator BC-420 used in the experiment has the ratio of concentrations of hydrogen atoms to the carbon atoms equal to 1.1 and its atomic weight is 1.08.

2.4.2 Light signal propagation in a scintillator material

In order to convert the time-of-flight spectra of the prompt neutrons into a one dimensional coordinate distribution, the flight time conversion factors were measured for each of the detectors. The conversion factor has dimensions of [cm$\cdot$ns^{-1}]. A 1 μCi ^{60}Co gamma ray source was used in these measurements. The source has two strong gamma emission lines at 1.173 MeV and 1.332 MeV. The photons created in the scintillator material propagate to the end of the bars and are detected by PMTs. The neutron detectors were shielded with 2$''$ of lead on the surface. A lead brick with a 0.6 cm hole was used as a collimator and was moved across the active area of the detector. The gamma source was placed over the collimator hole at different positions as indicated in Fig. 2.15.

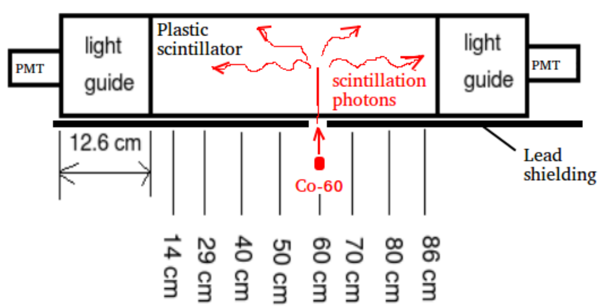

Fig. 2.15. Experimental setup for the measurement of the speed of light propagation in the scintillator material.

The time difference between the signals from two PMTs was measured. A typical time difference spectrum obtained in the experiment to determine the speed of signal propagation inside the scintillator material is shown below in Fig. 2.16.

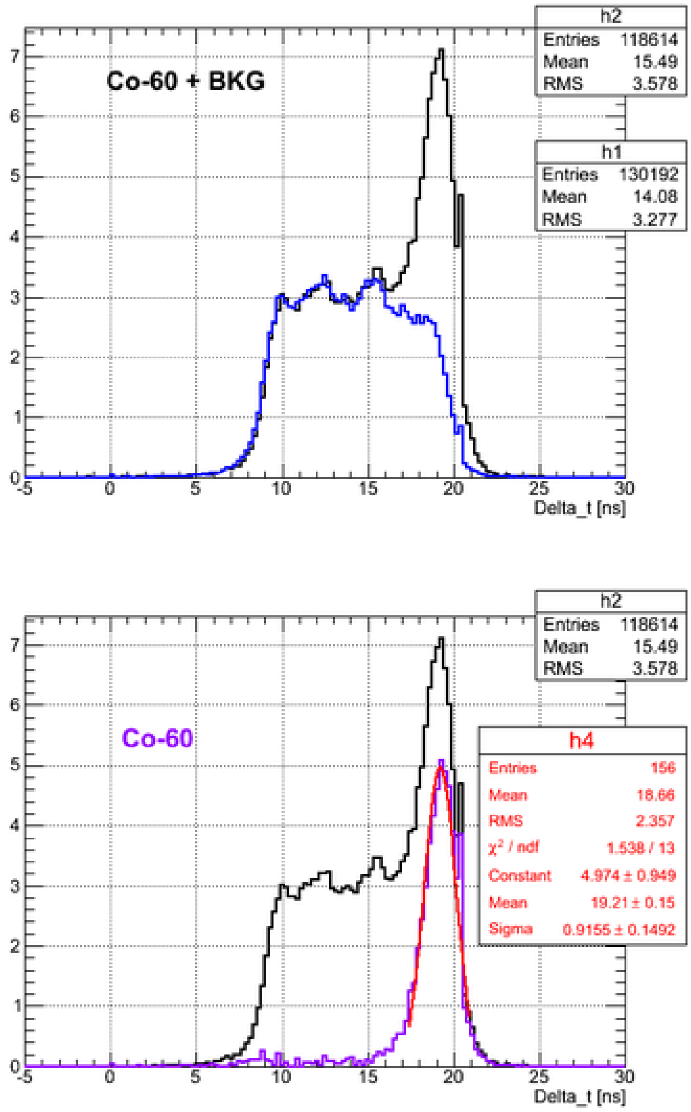

Fig. 2.16. An example of time difference spectrum. The signals are produced by a ^{60}Co source positioned over the surface of detector E. Black curve – signal combined with background, blue curve – pure background, purple curve – pure signal.

Experimental data extracted from the time difference spectra obtained with ^{60}Co source are presented in Fig. 2.17.

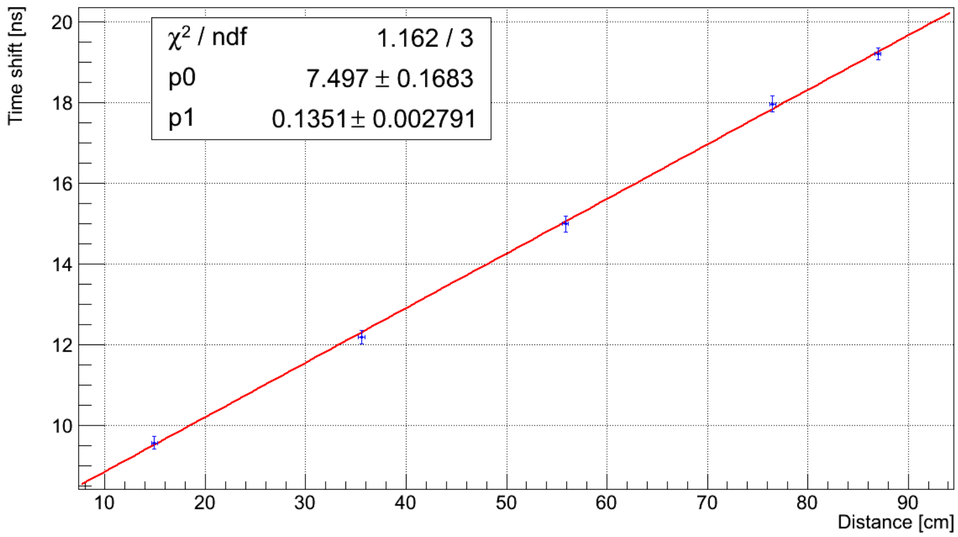

Fig. 2.17. An example of the calibration curve for the signal propagation inside the scintillator material of detector E.

The signal propagation speed in the material of the scintillator was obtained from the linear fit of the experimental data on the time difference as a function of the source position. It can be seen that in the case of detector E the effective speed of light propagating in BC-420 material is equal to 7.4 $\mathrm{cm \cdot ns^{-1}}$. More detailed information on the signal propagation speed in the material can be found in Table 2.1.

Table 2.1. Data on the effective speed of light propagating in BC-420 material.

Detector	V_{mat}, $\mathrm{cm \cdot ns^{-1}}$	δV_{mat}, $\mathrm{cm \cdot ns^{-1}}$	χ^2/ν	$\chi^2_{\alpha=0.05}/\nu$
E	7.4	0.2	0.4	2.6
M	6.8	0.3	0.01	2.6
F	7.4	0.2	0.4	2.6
G	7.2	0.2	0.1	2.6
H	7.8	0.2	0.1	2.6
K	6.7	0.2	0.2	2.1
I	5.5	0.2	1.1	2.6

The second column labelled V_{mat} represents the effective speed of light propagating in BC-420 material, the third column δV_{mat} shows the errors on the parameter V_{mat}, the fourth column shows the values of χ^2/ν statistic, where ν is the number of degrees of freedom. The fifth column shows the values of $\chi^2_{\alpha=0.05}/\nu$, where $\chi^2_{\alpha=0.05}$ is the χ^2 critical value for $\alpha = 0.05$ (95% confidence level) taken from χ^2 distribution table. The values of χ^2/ν obtained from the fit are smaller than the critical values $\chi^2_{\alpha=0.05}/\nu$ meaning that the linear fit function describes the experimental data well. The values of the effective speed of light in BC-420 material were found to be slightly different for different detectors. The light is reflected from the optical boundaries formed by the scintillator and the reflective coating (see Fig. 3.3). The difference in the quality of the optical contact of the coating and the scintillator causes the variation. Also, the experimentally determined values of the effective speed of light V_{mat} is lower than the actual speed of light in the BC-420 $V_{eff} = c/n_{BC-420} = 18.4\ \text{cm} \cdot \text{ns}^{-1}$, where n_{BC-420} is the index of refraction of BC-420 material. This could happen due to the multiple reflection of the scintillation photons from the optical boundaries of the detector which increased the time of the light collection.

2.4.3 Experimental setup for the two neutron correlation experiment

In order to measure the two neutron opening angle correlation, we induced photofission reactions on ^{238}U and observed prompt neutrons created in the reaction. The photon beam was generated using the High Repetition Rate Linear accelerator (HRRL). 10.5 MeV electrons were accelerated and impinged upon a 2.5 mm thick Al bremsstrahlung converter where they created bremsstrahlung photons (see Fig. 2.18). The repetition rate of the electron pulses was 300 Hz.

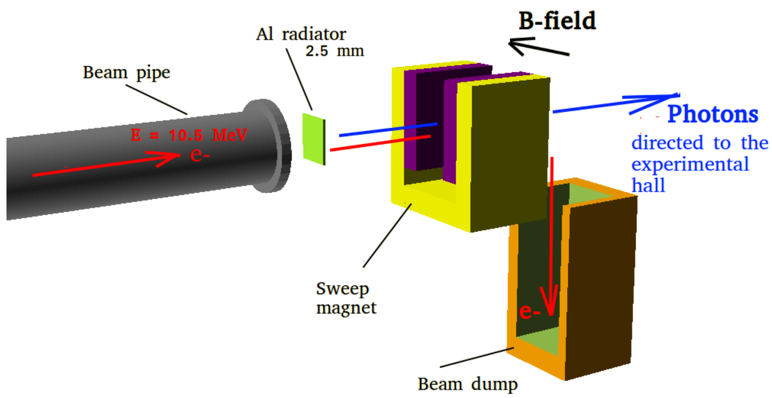

Fig. 2.18. Schematic representation of the photon beam production and charged particle separation.

To clean the electrons scattered in the bremsstrahlung converter material we used a sweep magnet. Electrons were deflected by the magnetic field of the sweep magnet towards the beam dump and photons were unaffected and transmitted further downstream.

During the experiment, two different kinds of targets were used. A deuterated water target was used to debug the experimental equipment and to obtain a neutron time-of-flight spectrum which can be described by the known kinematics of the photodisintegration of the deuteron. The main target during the actual measurement of the two neutron opening angle was a depleted ^{238}U plate with the dimensions $\sim 4'' \times 4'' \times 1/8''$. It was oriented in such way that the target material in the path of the neutrons was of the same thickness, so the neutrons travelled the same path length before they got out of the target.

To clean the photon beam from the electrons scattered inside the bremsstrahlung converter, a permanent magnet was used to bend the electrons down and send them into a beam dump consisting of Al bricks surrounded by lead and placed in the accelerator hall.

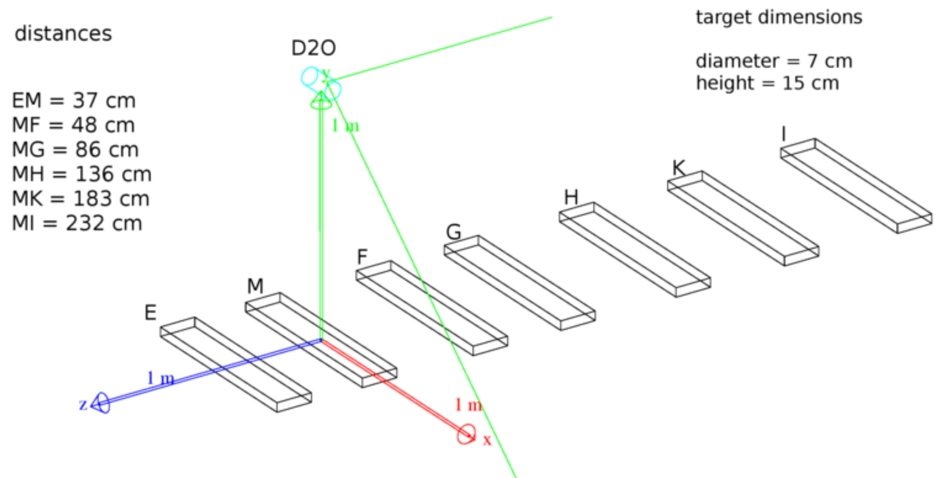

Fig. 2.19. Geometry of the experimental setup used in the two neutron correlation experiment. In the experiment the D_2O cylindrical target shown on the sketch was used for the calibration purposes and changed to a DU plate during the two neutron correlation data production runs.

After the photon beam was cleaned, it entered the experimental hall through a collimator system consisting of an upstream collimator with the hole diameter 0.25″ and a downstream collimator with the hole diameter 0.5″. The distance from the upstream collimator to the bremsstrahlung radiator was 63.7 cm. The distance from the downstream collimator to the target was 339 cm. The distance from the bremsstrahlung radiator to the target was 520 cm. The distance from the beam line to the front surface of the neutron detectors was 100.9 cm.

A positron spectrometer was used to define relative photon flux changes by measuring the rate of positrons created in air and swept by a magnetic field toward the positron detector. The operation principle of the photon flux monitor is described in Sec. 3.3.

The neutron detection was accomplished via a detector array consisting of seven plastic scintillator detectors. The neutron detector design description can be found in Sec. 3.2. After trying different configurations for the detector placement, we found the one with the lowest background contamination which is shown in Fig. 2.19.

2.4.4 Time, energy and coordinate determination of the neutron hit

The actual time of flight of the prompt neutron was calculated using the sum of times of signals coming from the two photomultipliers of a specific detector. Alternatively, it could be calculated using neutron time-of-flight spectra obtained by separate PMTs of the same detector subtracting the relative photon arrival time from the neutron arrival time observed in TDC spectrum. Additionally it would be necessary to make neutron coincidences and select the events which were observed by both PMTs. In both cases the main source of the uncertainty in the neutron time-of-flight was defined by the width of the reference photon peak. In the author's point of view, an advantage of the technique utilized is that there was no need to create an extra signal coincidence since the signals observed by both PMTs could be easily separated since their time-of-flight was larger than the time-of-flight of signals detected by a single PMT. A cumulative time-of-flight spectrum containing the information on the relative time-of-flight of photons and neutrons was calculated using the following expression:

$$TOF_n = \frac{1}{2} \cdot (TDC_1 + TDC_2 - C_t), \tag{2.10}$$

where TDC_1 and TDC_2 are the total times needed for the signal to be detected by the TDC after the trigger signal arrived to the gate of the TDC and $C_t = tof_1 + tof_2$. The terms tof_1 and tof_2 represent the times for the light to reach each photomultiplier. The value of the C_t should be constant for each detector and was defined in terms of V_{mat} (see Sec. 2.4.2) and the total length of the neutron detector. The whole detector length is known to be 101.6 cm, the inverse value of the speed of light propagation inside of detector G, for instance, is equal to 0.1387 $\text{ns} \cdot \text{cm}^{-1}$. Hence, in this case the constant $C_t = V_{mat}^{-1} \cdot 101.6$ cm = 14.1 ns. The values of C_t for different detectors used in the experiment together with the relative uncertainties are presented in Table 2.2 in the second and third columns correspondingly.

Table 2.2. Data on the C_t and its relative uncertainties.

Detector	C_t, ns	ΔC_t, %
E	13.7	0.4
M	14.9	0.3
F	13.8	0.4
G	14.1	0.4
H	13.1	0.4
K	14.8	0.3
I	18.5	0.3

To extract the actual neutron time of flight from the cumulative time-of-flight spectrum of neutrons which were detected by both PMTs, it was necessary to subtract the relative photon arrival time from the neutron arrival time observed in the cumulative TDC spectrum.

The value of the actual neutron time-of-flight can be used to determine the energy of the neutron being detected. The neutron energy can be calculated as follows:

$$E_n = \frac{m_n c^2}{2} \cdot \frac{1}{c^2} \left(\frac{l_n}{TOF_n} \right)^2, \tag{2.11}$$

where l_n is the distance from the target to the impact point on the detector, m_n is the neutron mass, TOF_n is the neutron time-of-flight, and c is the speed of light. The uncertainty of the neutron energy can be calculated using the expression:

$$\frac{\Delta E_n}{E_n} = 2 \cdot \sqrt{\frac{U^2(l_n)}{l_n^2} + \frac{U^2(TOF_n)}{TOF_n^2}}. \tag{2.12}$$

In this expression $U^2(l_n)$ is the uncertainty of the distance which neutrons pass from the target to the corresponding neutron detector. The main contribution to the $U^2(l_n)$ term comes from the finite acceptance of the neutron detectors. The term $U^2(TOF_n)$ is related to the neutron energy uncertainty. The width of the photon peak in the time-of-flight spectrum defines the main contribution to the neutron energy uncertainty term. It follows that precise measurement of the neutron energy requires small uncertainty in the definition of the distance between the target and the neutron detector and small uncertainty on the neutron time-of-flight measurement.

The uncertainty in the distance between the target and the neutron detector was simulated using the Geant4 simulation package [35]. In this simulation, neutrons were generated in the volume of the target at random positions and emitted isotropically. The target had a cylindrical shape with radius 3.5 cm and height 15 cm centered on the beam axis and placed above the center of neutron detector E at a distance 100.9 cm above its surface (see Fig. 2.19). The neutron flight path distributions were recorded. The root mean square (RMS) of the distribution was obtained for each neutron detector and the values of RMS gave us an estimate of the uncertainty in the neutron flight path for each detector. The values of RMS of the neutron flight path l^{RMS} are presented in Table 2.3.

The uncertainty of the neutron time-of-flight was obtained from the experimental data using the time-of-flight spectra. Time-of-flight spectrum clearly shows two separate peaks: one corresponding to the photon flash and another one corresponding to the arriving neutron. The neutron time-of-flight uncertainty was obtained from the Gaussian fit of gamma flash, *i.e.*, its sigma [see Fig. 2.20(B)]. More detailed information on the neutron time-of-flight uncertainty can be found in Table 2.3.

Table 2.3. Neutron time-of-flight and energy uncertainty data.

Detector	$\sigma \pm \delta\sigma$, ns	t^{RMS}, ns	l^{RMS}, cm	ΔE_9, MeV	ΔE_1, MeV
E	10.7 ± 0.7	62	2.87	4	0.2
M	7.6 ± 0.5	65	2.38	4	0.2
F	9.0 ± 0.6	66	2.67	5	0.2
G	18.9 ± 1.4	68	3.23	11	0.5
H	11.5 ± 0.8	73	3.65	7	0.3
K	11.8 ± 0.9	80	4.16	7	0.3
I	26.3 ± 4.1	69	4.32	15	0.6

The second column in the table shows the values of sigma and its uncertainty obtained from the Gaussian fit of the peak of the photon flash for each of the detectors. The value of the sigma was used as an estimate of the neutron time-of-flight uncertainty in Eq. (2.12). The third column t^{RMS} gives the values of RMS of the whole photon region in the time-of-flight spectrum. The neutron time-of-flight uncertainty achieved running the experiment at HRRL with the suggested electron pulse width ~ 20 ns introduced a high uncertainty in the neutron energy which is reported in the last two columns of the table. The column ΔE_9 gives the energy uncertainty for 9 MeV neutrons. The column ΔE_1 gives the energy uncertainty for 1 MeV neutrons. An example of the neutron energy uncertainty change as a function of the neutron energy is presented in Fig. 2.20(D). In order to decrease the time-of-flight uncertainty the electron pulse should be well-shaped with the width as narrow as possible.

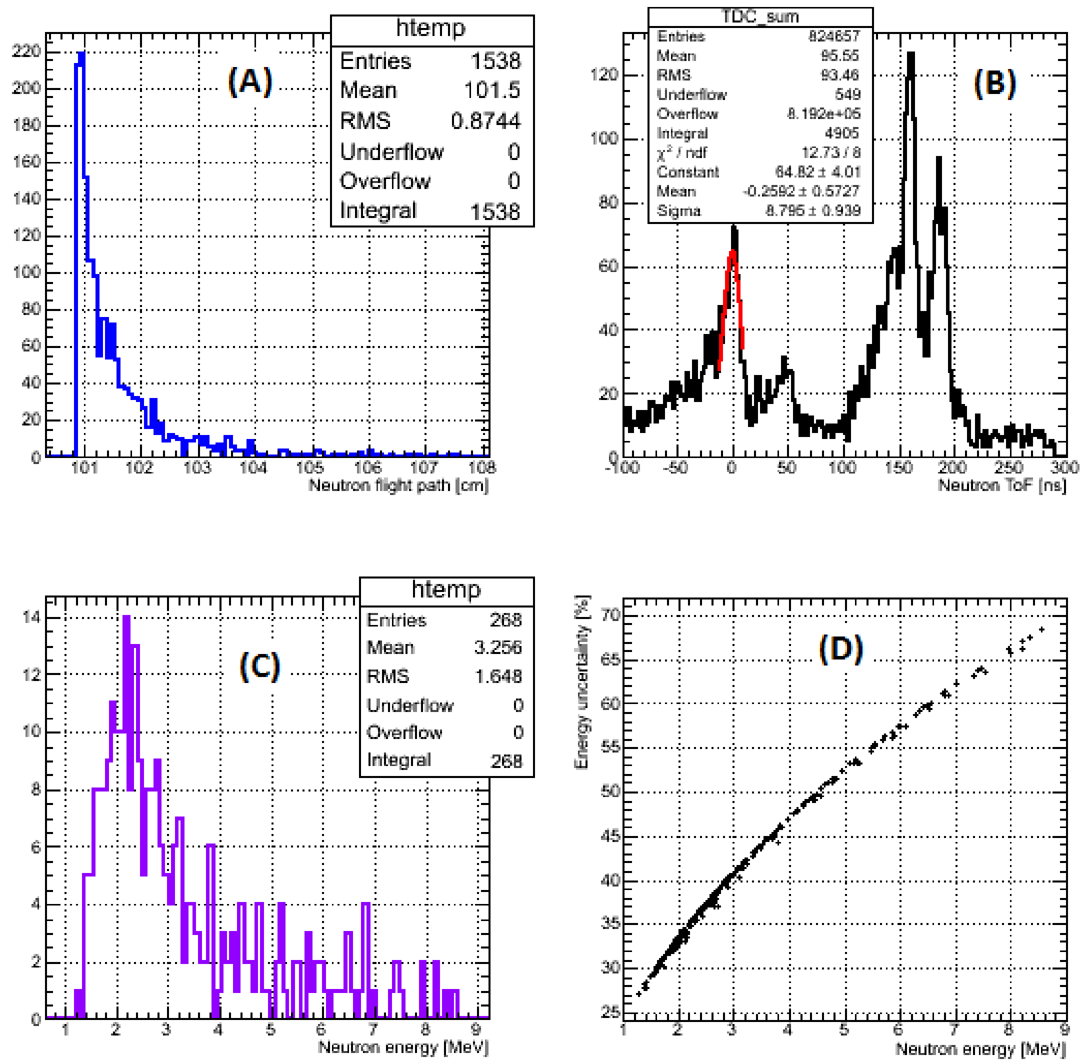

Fig. 2.20. An example of the neutron energy uncertainty distribution. (A)-distribution of the distances from the target to the detector surface (neutrons+photons), (B)-inverted time-of-flight spectrum, (C)-neutron energy spectrum, (D)-neutron energy uncertainty as a function of the neutron energy.

The neutron detector design allowed a determination of the coordinate of the neutron hit in one-dimension along the long side of the scintillator bar. The coordinate of the hit could be found in different ways. To determine the coordinate, one uses the charge signals E_1 and E_2 from both ends of the scintillator bar [36]. The coordinate can be expressed as:

$$x = \frac{1}{2\alpha} ln \frac{E_2}{E_1}, \tag{2.13}$$

where α is light attenuation coefficient for the scintillator material. Hence, if one knows the amplitudes of two signals collected at different sides of the neutron detector and the light attenuation coefficient, it is possible to calculate the coordinate of the neutron hit.

The method of coordinate measurement used in the current experiment was based on the calculation of the time difference between the signals arriving from the two PMTs. Ideally, the time difference should be zero when neutrons hit exactly in the middle of the scintillator bar, and increase as the location of the hit moves towards the ends of the scintillator. The real distribution of the time differences will be shifted one way or another depending on the delay introduced by the signal cables, PMT transit times, and PMT voltage dividers circuits. The coordinate of the neutron impact on the detector surface was calculated as:

$$X_n = (TOF_1 - TOF_2) \cdot V_{mat}, \tag{2.14}$$

where V_{mat} is the propagation speed of light inside the detector material discussed before. A typical spectrum of the neutron and gamma time-of-flight difference distribution obtained for the two photomultipliers attached to the ends of the same detector is shown below in Fig. 2.21.

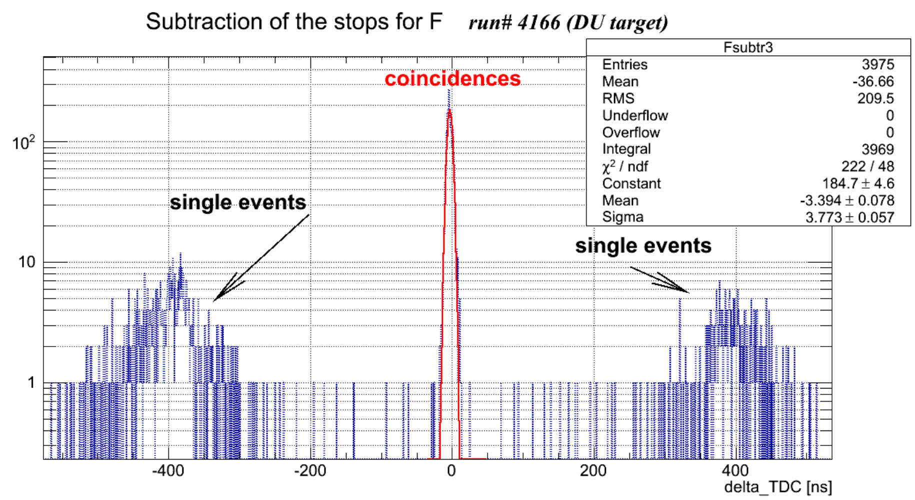

Fig. 2.21. An example of the spectrum of the difference of neutron and gamma TOF spectra obtained via detector F with the DU target.

It can be seen that a certain number of produced scintillations were detected with either only the left or the right phototube of the neutron detector. We were interested in the events which were detected simultaneously by the two PMTs. The time difference between two signals is small and, hence, all the events obtained by two PMTs at the same time will be concentrated around zero time difference (see the peak in the center of Fig. 2.21).

2.4.5 Neutron detector efficiency measurement technique

In this section, the technique for the efficiency measurement of the large plastic neutron detector will be described. Knowledge of the absolute efficiency of the neutron detector was not necessary for the technique used in the two neutron correlation experiment since it cancels in the ratio of correlated events and uncorrelated events. However, we needed to achieve the conditions when approximately one fission per accelerator pulse was generated in the target. If the prompt neutron multiplicity ν, the neutron detector geometrical efficiency ϵ_{geom}, and the neutron detection efficiency ϵ_{det} are known, it is possible to determine the conditions for one fission per pulse by calculating the single neutron counting rate:

$$R \sim \nu \epsilon_{geom} \epsilon_{det}. \tag{2.15}$$

For the efficiency measurement, a ^{252}Cf neutron source was used. In order to be able to detect fission neutrons, a fission trigger was created consisting of the ^{252}Cf source and a NaI(Tl) detector. The main idea of the trigger is to detect prompt gammas originating from ^{252}Cf spontaneous fission via the NaI(Tl) scintillator, and trigger the data acquisition system (DAQ) on the photon signal. A detailed description of the DAQ can be found in Sec. 3.1. To eliminate signals produced by neutrons, the NaI(Tl) detector was covered with two inches of borated polyethylene. The voltage divider of the NaI(Tl) detector had two outputs: (1) a timing output and (2) the usual analogue output. The timing output was shaped and discriminated, and then split into two NIM signals. One delayed NIM signal was used as the data acquisition system trigger and the un-delayed NIM signal served as a fake stop signal to monitor the DAQ system functionality. The neutron detector produced signals when neutrons hit its active area. In order to prevent photons from producing a signal in the neutron detector, it was covered with two inches of lead.

Since the neutron detector was shielded with lead, the photon flux from the ^{252}Cf was suppressed during the actual efficiency measurements. In order to reliably define the reference time in the time-of-flight spectrum corresponding to the prompt photons originating from the spontaneous fission of ^{252}Cf, a ^{22}Na photon source which emits two annihilation back-to-back photons with energies 0.511 MeV was used. A lead brick with a hole of diameter of 1.5 cm was placed around the center of the active area of the neutron detector. This allowed one of the annihilation photons to get through the lead shielding and produce a signal in the neutron detector. The other annihilation photon hit the NaI(Tl) detector and produced the DAQ trigger signal (see Fig. 2.22). The distance between the NaI(Tl) and plastic scintillator detector was 20 cm and the ^{22}Na source was placed between the two detectors.

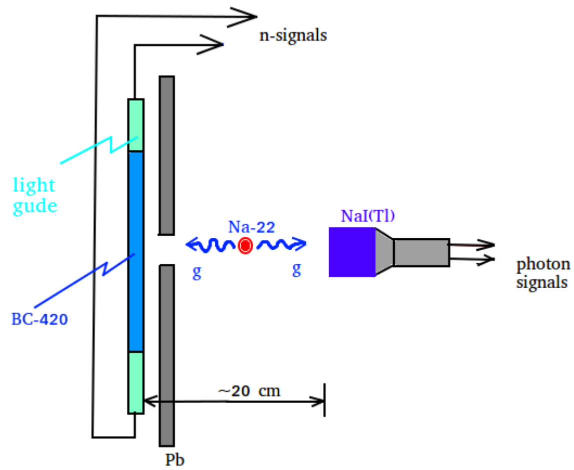

Fig. 2.22. Schematic representation of the setup used to measure the neutron detector efficiency. Timing calibration stage.

There was no additional shielding around the NaI(Tl) detector because the ^{22}Na activity was substantially higher than the intensity of background radiation.

After the reference time was established, the NaI(Tl) detector was moved inside an additional lead shielding at a distance ∼65 cm away from the neutron detector and the front part of NaI(Tl) was covered with 2″ of borated polyethylene.

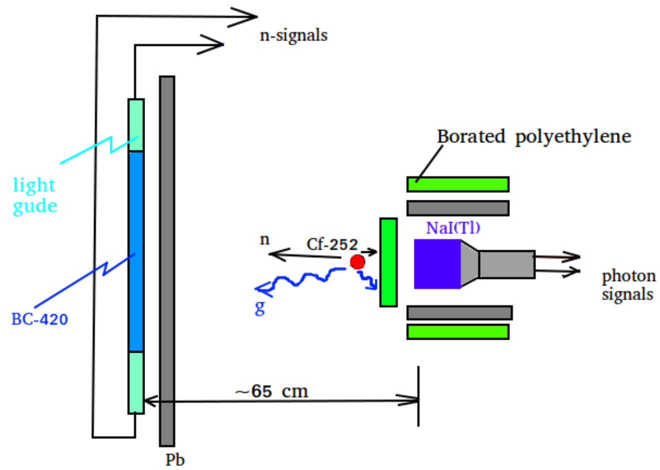

Fig. 2.23. Schematic representation of the setup used to measure the neutron detector efficiency. NaI(Tl) detector in this configuration served as a fission trigger. The timing output of this detector was used to trigger DAQ.

The lead collimator in the neutron detector shielding was replaced with a solid lead brick. The ^{252}Cf source was positioned right in front of the shielding of the NaI(Tl) detector (see Fig. 2.23) and time-of-flight spectra were taken with the photon signal being used as a DAQ trigger.

Background measurement was made without the ^{252}Cf source to understand the impact of cosmic radiation and radiation from surrounding materials on the experimental data.

The efficiency of the neutron detector ϵ_{det} was calculated using Eq. (2.16):

$$\epsilon_{det} = \frac{N_n}{N_{trig}\frac{1}{\nu}\frac{4\pi}{\delta\Omega}}, \tag{2.16}$$

where $\nu = 3.77$ is the prompt neutron multiplicity per fission event of ^{252}Cf, solid angle $\delta\Omega = 0.237$ sr, N_n is the number of neutrons detected by the neutron detector during the time Δt, and N_{trig} is the number of trigger signals produced during the same time Δt by photons in the NaI(Tl) detector. The efficiency was measured for different values of the constant-fraction discriminator thresholds and found to be ∼14% at a threshold of constant fraction discriminator where the analogue neutron signals were supplied set to 1 mV.

The neutron detector efficiency measurements enabled the electron accelerator settings to be adjusted according to the requirement of less than 1 fission per pulse, which was verified during the actual experiment. The average number of prompt neutrons per fission event is subject to Poisson statistics. The Poisson distribution can be presented in the form:

$$P(n) = \frac{\bar{n}^n e^{-\bar{n}}}{n!}. \tag{2.17}$$

The Poisson probability distribution for observing one prompt neutron per pulse is defined as:

$$P(1) = \frac{\bar{n}^1 e^{-\bar{n}}}{1!} \tag{2.18}$$

and the Poisson probability distribution for observing two prompt neutrons per pulse is given by:

$$P(2) = \frac{\bar{n}^2 e^{-\bar{n}}}{2!}. \tag{2.19}$$

The ratio of the two distributions is:

$$\frac{P(1)}{P(2)} = \frac{\bar{n}^1 e^{-\bar{n}}}{\bar{n}^2 e^{-\bar{n}}} \cdot 2 = \frac{2}{\bar{n}}. \tag{2.20}$$

Experimentally it was found that the ratio of the neutron yields of correlated neutrons over uncorrelated neutrons is equal to 2.4. The ratio of the two Poisson distributions was set to be equal to $P(1)/P(2) = 2.4$ and, hence, it was determined that the average number of fissions per pulse is $\bar{n} = 2/2.4 = 0.83$.

2.5 Results and discussion

2.5.1 Coordinate resolution of the neutron detectors

In order to calculate the precision of the neutron time of flight and neutron energy it is necessary to know the position resolution of the neutron detectors.

If we have a physical process described in the time domain by a function $h(t)$ then the Fourier transform of $h(t)$ into the frequency domain $H(f)$ is given by the following equation in the case of continuous transformation:

$$H(f) = \int_{-\infty}^{\infty} h(t) e^{-2\pi i f t} \, \mathrm{d}t, \tag{2.21}$$

and in the case of discrete transformation:

$$H_n \equiv \sum_{k=0}^{N-1} h_k e^{-2\pi i k n/N}. \tag{2.22}$$

If there are two functions h(t) and g(t), and their Fourier transforms are $H(f)$ and $G(f)$, one can define the convolution of these two functions:

$$g * h = \int_{-\infty}^{\infty} g(\tau) h(t-\tau) \, \mathrm{d}\tau. \tag{2.23}$$

In this case the convolution theorem states that [37]:

$$g * h \Longleftrightarrow G(f)H(f), \tag{2.24}$$

i.e., the Fourier transform of the convolution of two functions is the product of individual Fourier transforms.

For the purpose of the determination of the position resolution, the discrete Fast Fourier Transform (FFT) algorithm [37] was used. FFT is an algorithm that allows one to calculate the Discrete Fourier Transform (DFT) and its inverse.

We suggest that the experimental coordinate distribution obtained with the neutron detector can be represented as the convolution of the ideal response function of the detector and a Gaussian which represents the effect of finite coordinate resolution (see Fig. 2.24).

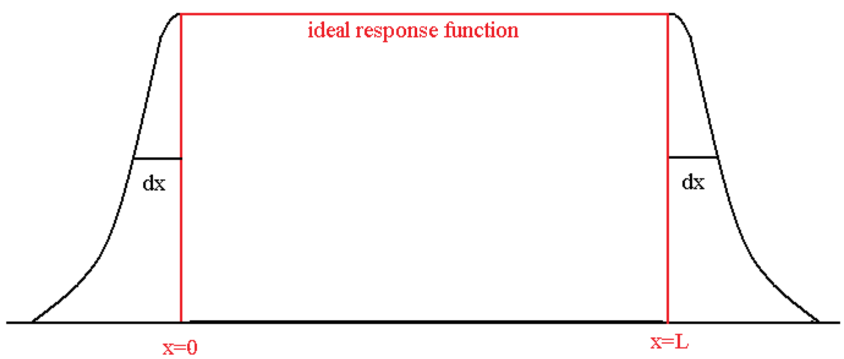

Fig. 2.24. Schematic representation of the ideal detector one-dimensional coordinate response function (red) together with the effect of finite coordinate resolution dx. The length x of the neutron detector active area is L.

Full width at half maximum of the Gaussian distribution was used as a parameter to describe the uncertainty in the position of the neutron hits. In this experiment, only one coordinate was defined along the long side of the neutron detector. In order to get the value of the width parameter of the Gaussian distribution, the experimental data were fit with a curve that was parametrized in the process of the convolution and the width was one of the parameters adjusted during the experimental neutron coordinate distribution fitting procedure. The results of the fitting of the coordinate distribution of neutron hits over the detector surface are presented in Figs. 2.25 and 2.26, and in Table 2.4.

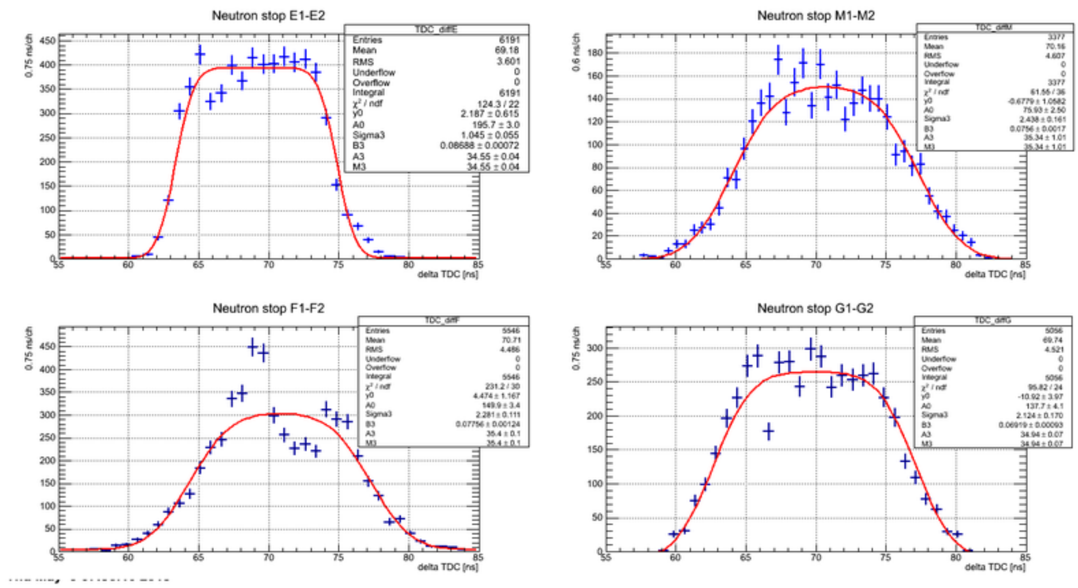

Fig. 2.25. The result of the fit of the neutron coordinate distribution with the parametrized fit function for the first four neutron detectors E, M, F, and G.

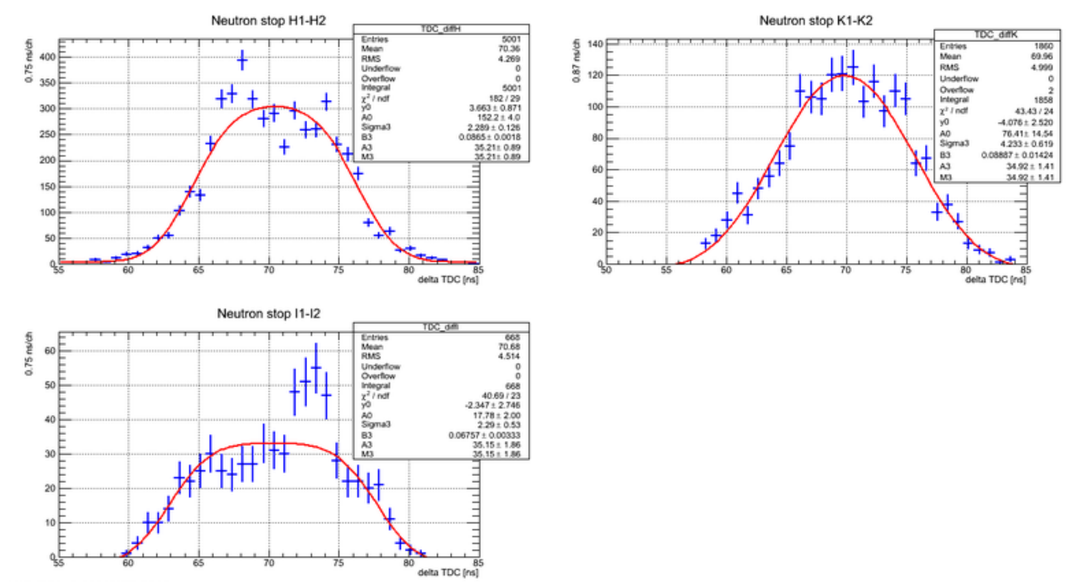

Fig. 2.26. The result of the fit of the neutron coordinate distribution with the parametrized fit function for the last three neutron detectors H, K, and I.

Table 2.4. Detector position resolution data.

Detector	R, cm	δR, cm	χ^2/ν	$\chi^2_{\alpha=0.05}/\nu$
E	7.7	0.4	5.6	1.5
M	16.6	1.1	1.8	1.4
F	16.8	0.8	7.7	1.5
G	15.4	1.2	4.0	1.5
H	17.8	1.0	6.3	1.5
K	28.4	4.2	1.8	1.5
I	16.2	2.9	1.8	1.5

The second column labelled R represents the uncertainty of the neutron hit coordinate, the third column δR shows the errors on the parameter R, the fourth column shows the values of χ^2/ν statistic, where ν is the number of degrees of freedom. The fifth column shows the values of $\chi^2_{\alpha=0.05}/\nu$, where $\chi^2_{\alpha=0.05}$ is the χ^2 critical value for $\alpha = 0.05$ (95% confidence level) taken from χ^2 distribution table. The values of χ^2/ν obtained from the fit are higher than the critical values $\chi^2_{\alpha=0.05}/\nu$ meaning that the fit function chosen does not represent the distribution of the experimental data well. The experimental data showed some non-uniformity on the top of the coordinate hit distributions which was supposed to be flat. That could be the result of cracks between the lead bricks composing the shielding of the neutron detectors. The presence of the cracks in the shielding would increase the yield at a certain coordinate. Still the data from Table 2.4 can be used as an estimate of the uncertainty in the position of the neutron hits over the surface of the neutron detector.

2.5.2 Data from the two neutron correlation measurements

The main goal of the two neutron correlation experiment was to obtain time-of-flight spectra of prompt neutrons. In Fig. 2.27 one can see a typical time of flight spectrum of prompt neutrons emitted in deuteron photodisintegration. It should be noted that the time in the TOF spectra is inverted. The photon peak is on the right hand side of the prompt neutron area and the neutron time-of-flight should be calculated with respect to the center of the photon peak.

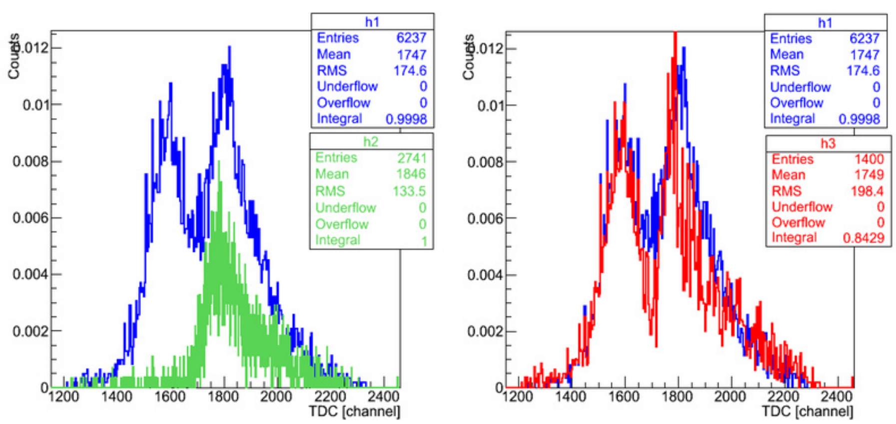

Fig. 2.27. Typical time of flight spectrum of neutrons created in the deuterium photodisintegration reaction. The blue curve on the left and right plots is the cumulative yield including signal+background. The green curve on the left plot is the background measured with no target in place. The red curve on the right plot is the target related yield of photons and neutrons with the background subtracted.

The green curve on the left side of the figure is the signal obtained with the empty target, *i.e.*, it represents a background signal. The blue curve is the data obtained with the D_2O target placed in the beam. In order to estimate the effect of the background on the signal, the background was subtracted from the signal and the result can be seen on the right side of the figure. The signal+background and pure signal have nearly the same magnitude indicating that the data obtained were beam related with low background impact.

A typical time-of-flight spectrum of prompt neutrons created in the photofission process of ^{238}U is presented in Fig. 2.28.

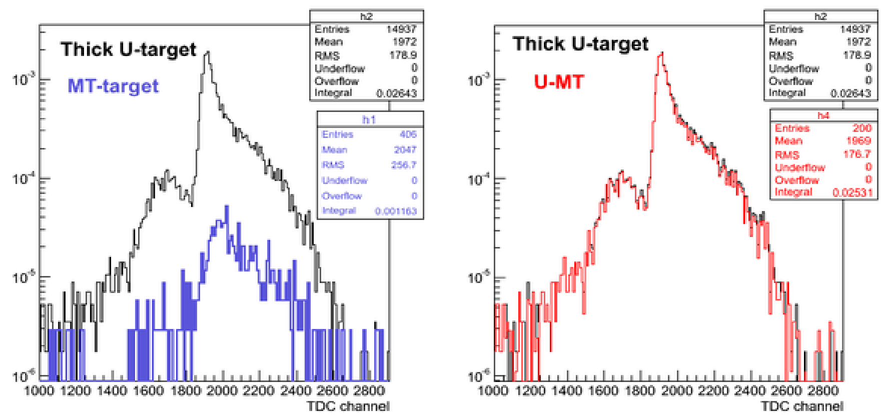

Fig. 2.28. Typical time of flight spectrum of neutrons created in the ^{238}U photofission reaction. The black curve on the left and right plots is the cumulative yield including signal+background. The blue curve on the left plot is the background measured with no target in place. The red curve on the right plot is the target related yield of photons and neutrons with the background subtracted.

The relative effect of the target and the background can be seen. The blue curve on the left side of the figure is the signal obtained with the empty target. The black curve is the data obtained with the DU target placed on the beam. As in the case with D_2O target, the signal+background and pure signal have almost the same magnitude and the shape in the neutron area.

After collecting raw data, the data analysis was performed. In order to extract the information on the two neutron opening angle between neutrons created in photofission of ^{238}U, the time-of-flight spectra of prompt neutrons were used.

A program based on C++ coding was written to allow one to make four-fold coincidences. First, the coincidences were found between two PMTs of each neutron detector. As can be seen in Fig. 2.29 the time-of-flight spectrum obtained by two PMTs of one detector can be transformed to give the information on the time-of-flight spectrum of neutrons that were detected by the two PMTs at the same time. In order to get the TOF spectrum of neutrons in coincidence mode it was necessary to add neutron TOF spectra from the two PMTs:

$$TOF_n^{two-fold} = TOF(PMT_A) + TOF(PMT_B). \tag{2.25}$$

If either time-of-flight $TOF(PMT_A)$ is equal to zero, *i.e.*, missing in the time-of-flight of the single PMT, for a given $TOF(PMT_B)$ or the other way around around it means that:

$$TOF(PMT_A) + TOF(PMT_B) = TOF(PMT_A), \tag{2.26}$$

for example. When there is a signal in both PMTs, the time-of-flight will increase and it is possible to observe the time-of-flight of neutrons in two-fold coincidence mode (see Fig. 2.29).

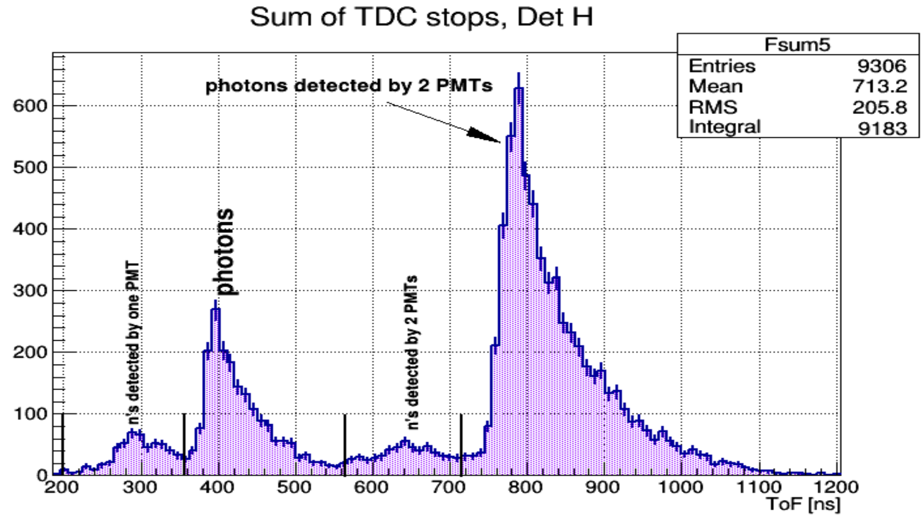

Fig. 2.29. An example of composite TOF spectrum obtained during the experiment by summing up the TOF spectra of two PMTs attached to detector H.

In the same way, by adding the TOF's obtained from two different PMTs looking at the same scintillator, the neutron signal coincidences were found for the second neutron detector. Finally, the four fold coincidences were found for two separate neutron detectors using offline data analysis.

Using the software written and the data obtained from same pulse data and different pulse data (see Sec. 2.3) it was possible to find the normalized ratio of correlated events over uncorrelated events.

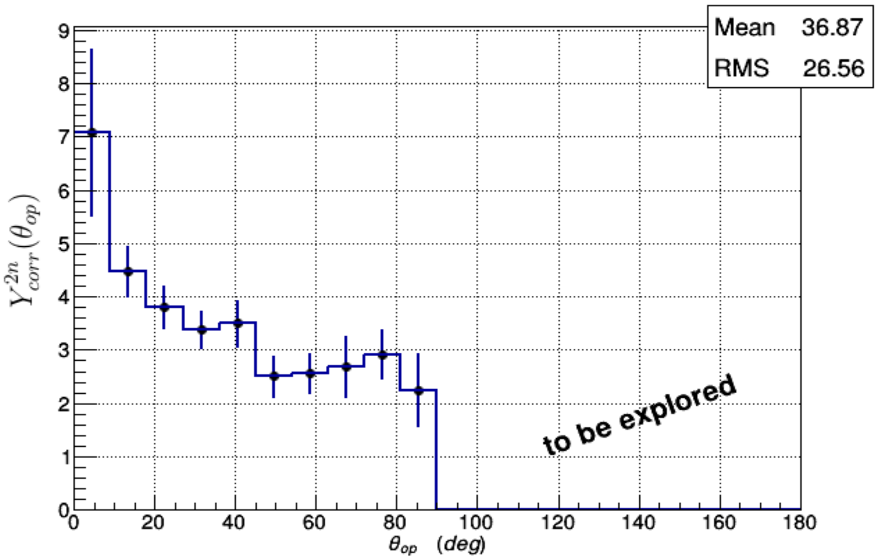

Fig. 2.30. Net yield of the correlated events as a function of the opening angle. The ratio of the two yields in the opening angle range [0,10] degrees and [80,90] degrees is $R(90/10) = 0.3 \pm 0.1$.

By subtracting the totally uncorrelated events distribution from the correlated events distribution and taking a ratio of the difference over the totally uncorrelated events distribution, it was possible to obtain the relative yield of the correlated neutrons per pulse.

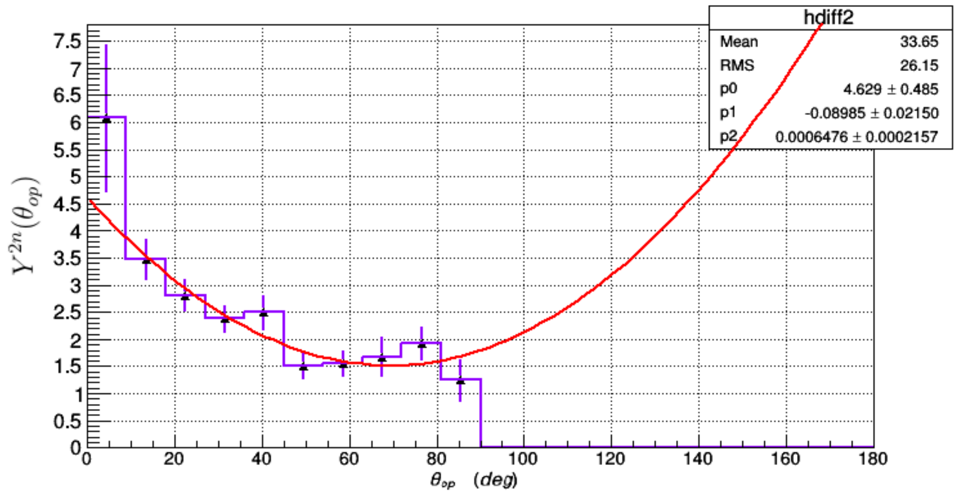

Fig. 2.31. The ratio of the correlated neutron pair yield to the yield of the uncorrelated neutrons. The fitting curve represents one of the possible data trends and should be used as a guide to the eye.

These two distributions of the two neutron opening angle obtained in the case of the photofission process of ^{238}U (see Figs. 2.30 and 2.31) can be qualitatively compared to the modelled distribution of the two neutron opening angle based on the data obtained for the case of neutron fission (see Fig. 2.12). Comparing the main trend of the data presented in these figures, a similar dependence of the higher yield of two neutron events with small values of opening angles (around 0 degrees) and opening angles with large values (around 180 degrees) with respect to the yield of the two neutron detection events with the intermediate values of opening angles (around 90 degrees) can be seen. According to both the experimental data discussed above and the simple model developed in this paper which is based on the data from [22] it can be said that in the process of fission with either neutrons or photons there are preferable configurations in the fissioning system. When two neutrons are emitted by one fission fragment and directed along the initial momentum of the fragment, small opening angles are favored [see Fig. 2.32(a)].

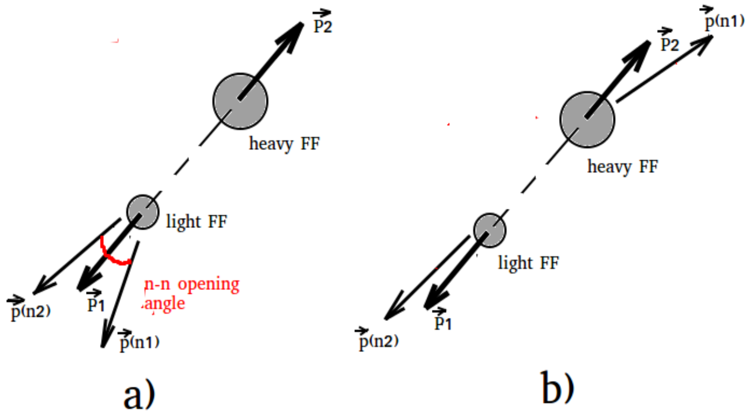

Fig. 2.32. Schematic representation of correlation of prompt neutrons momenta ($\vec{p}(n1)$, $\vec{p}(n2)$) with momenta of fission fragments ($\vec{P}1$, $\vec{P}2$).

Larger neutron opening angles are favored when fission fragments, propagating back-to-back, emit one neutron per fragment with the momentum direction along the initial momentum of the corresponding fission fragment [see Fig. 2.32(b)]. The later kinematics were not probed in these measurements, but will be the subject of future work. The cases when either two neutrons are emitted by one fission fragment with the opening angle close to 90 degrees or each fragment emits one prompt neutron which creates a neutron pair with the opening angle close to 90 degrees are less likely to occur. To prove experimentally the assumptions concerning the yield of opening angles beyond 90 degrees, the experimental setup needs to be modified. The fission model can also be improved. To mention a few main changes, the model can include more precise dependence of neutron multiplicity on the fission fragment mass and prompt neutron energy. Emission of the prompt neutrons can be considered from pre-scission, scission and post-scission configurations to investigate the influence of the fission dynamics on the angular distribution of the prompt neutrons.

The yield of n-n coincidences at a small opening angle could be increased due to the effect of cross talk between the neighbouring detectors. In this case a signal in the detectors is produced by a single neutron scattered from the active area of one detector to the active area of the neighbouring detector.

The effect of the cross talk in this experiment should not affect the experimental data presented in Figs. 2.30 and 2.31 due to the following reasons. First, the neutron scattering on the proton at the angle of 90 degrees is kinematically suppressed according to [38]:

$$E'_n = E_n \cos\theta_L, \tag{2.27}$$

where E'_n is the energy of the scattered neutron, E_n is the energy of the incident neutron, and θ_L is the neutron scattering angle in the laboratory frame. The neutron scattering at 90 degrees could affect the n-n coincidence yield for the neighbouring detectors close to the target where the neutrons hit the detectors almost normally to the surface. The scattering on the ^{12}C which is another component of BC-420 material would not produce a detectable signal due to the kinematics of this interaction. For the detectors placed far from the target, the θ_L differs from 90 degrees such that the neutron could scatter in the direction of the neighbouring detector. However, the simulation of the shielding between the detectors consisted of $4''$ lead $-$ $4''$ borated polyethylene $-$ $4''$ lead showed no transparency for the neutrons with the fission neutron energy spectrum.

Chapter 3

Apparatus

3.1 Data acquisition system

A data acquisition system based on NIM/VME standard equipment was used to process the information obtained in both experiments on the polarized photofission and the two neutron correlation experiment. The data acquisition system was kindly provided and serviced by [39]. A schematic representation of the DAQ is shown in Fig. 3.1.

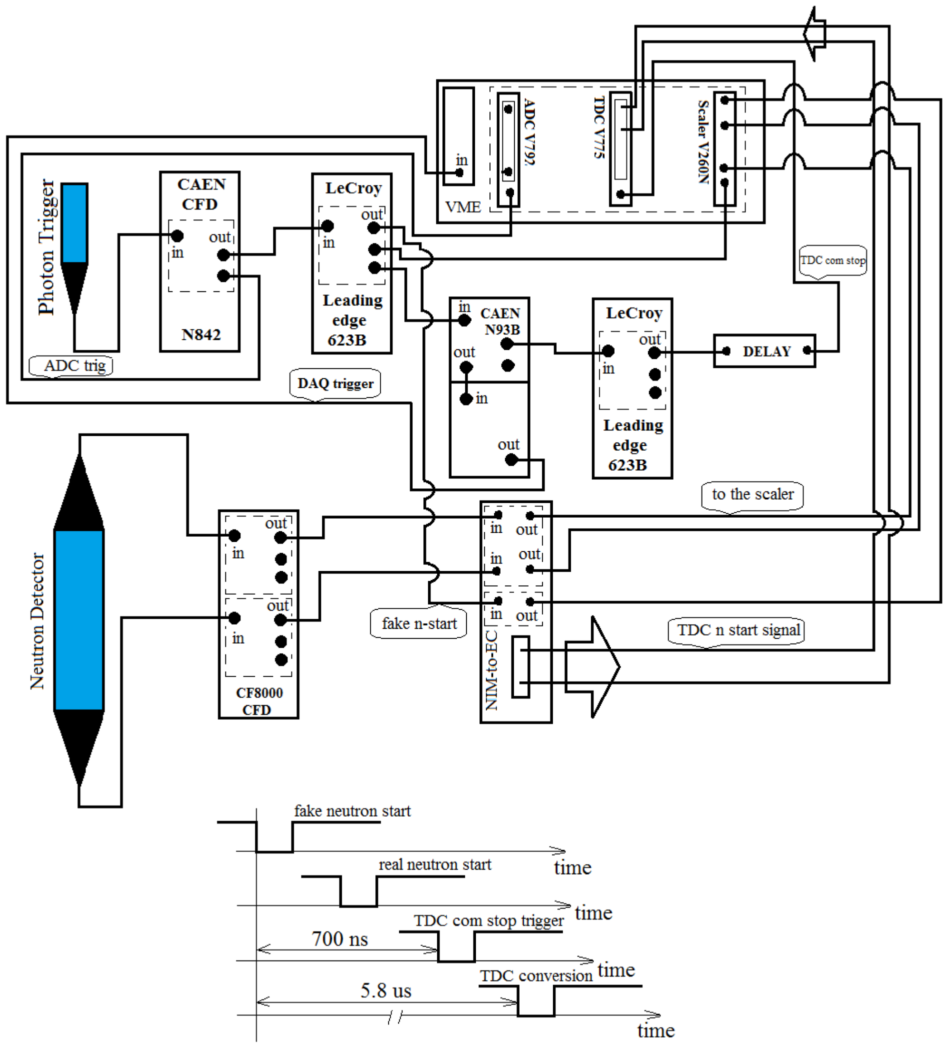

Fig. 3.1. DAQ in "common stop" mode.

Analog signals produced by incident particles in the detectors' PMTs were supplied to an octal constant fraction discriminator ORTEC CF8000 with the thresholds set to the lowest possible values. The logical output signals were negative, 20 ns wide fast NIM-standard pulses, which were sent to a NIM-to-ECL level translator. The level translator was connected to a thirty two channel V775 CAEN multi-channel TDC with a ribbon cable. In the case of the experiment with polarized photofission, the V775 CAEN multi-channel TDC was operated in the common start mode with the timing delays adjusted by two digital delay/pulse generators DG535 with settings described in Appendix A.2. For the two neutron correlation experiment, the V775 CAEN multi-channel TDC was operated in the common stop mode and triggered on a delayed accelerator gun pulse. A VME crate was connected to the computer with CODA software writing the data stream to a hard drive. The neutron time-of-flight was measured with respect to a reference time that was defined in the experiment by the time when photons hit the neutron detector. The relative position of the time-of-flight spectrum on the TDC scale depended on the relative time difference between the detector signals produced by neutrons/photons and periodic common start/stop signal.

It was important to understand the timing behaviour of the gun pulse with respect to the DAQ start trigger signal. The jitter of the gun pulse with respect to the signal created in a plastic scintillator named "Ilyusha" and placed in the beam was about 6.7 ns and is shown in Fig. 3.2 (right panel). This finite distribution width can be considered as an additional source of the uncertainty in the neutron energy spectrum together with the width of the photon peak in the neutron time-of-flight spectrum and detector resolution uncertainty.

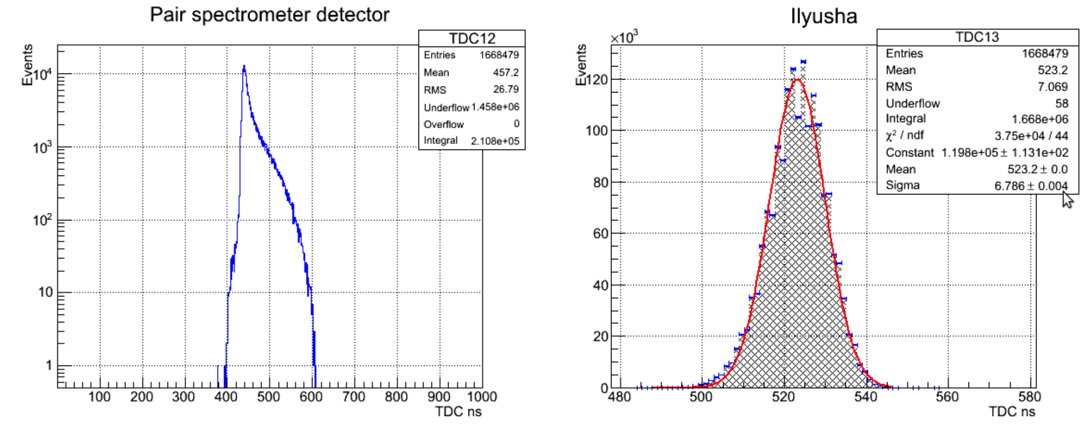

Fig. 3.2. Gun pulse jitter.

The timing correlation of the DAQ start signal taken to be the gun pulse and the positron signal obtained with the relative photon flux monitor is pictured in Fig. 3.2 (left panel).

3.2 Neutron detector design

A schematic design of the neutron detectors for the experiment to measure two neutron correlations in photofission is shown in Fig. 3.3. The need to obtain information on the neutron position as it hits the detector required relatively large active volume which was made to be $75 \times 14.8 \times 3.8$ cm^3. Two light guides were glued with optical glue to both ends of the scintillator to increase the efficiency and uniformity of the light collection. The dimensions of the light guide were $12.5 \times 14.8 \times 3.8$ cm^3. Then the assembly was wrapped with light reflective material (Tyvek) and made light tight leaving openings for the PMTs which were attached to each light guide with the help of optical couplant (optical cookies). In order to provide mechanical stiffness and good optical contact, holders were designed to support photomultiplier tubes and create some pressure on the PMTs against the optical cookie (see Fig. 3.3).

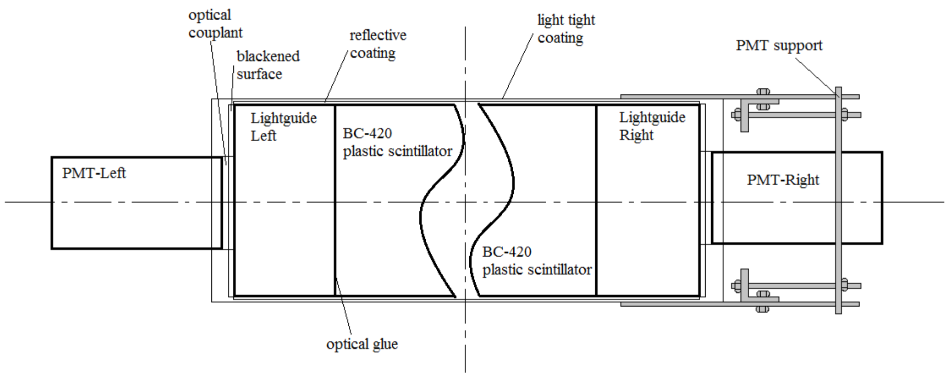

Fig. 3.3. Neutron detector sketch.

For the experiment using the polarized photon beam to initiate photofission, nine detectors were used, each having active volume of $5 \times 7.3 \times 7.3$ cm^3. The plastic scintillator BC-420 was viewed via a Photonis XP2262/B photomultiplier tube. The photomultiplier was attached to the scintillator with the help of an optical cookie used as an optical couplant. The scintillator was polished and wrapped in aluminium foil to reflect the light produced during the interaction of the neutrons with the scintillation material and improve the efficiency of the light collection. A schematic view of the detector assembly is shown in Fig. 3.4.

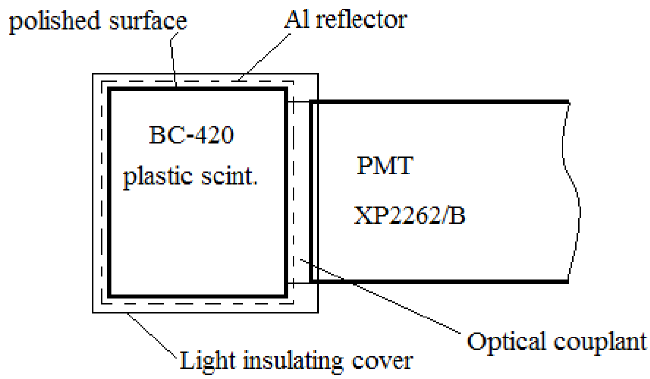

Fig. 3.4. Neutron detector design sketch.

The mechanism of neutron detection is the same as described in Sec. 2.4.1.

3.3 Photon flux monitoring

In order to monitor the relative photon flux during the experiment, a separate technique was used that allowed us to measure the relative number of positrons produced by the incident photons. Permanent magnets placed parallel to each other creating a vertical B-field were used to form the spectrometer analysing magnet. The air gap between the sweep magnet placed inside the experimental hall and pair spectrometer magnet was used as a pair converter. The effect of deflection of a charged particle in a magnetic field was applied to deflect positrons with the analysing magnet, and send them toward the positron detectors.

The positron detector consisted of BC-420 plastic scintillator attached to a light guide which was in turn attached to a photomultiplier tube. Additional lead shielding was placed around the positron detector to provide the irradiation of the active area only.

As an example, the data on the relative photon flux obtained with the photon flux monitor is presented in Fig. 3.5. Observing the relative change in positron count rate, it is possible to find the relative change of the photon flux and adjust the electron current of the accelerator respectively.

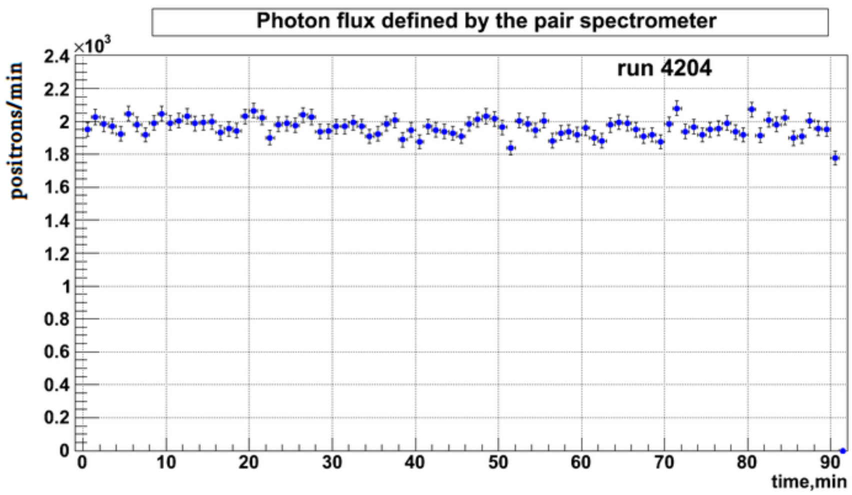

Fig. 3.5. An example of the data obtained via the photon flux monitor for run 4204 that was 90 minutes long.

It should be noted that the $e^{-}-e^{+}$ pair production reaction has a threshold on the photon energy of about 1.02 MeV. Hence, the pair spectrometer is insensitive to the photon flux change in the case the photon energies are below the threshold value.

Chapter 4

Photofission with polarized photons

4.1 Investigation of photofission with polarized photons

It has been experimentally observed that if the fission of a nucleus is caused by high energy unpolarized photons, then the angular distribution of fission fragments is anisotropic. In particular, the number of fission fragments detected 90 degrees to the photon beam was larger than the number of fission fragments detected in either forward or backward directions. Quantitative measurements of the fission fragment angular distribution were made in 1956 [40]. It was found that the experimental angular distribution of fission fragments can be fit by the following curve:

$$W(\theta) = a + b\sin^2(\theta), \tag{4.1}$$

where θ is the angle between the fission fragment and the photon beam, and the b/a ratio depends on the photon beam energy, the target material, and the type of fission fragments being observed.

The general expression for the fission fragment angular distribution function has the following form ($L = J \leq 2$) in the case of an unpolarized photon beam [1, p. 111]:

$$W^J_{M=\pm1,K}(\theta) = A_0 + A_2 \cdot P_2(\cos\theta) + A_4 \cdot P_4(\cos\theta). \tag{4.2}$$

In the case of a linearly polarized photon beam, the angular distribution function depends on both polar (θ) and azimuthal (ϕ) angles. Here one should make a transformation:

$$P_\nu(\cos\theta) \rightarrow P_\nu(\cos\theta) + \omega_L \cdot P_\gamma \cdot f_\nu(L, L) \cdot \cos 2\phi \cdot P^2_\nu(\cos\theta), \tag{4.3}$$

where P^2_ν are the associated Legendre polynomials, $f_\nu(L, L)$ are coupling coefficients, $\omega_L = +1(-1)$ for electric (magnetic) transitions and P_γ is the degree of linear polarization of the photon beam. After making the previous transformation, one will get the angular distribution function which depends on θ and ϕ angles:

$$\begin{aligned} W^J_{M=\pm1,K}(\theta, \phi) = a + b \cdot \sin^2\theta + c \cdot \sin^2(2\theta) + \\ + \omega_L \cdot P_\gamma \cdot \cos 2\phi \cdot (d \cdot \sin^2\theta - 4c \cdot \sin^4\theta). \end{aligned} \tag{4.4}$$

The main aim of this portion of the thesis is to obtain the experimental angular distribution of prompt neutrons emitted in the process of photofission generated by linearly polarized photons for various target materials, and relate that angular distribution with the known angular distribution of the fission fragments. If the angular asymmetry of prompt neutrons is reflected in the one for fission fragments, it will be possible to say that the process of fission happened without direct detection of fission fragments.

4.2 Review of past work on photofission with polarized photons

4.2.1 Data on the photofission with unpolarized photons

The first observation of the asymmetry of fission fragments was quantitatively described by E. J. Winhold and I. Halpern [40]. They measured the angular distribution of fission fragments produced by unpolarized photons and found the dependence described by Eq. (4.1).

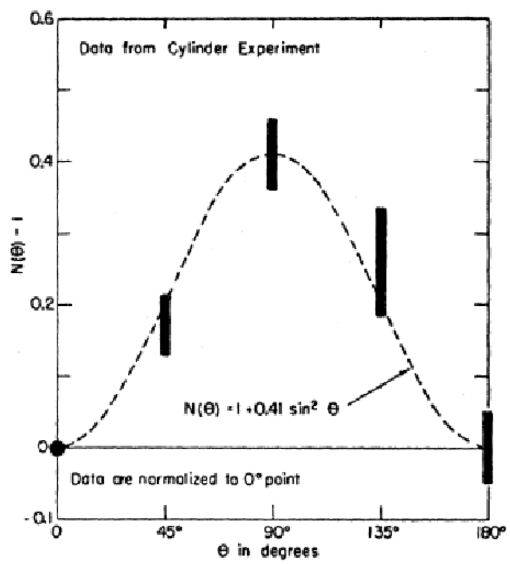

Fig. 4.1. Asymmetry of fission fragment emission. End point energy is 16 MeV. Figure was taken from [40].

It was observed that more fission fragments were emitted at 90 degrees with respect to the beam direction (see Fig. 4.1). Neutrons, protons, and α-particles used to induce fission created the same effect of asymmetry of angular distribution of fission fragments. ^{232}Th was used as a target and fission fragments emitted from the target were detected by a plastic catcher. Then the angular distribution of the fission fragments was determined by the measurement of β-activity distribution in the plastic. An anisotropic angular distribution was also induced by photons with energies within about 3 MeV of the fission threshold and the photons with energies in the giant dipole resonance region produced an isotropic angular distribution of the fission fragments. The authors investigated the angular distribution of the fission fragments in the photofission process for different target materials and found that (a) the asymmetry was observed for certain fissionable targets, (b) to produce the anisotropy, the energy of the photons should be within a couple of MeV of threshold, (c) the targets that generate anisotropic fission have different fission cross sections than the ones which do not generate anisotropic fission, (d) the mass ratio and the anisotropy of the observed fission fragments are correlated.

These findings can be explained in the following way [40]. According to Bohr's considerations, a collective rotation of a nucleus defines the orbital motion of the fission fragments. In the case of photofission of even-even nuclei (^{232}Th, ^{238}U) there is an absorption of dipole photons and the nuclei pass through the 1^- collective state where the nuclear symmetry axis is perpendicular to the vector of angular momentum. The fission fragments are preferentially emitted perpendicularly to the vector of angular momentum/photon beam axis because the nucleus rotates perpendicularly to the angular momentum in the state described. The excitation energy of even-even nuclei should be near the "threshold" to be able to observe the fission fragment emission angular asymmetry. If the excitation energy is above the "threshold" by a couple of MeV there will be many different 1^- states available at the saddle point and as a consequence the symmetry axis of a nucleus loses preferred orientation with respect to the nuclear angular momentum, so the angular distribution of fission fragments becomes isotropic. In the case of odd-A nuclei (^{235}U) they have a large spin in their ground states. A dipole absorption will orient the nuclear angular momentum isotropically with respect to the photon beam axis such that the angular distribution of fission fragments is isotropic. Also, since the concentration of the energy levels around the saddle point for odd-A nuclei is expected to be larger than in the case of even-A nuclei, the spin of odd-A nuclei is carried away by single nucleons rather than being converted into collective oscillations.

In Ref. [41], the authors investigated the dependence of the angular distribution of fission fragments versus the end point energy of bremsstrahlung radiation that was obtained in the photofission process of ^{238}U nuclei via unpolarized photons. The photon beam was produced in the process of bremsstrahlung radiation with an end point energy $\sim$5.5 MeV. The results of the measurement are presented in Fig. 4.2 below.

The authors noticed an increase in the contribution of the isotropic component of the angular distribution function with a decrease of the end point energy. The angular distribution of the fission fragments is dominated by the quadrupole component, hence, in all the processes that occur at low energies of bremsstrahlung photons the main role is defined by the 2^+ states of the ^{238}U nucleus. The main conclusion of [41] was that the isotropy in the fission fragment angular distribution showed that the fission of ^{238}U happens from the ground state located in the

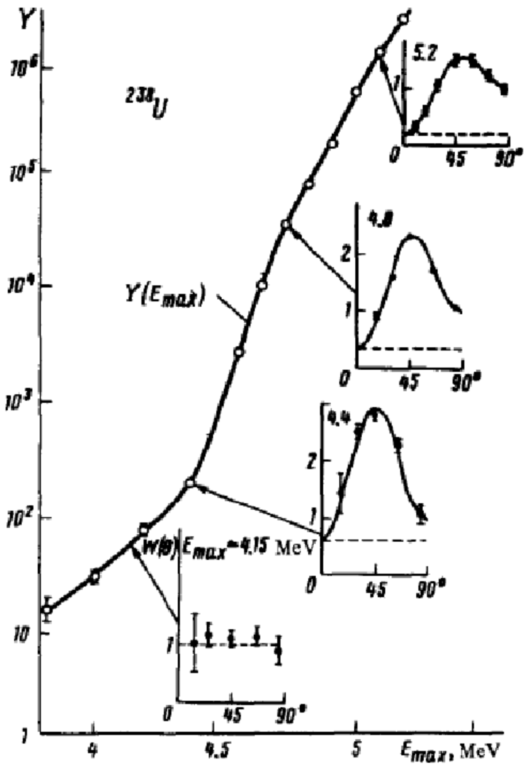

Fig. 4.2. The yield and angular distribution of fission fragments as a function of the bremsstrahlung end-point energy. Picture was taken from [41].

second well of the potential barrier.

As a further investigation of photofission of ^{238}U, Ref. [42] can be considered. The authors investigated photofission of ^{238}U via monochromatic unpolarized γ-rays in the energy range 11-16 MeV. In order to provide monochromatic γ-rays they used the tagged photon technique. They observed the angular distribution of the fission fragments pictured in Fig. 4.3.

The solid line here represents a least-squares fit of the experimental data and can be described by:

$$W(\theta) = a + b \cdot \sin^2 \theta + c \cdot \sin^2 2\theta. \tag{4.5}$$

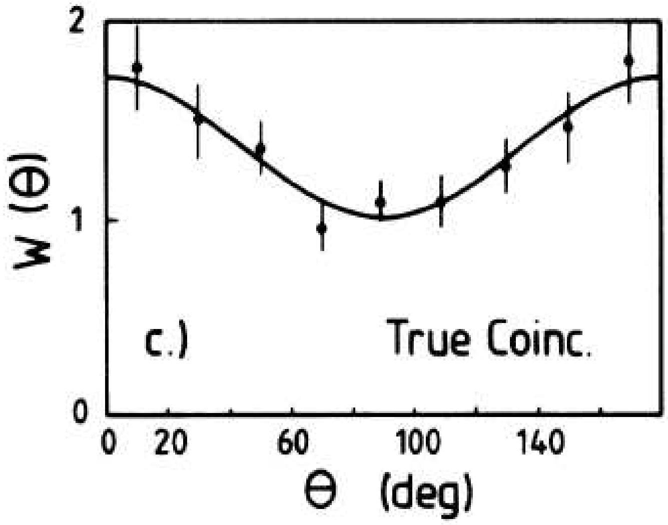

Fig. 4.3. The fragment angular distribution for true coincidences. E_γ = 11.3 MeV. Picture was taken from [42].

The authors claim that this function can be used to describe the angular distribution of photofission fragments in the case of dipole and quadrupole excitation. They have not observed quadrupole contributions and the coefficient c in the fits was always zero.

It was also observed that the angular correlation coefficient b deduced from the angular correlations as a function of the photon energy in the region of the threshold for the second chance fission was equal to zero except for the two values of photon energy 11.3 and 12.6 MeV (see Fig. 4.4).

The authors claim that it was the first time that large anisotropies were observed at such high energy of the photon beam. They qualitatively explained that the anisotropies are due to "near-barrier fission of the residual compound nucleus after neutron emission, ^{237}U". Also it was found that there is a profound anisotropy for different mass regions in the fission fragment mass distribution spectrum (see Fig. 4.5).

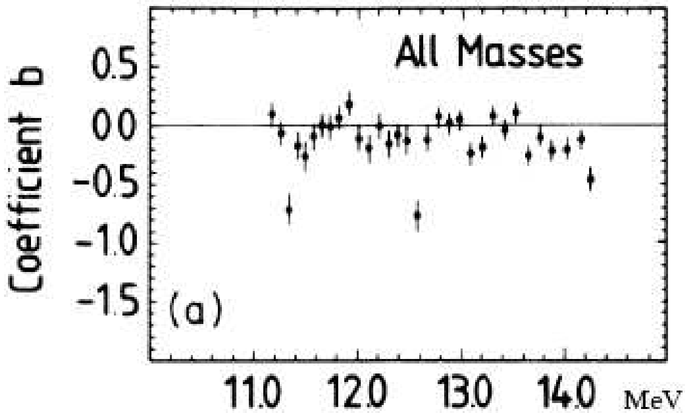

Fig. 4.4. The angular correlation coefficient b as a function of photon energy. Picture was taken from [42].

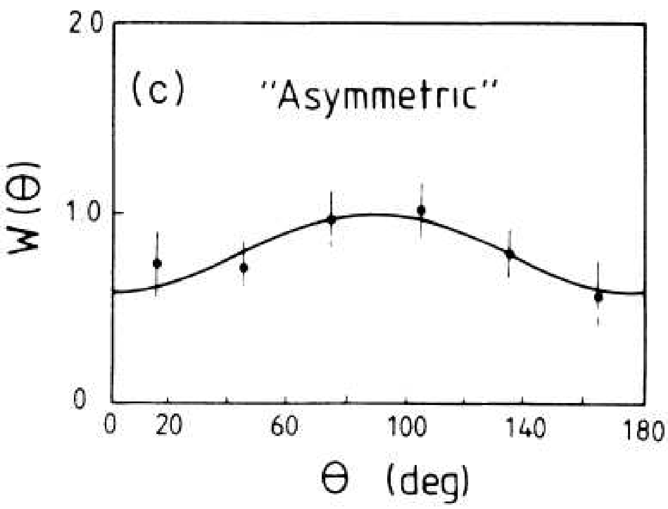

Fig. 4.5. The fragment angular distribution in the (γ, f) reaction at E_γ = 12.13 MeV for a "far-asymmetric" mass split region. Picture was taken from [42].

4.2.2 Data on the photofission with linearly polarized photons

Implementation of a polarized photon beam can improve our understanding of the physics of the photofission process. The first experimental results on the photofission of ^{232}Th via polarized photons with $P_\gamma = 0.3$ and $E_\gamma = 10$ MeV were presented in Ref. [43]. The theoretical dependence of the angular distribution functions versus θ-angle for dipole and quadrupole excitations was calculated using the following expression:

$$\begin{aligned} W(\theta,\phi) = a + b\cdot\sin^2\theta + c\cdot\sin^2 2\theta + \\ + \omega\cdot P_\gamma\cdot\cos 2\phi\cdot(d\cdot\sin^2\theta - 4c\cdot\sin^4\theta) \end{aligned} \tag{4.6}$$

and the results are presented in Fig. 4.6 below. The values of the coefficients a, b, c, and d were determined.

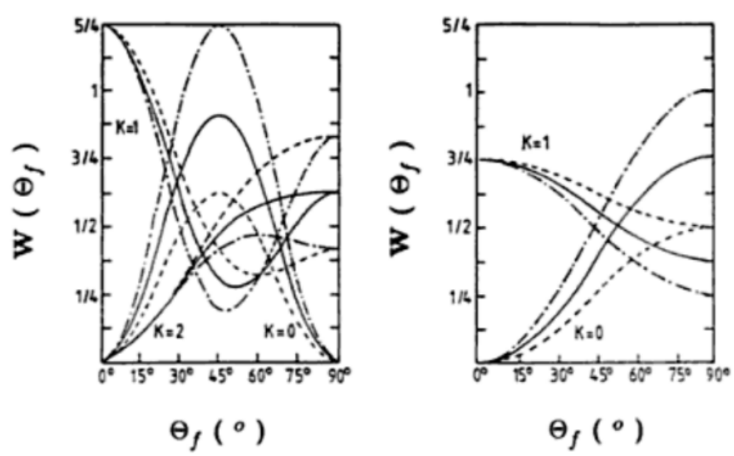

Fig. 4.6. The fragment angular distribution in the (γ, f) reaction for an even-even nucleus using linearly polarized photons. Left: electric quadrupole excitation, right: electric dipole excitation. Full lines represent angular distribution for unpolarized photons. Dashed lines: polarized photons using, $\phi = 90°$. Dashed-dotted lines: polarized photons using, $\phi = 0°$. Picture was taken from [1].

Experimental measurements of the angular distribution for fission fragments created by linearly polarized photons are provided below for a ^{232}Th target (see Fig. 4.7). It can be seen that the electric dipole excitations occur predominantly.

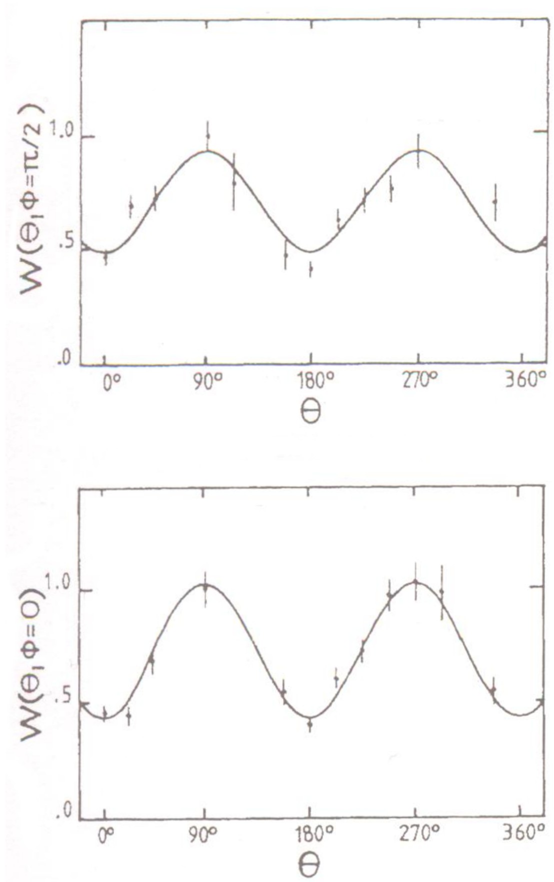

Fig. 4.7. The angular distribution asymmetry for fission fragments created by linearly polarized photons. Picture was taken from [43].

In Ref. [44] the authors found optimal energies of the linearly polarized photons to observe asymmetries in angular distribution of fission fragments for ^{234,236,238}U and ^{238,240,242}Pu isotopes. Also they calculated the asymmetry coefficients of the fragments' angular distributions. The asymmetry function of the fission fragments with respect to the photon beam line was defined as:

$$W(\theta,\phi) = \frac{d\sigma_{\gamma,f}(\theta,\phi)/d\Omega}{d\sigma_{\gamma,f}(\pi/2,\pi/4)/d\Omega}, \tag{4.7}$$

where

$$\frac{d\sigma_{\gamma,f}(\theta,\phi)}{d\Omega} = a_0 + b_0\sin^2\theta + c_0\sin^2(2\theta) + P_\gamma\cos 2\phi(d_0\sin^2\theta - 4c_0\sin^4\theta). \tag{4.8}$$

The actual asymmetry coefficients used in the paper were linear combinations $a = \frac{a_0}{a_0+b_0}$, $b = \frac{b_0}{a_0+b_0}$, $c = \frac{c_0}{a_0+b_0}$, and $d = \frac{d_0}{a_0+b_0}$. The coefficient d was calculated using experimental values of the coefficient a, b and c obtained for fission of ^{234,236,238}U and ^{238,240,242}Pu isotopes via unpolarized photons with $E_\gamma = 4-10$ MeV and the asymmetry $\Sigma(\theta=\pi/2) = -\frac{b/a}{b/a+1}$ for the fission process caused by linearly polarized photons with $E_\gamma = 10-26$ MeV. After investigation of the energy dependence of b/a, d/b, and $d/4c$ (see Fig. 4.8 as an example) it was

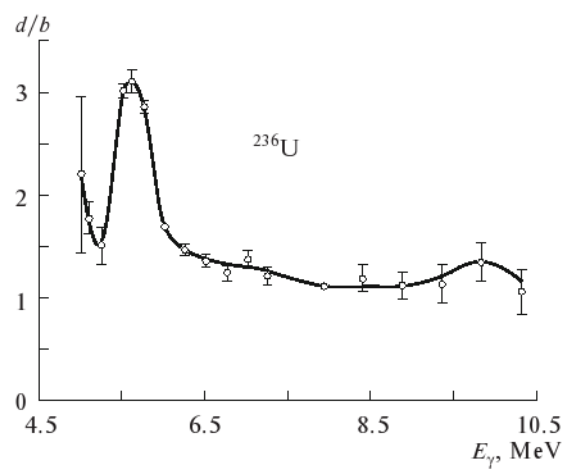

Fig. 4.8. Dependence of the ratio d/b of the fragments' angular distribution asymmetry coefficients for fission by linearly polarized photons on the photon energy. Picture was taken from [44].

found that the polarization term increases its contribution to $W(\theta,\phi)$ with an increase of photon energy starting from 4 MeV, and reaches its maximum value at the optimal energies for observation of polarization effects: (a) 5.25-6.0 MeV for ^{238}Pu, (b) 5.0-5.5 MeV for ^{238}U, (c) 5.6-6.2 MeV for ^{234}U, (d) 4.3-6.0 MeV for ^{236}U. In the range of photon energies optimal for observation of the polarization part in the photofission asymmetry $W(\theta,\phi)$, the maximum value of the deviation of $\frac{W(\theta,\phi)-W(\theta)}{W(\theta)} \cdot 100\%$ is equal to 70-100% for the polarization $P_\gamma = 1$ and decreases to 20-30% for the polarization $P_\gamma = 0.3$. The contribution of the polarization term to the fission fragments' angular distribution asymmetry decreases with photon beam energy increase and at $E_\gamma \geq 15$ MeV the quadrupole channel's contribution vanishes (coefficient $c \approx 0$). Thus the angular distribution of fission fragments for linearly polarized photons becomes close to isotropic ($b/a \ll 1$) and coefficients d and b become equal. For example, for the case ^{238}U at $E_\gamma = 26$ MeV the ratio $b/a = 0.06$.

More recent experiments determined the fission fragment angular distribution and prompt neutron angular asymmetry in the photofission reaction on different heavy actinide targets irradiated with nearly monoenergetic 100% linearly polarized photons [45, 46]. The photon beam in these experiments was produced by scattering of electrons on laser photons using the high γ-ray source $Hi\gamma S$ facility at Triangle Universities Nuclear Laboratory [13]. In the experiment described in [46] fissionable targets such as ^{232}Th and ^{238}U were used to observe the angular distribution of fission fragments after photofission. Large angular asymmetries of the prompt neutrons emitted by fission fragments were detected using an array of detectors based on paired liquid scintillators and photomultipliers placed at different polar (θ) and azimuthal (ϕ) angles. The neutron emission asymmetry was calculated as:

$$\Sigma(\theta) = \frac{W(\theta, \phi = 0) - W(\theta, \phi = \pi/2)}{W(\theta, \phi = 0) + W(\theta, \phi = \pi/2)},$$

where $W(\theta, \phi)$ is the function that describes the angular distribution of fission fragments created in the photofission reaction. Neglecting quadrupole fission channels the asymmetry function was represented as:

$$\Sigma(\theta) = \frac{\frac{b}{a}\sin^2(\theta) + \frac{c}{a}\sin^2(2\theta)}{1 + \frac{b}{a}\sin^2(\theta) + \frac{c}{a}\sin^2(2\theta)},$$

where a, b, and c are the coefficients of the $W(\theta, \phi)$ function [46]. By fitting the experimental angular distributions it was possible to extract information on the fit parameters b/a and c/a where the coefficient a was set to $a = 1 - b$ for the proper normalization. It was obtained that $b = 0.433 \pm 0.011^{statistical} \pm 0.006^{systematic}$ and $c = -0.012 \pm 0.017^{statistical} \pm 0.009^{systematic}$.

In Ref. [45] the author used the photofission of ^{233,235,238}U, ^{237}Np, and ^{239,240}Pu. The photon beam in these experiments was also produced by scattering electrons on a free electron laser beam using the $Hi\gamma S$ facility. The angular distribution of the fission fragments created in the process of photofission with nearly monochromatic photons with polarization close to 100% was measured using a scattering chamber with microstrip detectors as detecting elements. The authors of [45] provided information on the correlation of the angular distribution function coefficient b_f for fission fragments created in the photofission with polarized photons and the coefficient b_n obtained from the analysis of the angular distributions of prompt neutrons in the photofission process (see Fig. 4.9). It can be seen that the angular distribution of the prompt fission neutrons is correlated with the angular distribution of fission fragments.

In the paper [13] it was found that the angular distribution of prompt neutrons produced during the photofission is anisotropic. However, the anisotropy

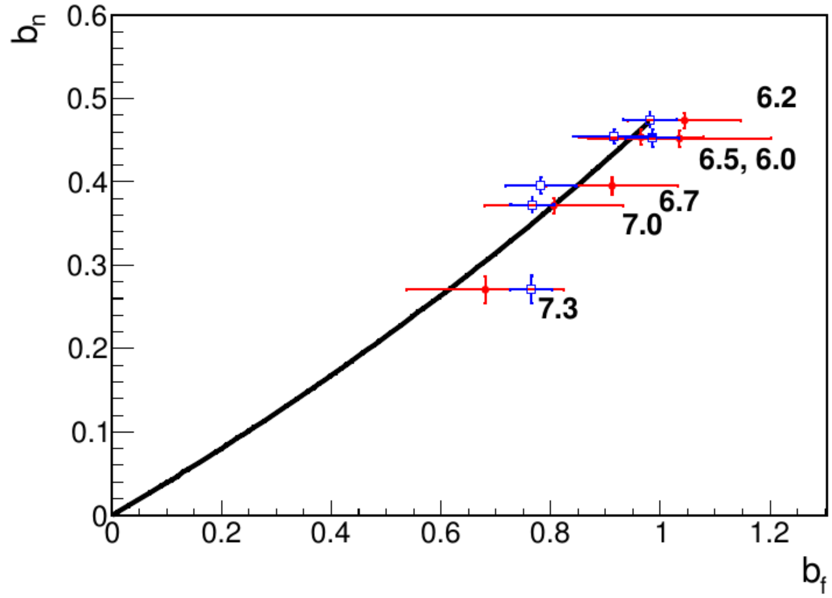

Fig. 4.9. Correlation of the parameters b_n and b_f describing prompt fission neutrons and fission fragments angular asymmetries. Solid line represents the result of a simple kinematical model. Picture was taken from [45].

of the prompt neutrons was substantially lower than the anisotropy in angular distribution of fission fragments.

4.3 Experimental methods

4.3.1 Polarized gamma beam

Bremsstrahlung kinematics

In the current research work, we produced polarized photons using the effect of partial polarization of off-axis photons created by electron scattering in the nuclear Coulomb field. This effect is called electron bremsstrahlung [47].

Let us consider the process of bremsstrahlung photon emission closer. In the elementary process of bremsstrahlung, energy conservation gives the following expression for the momentum given to a nucleus by the incident electron:

$$\vec{q} = \vec{p}_1 - \vec{p}_2 - \vec{k}, \tag{4.9}$$

where $\vec{p}_1$ is the momentum of the incident electron, $\vec{p}_2$ is the momentum of the scattered electron, and $\vec{k}$ is the momentum of the bremsstrahlung photon. Here we are talking about elastic bremsstrahlung, where the target nucleus is in the ground state before and after the electron scattering.

According to [47, p. 27] the recoil energy of the target nucleus $E_{recoil} \approx (\vec{q})^2/(2M)$ can be omitted in the consideration if the incident electron energy is $E_0 \ll \frac{1}{2}Mc^2 \approx 469$ A MeV. In this case we have the following relation of energies of the particles involved in the bremsstrahlung process:

$$h\nu = E_0 - E_e, \tag{4.10}$$

where $h\nu$ is the energy of the emitted photon. In the experiment we used $E_0 =$ 25 MeV electrons incident on a 1 mil (25 μm) aluminium radiator (A = 27). Hence 25 (MeV) $\ll 469 \cdot 27$ (MeV) = 12663 MeV and we can neglect the recoil energy of the target nucleus.

Angular and energy distribution of bremsstrahlung radiation

The energy spectrum of bremsstrahlung radiation produced by 25 MeV electrons is presented in Fig. 4.10 and has a shape of a Bethe-Heitler spectrum.

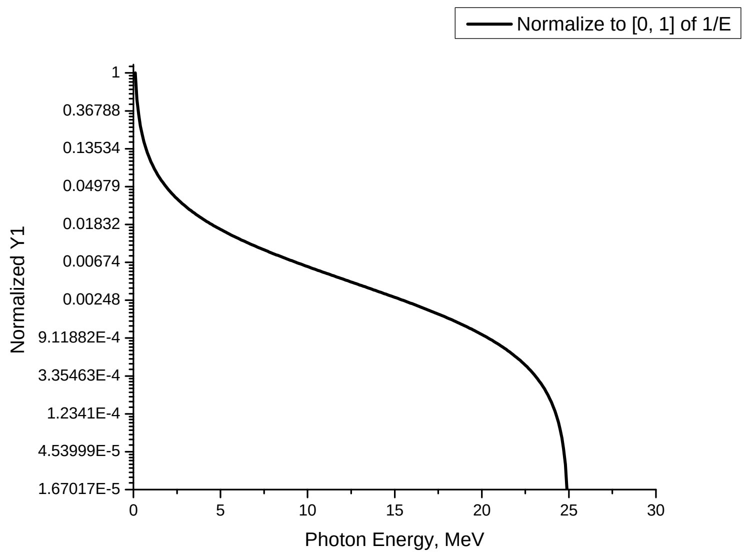

Fig. 4.10. Bremsstrahlung spectrum produced by 25 MeV electrons.

The angular distribution of the bremsstrahlung photons in the elementary bremsstrahlung event shows a maximum at a specific polar angle measured with respect to the direction of the incident electrons [47, p. 97]. The expression for the angular distribution of bremsstrahlung radiation can be obtained by parametrizing the experimental data as:

$$\frac{dN}{d\theta} = \frac{\frac{E\theta}{\mu}}{[1 + (\frac{E\theta}{\mu})^2]^2}, \tag{4.11}$$

where E is the energy of the incident electrons, $\mu = mc^2 = 0.511$ MeV is the rest energy of the electron, and θ is the angle of observation of the bremsstrahlung radiation [48, 49]. It can be seen that the angular distribution of the bremsstrahlung radiation is anisotropic. The distribution of bremsstrahlung photons $dN/d\theta$ as a function of the observation angle θ is presented below in Fig. 4.11.

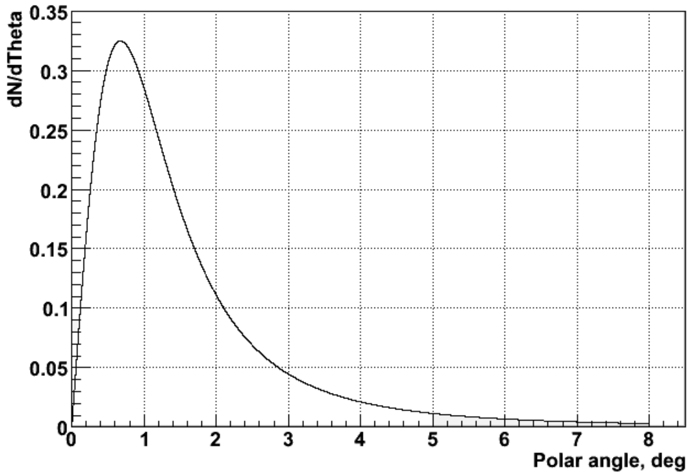

Fig. 4.11. $\frac{dN}{d\theta}$ distribution as a function of the observation angle θ sampled for the case $\mu/E = 0.02044$.

Bremsstrahlung Cross Section

The bremsstrahlung cross section summed over the polarization of the outgoing photons, can be found using the Dirac theory of the electron [50, p. 1026] and can be described by the Bethe-Heitler formula obtained in the Born approximation [47, p. 44]:

$$\begin{aligned}\frac{d^3\sigma_B}{d\Omega_k d\Omega_{p_2} dk} = \frac{\alpha Z^2 r_0^2}{\pi^2}\frac{p_2}{kp_1q^4}\Bigg\{&\frac{4\epsilon_2^2 - q^2}{D_1^2}(\vec{p}_1 \times \vec{k})^2 + \frac{4\epsilon_1^2 - q^2}{D_1^2}(\vec{p}_2 \times \vec{k})^2 \\ &- 2\frac{4\epsilon_1\epsilon_2 - q^2}{D_1 D_2}(\vec{p}_1 \times \vec{k}) \cdot (\vec{p}_2 \times \vec{k}) + \frac{2k^2}{D_1 D_2}(\vec{q} \times \vec{k})^2\Bigg\}\end{aligned}, \qquad (4.12)$$

where k is the energy of the emitted photon, α is fine structure constant, Z is the atomic number of the target element, r_0 is classical electron radius, $\vec{q}$ is the recoil momentum of the target nucleus, $\vec{p_1}$ is the momentum of the incident electron, $\vec{p_2}$ is the momentum of the scattered electron, ϵ_1 is the total energy of the incident electron, ϵ_2 is the total energy of the scattered electron, $d\Omega_{p_2}$ is the element of solid angle in the direction of the momentum of the scattered electron $\vec{p_2}$, and $d\Omega_k$ is the element of solid angle in the direction of the momentum of the emitted photon $\vec{k}$. Coefficients D_1 and D_2 are defined in the following way: $D_1 = 2(\epsilon_1 k - \vec{p_1} \cdot \vec{k})$, $D_2 = 2(\epsilon_2 k - \vec{p_2} \cdot \vec{k})$ with the same meaning of the parameters as defined above.

According to [51, p. 334], the differential cross section for the bremsstrahlung process where a polarized photon is emitted with momentum $\vec{K}$ and polarization direction $\hat{\epsilon}$ into a solid angle $d\Omega_K$ can be described by the following equation:

$$\begin{aligned}\frac{d^3\sigma}{d\Omega d\Omega_K dK} = {} & \frac{\alpha Z^2 r_0^2}{(2\pi)^2}\left[\frac{1-F(q)}{q^2}\right]^2 \frac{P_2}{P_1}\frac{1}{K} \\ & \times \left\{ 4\left[\frac{E_1}{\Delta_2}(\vec{P_2}\cdot\hat{\epsilon}) - \frac{E_2}{\Delta_1}(\vec{P_1}\cdot\hat{\epsilon})\right]^2 \right. \\ & - q^2\left[\frac{1}{\Delta_2}(\vec{P_2}\cdot\hat{\epsilon}) - \frac{1}{\Delta_1}(\vec{P_1}\cdot\hat{\epsilon})\right]^2 \\ & \left. + K^2\left[2 + \frac{q^2}{\Delta_1\Delta_2} - \frac{\Delta_1}{\Delta_2} - \frac{\Delta_2}{\Delta_1}\right]\right\},\end{aligned} \tag{4.13}$$

where $\vec{P_1}$ is the initial momentum of the incident electron, $\vec{P_2}$ is the final momentum of the scattered electron, $E_{1,2}^2 = 1 + P_{1,2}^2$, $\Delta_{1,2} = E_{1,2} - P_{1,2}\cos(\theta_{1,2})$, $\vec{P_{1,2}} \cdot \vec{K} = P_{1,2}K\cos(\theta_{1,2})$, $\vec{q}$ is the momentum transferred to the nucleus of the target material defined as $\vec{q} = \vec{P_1} - \vec{P_2} - \vec{K}$. The effect of the screening of the atomic nucleus can be taken into account by calculating the atomic form factor $F(q)$.

Generally the polarization degree of bremsstrahlung photons produced in a real experiment and observed via the angular distribution of products of the analyzing reaction is limited by the finite angular dimensions of the target since there is an angular dependence of the bremsstrahlung polarization, and by the energy dependence of the reaction under study since not all the photon energy can be used to generate a specific analyzing reaction. These properties of the bremsstrahlung behaviour will be described in the next section.

Polarization Calculation

In the bremsstrahlung process, the emitted photons can have linear and circular polarization. These properties can be revealed in experiments with variable production conditions [52]. In this paper only the linear polarization is considered.

For electrons with *non-relativistic* energies, the bremsstrahlung linear polarization is closely related to the electron orbital angular momentum [52]. In the case of bremsstrahlung with low energy, the radiation consists predominantly of electric dipole radiation with the electric field vector parallel to the emission plane. A high energy bremsstrahlung radiation source can be described as an electric dipole oscillating parallel to the momentum of the incident electron and, thus, with electric field vector perpendicular to the emission plane. The low energy bremsstrahlung (low frequency photons with $k \sim 0$) emission would correspond to the radiation source oscillating perpendicular to the momentum of the incident electron. These conditions can be visualised as shown in Fig. 4.12.

The photons with low energies will be predominantly polarized perpendicular to the emission plane, and high energy photons will be predominantly polarized parallel to the emission plane [47].

For electrons with *relativistic* energies (E_e >5 keV), the bremsstrahlung linear polarization is affected not only by the orbital angular momentum of the incident electron but also by the electron spin angular momentum. The effects of interference of spin and orbital currents play an important role in the process

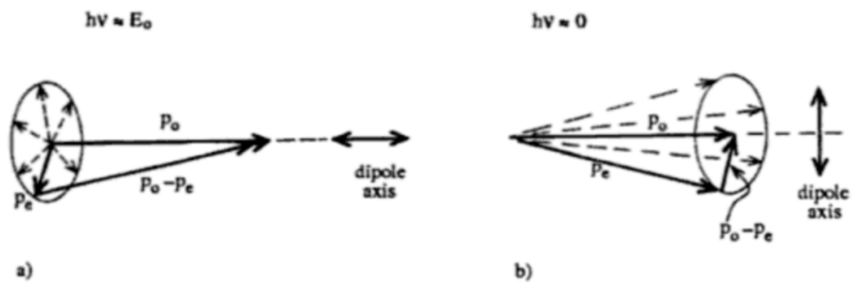

Fig. 4.12. Orientation of the dipole axis in the case of high frequency radiarion (part (a)) and low frequency radiation (part (b)). P_0 is the momentum of the incident electron and P_e is the final momentum of the electron after the bremsstrahlung interaction. Picture was taken from [47].

of production of high frequency radiation. This interference is the reason for the decrease of the polarization parallel to the emission plane [52].

In this part of thesis, the approach on the definition of the average linear polarization of bremsstrahlung photons produced by 25 MeV unpolarized electrons incident on an Al bremsstrahlung converter with arbitrary polarization direction is described. The final polarization spectrum of the photon beam is weighted by the collimator angular resolution, by the angular distribution of bremsstrahlung photons, and by the yield of the bremsstrahlung photons. In order to understand the polarization of the real beam of the bremsstrahlung photons, it is necessary first to understand how the polarization depends on the photon emission angle and the energy of photons. For this purpose the results from several papers were utilized.

The authors of [53] used spin formalism to calculate the absolute square of the bremsstrahlung matrix elements. For high energy bremsstrahlung, *i.e.*, the process where angular momenta $l >> 1$ are significant, they used the Sommerfeld-Maue type of wave function to describe the electrons:

$$\psi_{\pm} = e^{i\vec{p}\cdot\vec{r}}(1 - \frac{i\vec{\alpha}\cdot\nabla}{2\epsilon})uF_{\pm}, \tag{4.14}$$

where $\vec{p}$ is the electron momentum, ϵ is the electron energy, $\vec{\alpha}$ is the Dirac operator, $\vec{r}$ is the electron coordinate, and u is the spinor of free particle. $F_{\pm}$ represent the solution of:

$$(\nabla^2 + 2i\vec{p}\cdot\nabla - 2\epsilon V)F = 0, \tag{4.15}$$

with normalization $F(r) \to 1$ as $r \to \infty$. It is possible to find the solution of F for both unscreened and screened Coulomb potentials.

Following [53], *i.e.*, calculating bremsstrahlung matrix elements and the differential cross section of the bremsstrahlung process, it is possible to find the bremsstrahlung radiation cross section summed over the polarization directions ([53], Eq. (7.2)):

$$d\sigma(\vec{p}_1, \vec{k}) = 2Z^2\frac{e^2}{hc}(\frac{e^2}{mc^2})^2\frac{dk}{k}\frac{d\zeta}{\epsilon_1^2}\{(\epsilon_1^2 + \epsilon_2^2)(3 + 2\Gamma) - 2\epsilon_1^2\epsilon_2^2(1 + 4u^2\zeta^2\Gamma)\}. \tag{4.16}$$

The expression for linear polarization can be written as:

$$P = \frac{d\sigma_{\perp} - d\sigma_{\parallel}}{d\sigma_{\perp} + d\sigma_{\parallel}}, \tag{4.17}$$

where $d\sigma_{\perp}$ is the cross section for bremsstrahlung polarized perpendicular to the emission plane and $d\sigma_{\parallel}$ is the cross section for bremsstrahlung polarized parallel to the emission plane. Finally the polarization degree of bremsstrahlung radiation can be found as ([53], Eq. (7.3)):

$$P(\vec{p}_1, \vec{k}, \vec{e}_{linear}) = \frac{8\epsilon_1\epsilon_2 u^2\zeta^2\Gamma}{(\epsilon_1^2+\epsilon_2^2)(3+2\Gamma) - 2\epsilon_1^2\epsilon_2^2(1+4u^2\zeta^2\Gamma)}, \tag{4.18}$$

where k is the energy of the photon, $\epsilon_{1,2}$ energies of the incident/scattered electrons, $u = p_1\theta_1$, $\zeta = (1+u^2)^{-1}$, $\theta_1 = \epsilon_1^{-1}$, function $\Gamma = ln(1/\delta) - 2 - f(Z) + \mathfrak{F}(\delta/\zeta)$ should be used to take the screening into account, $\delta = k/(2\epsilon_1\epsilon_2)$. The maximum polarization should appear at a specific angle, m_e/E_e, of the photon emission called the critical angle [48, 54].

The algorithm based on the above theoretical considerations to calculate the polarization as a function of the photon energy was compared to the data which were calculated by the authors of reference [53]. The result is presented for the 50 MeV electrons incident on a lead converter and the polarization is calculated as a function of the photon energy at the angle of emission 0.57 degrees (see Fig. 4.13).

The calculation took into account the Coulomb correction to the Born approximation and the screening of the atomic nucleus. As can be seen from Fig. 4.13, good agreement between the results of [53] and the reproduction was obtained.

The next step was to observe the polarization as a function of the photon energy for our experimental conditions: a 0.25 mm thick aluminum converter and 25 MeV electron beam. The maximum polarization is achieved at the critical angle which is in our case $\theta_c = m_e/E_e \approx 1.2°$. Also it should be noted that the linear polarization decreases with the photon energy. This effect is also shown in Fig. 4.14.

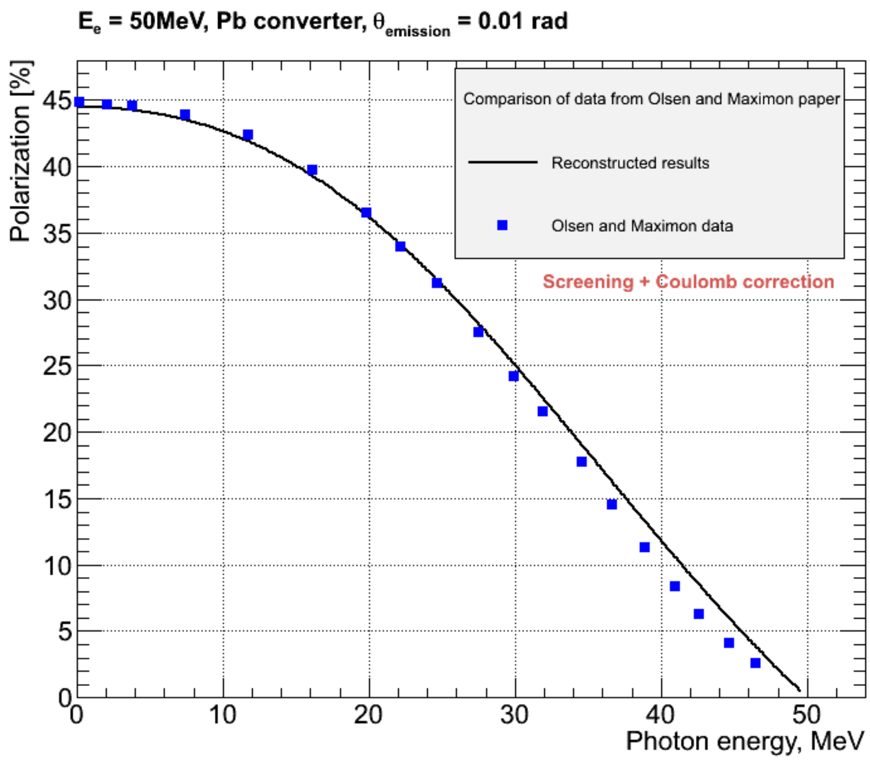

Fig. 4.13. The results of the reproduction of the data [53].

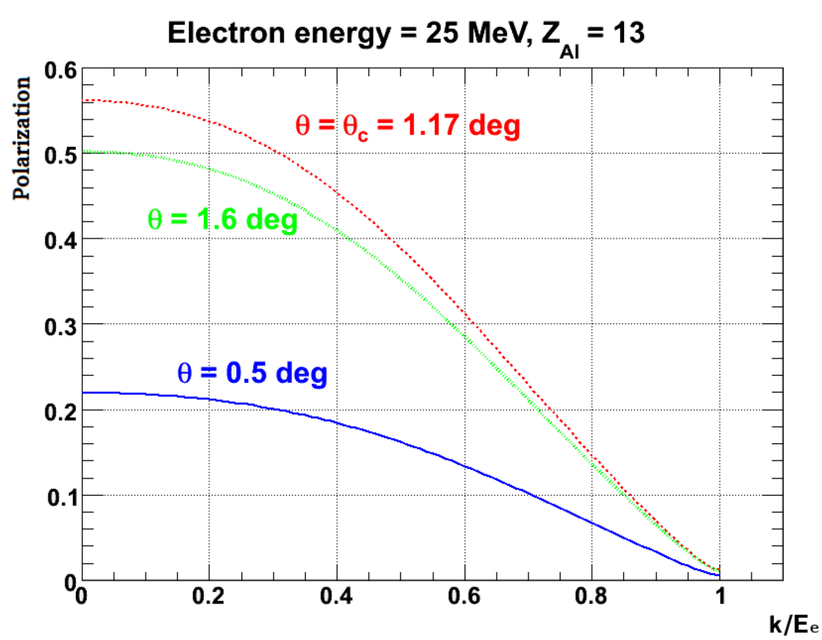

Fig. 4.14. Polarization of photons as a function of k/E_e.

The next step was to observe the polarization as a function of the photon emission angle for our experimental conditions. In order to obtain this dependence we used Eq. (4.18), where the photon energy was fixed and the emission angle varied. The results of a calculation of the polarization *versus* polar emission angle of the photon is shown in Fig. 4.15 for different photon energies.

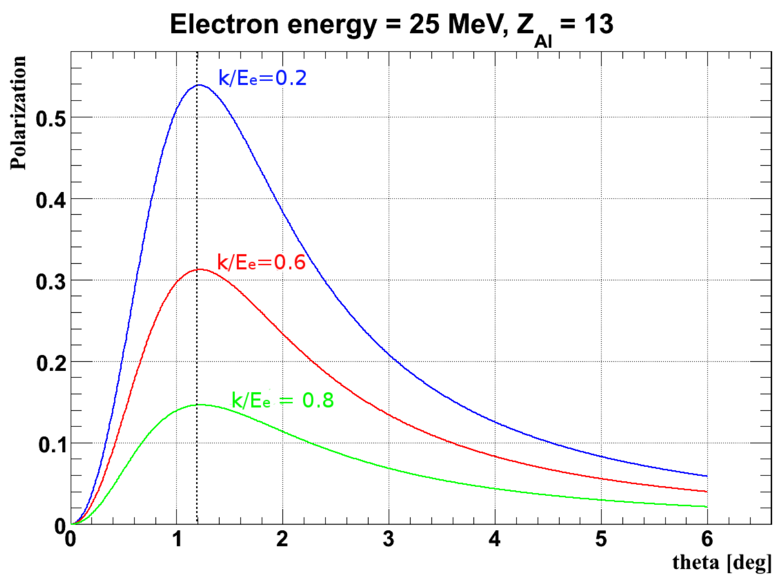

Fig. 4.15. Polarization of photons as a function of polar angle for different k/E_e values.

As can be seen from Fig. 4.15, the critical angle of 1.2 degrees at which the polarization has a maximum was obtained. This is in agreement with [54].

In order to calculate the average polarization over the hole of the downstream collimator positioned in the experimental hall (see Fig. 4.25), it is necessary to take into account the angular distribution of bremsstrahlung photons because the collimator has a finite acceptance. The dependence of the number of photons at a specific angle of emission is presented in Fig. 4.16 and was calculated using:

$$\frac{dN}{d\theta} = \frac{\theta/\theta_c}{(1+(\theta/\theta_c)^2)^2}. \tag{4.19}$$

The angular distribution of bremsstrahlung photons can also be very well approximated by the formula:

$$N(\theta) = \frac{1}{[1+(\frac{\theta}{\theta_c})^2]^2} \tag{4.20}$$

which is "the usual approximation to the angular distribution calculated by Schiff" [48].

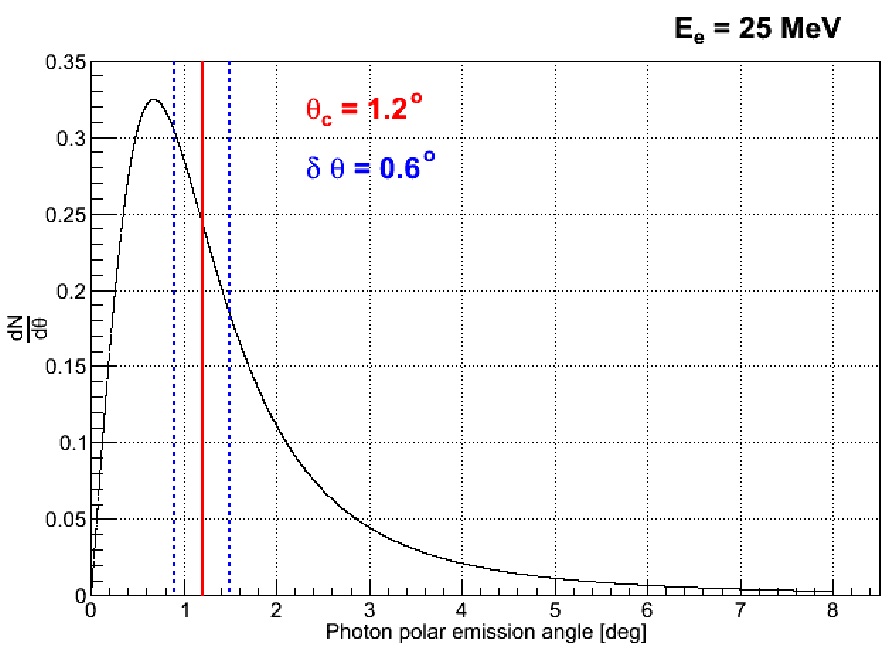

Fig. 4.16. Angular distribution of the bremsstrahlung photons.

It can be seen from Fig. 4.16 that the maximum of the angular distribution is at an angle lower than the angle of maximum polarization.

The next step was to consider the yield of bremsstrahlung photons as a function of the photon energy. The calculation was performed by [19] using reference [55] and is presented in Fig. 4.17 together with a fit function. The fit was done by using the Origin software package. As the procedure did not require a specific function to fit the electron yield, a polynomial was chosen. The degree of the polynomial used for fitting provided a reduced R^2 value of 0.99.

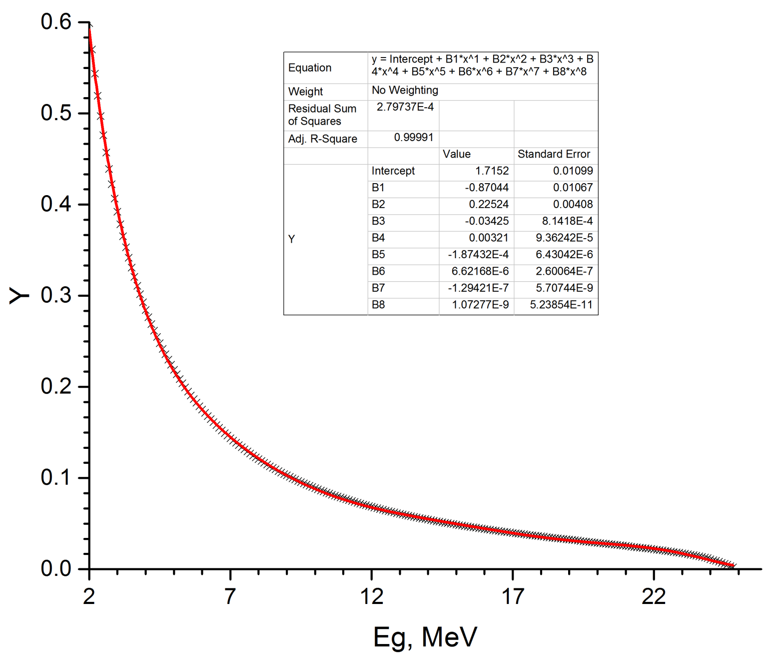

Fig. 4.17. Bremsstrahlung yield for $Z = 13$ and $E_e = 25$ MeV.

Once the shape of the angular distribution of the bremsstrahlung photons and the shape of the photon yield as a function of the photon energy are known together with the polarization dependence on the photon emission angle and the photon energy, it is possible to estimate the polarization distribution over the collimator hole and, finally, to obtain the spectrum of the values of polarization which is going to be on the target in the experimental hall. In our case, the upstream collimator was placed at a distance 280 cm away from the Al bremsstrahlung radiator. The downstream collimator hole had a diameter of around 4 cm which corresponds to the aperture $\theta_c/2 = 0.6°$ with the center of the hole placed at the critical angle $\theta_c \approx 1.2°$. In this case, the polar angle range was $\theta = 1.2° \pm 0.3°$ (see Fig. 4.16).

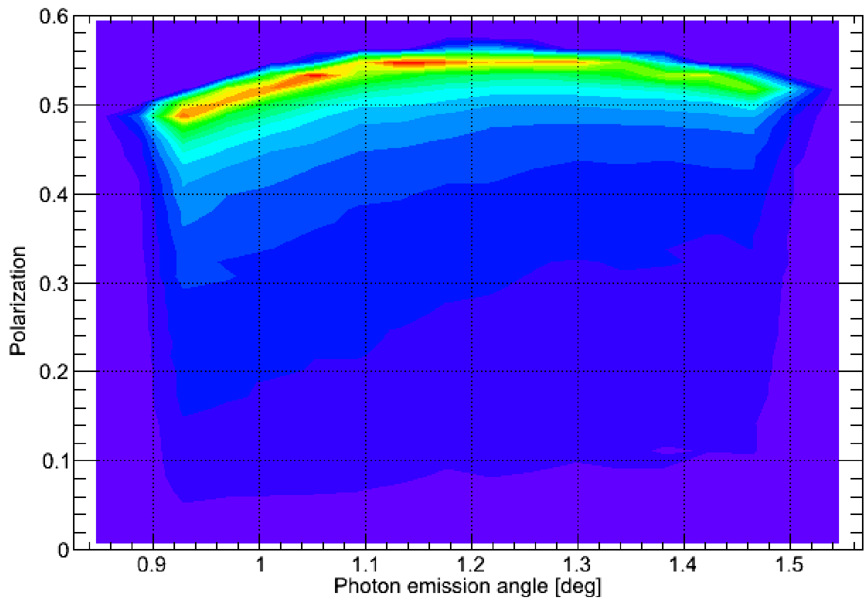

Fig. 4.18. Photon polarization *versus* emission angle after taking into account corrections due to the collimation, bremsstrahlung angular distribution and bremsstrahlung yield.

Using Monte-Carlo techniques, the values of photon emission angles and photon energy values were sampled according to their distributions shown in Figs. 4.16 and 4.17. Additional cuts were applied to the angular distribution because of the collimator presence, *i.e.*, the possible values of the emission angle were limited by the collimator acceptance. Also, a lower energy cut of 2.2 MeV was applied to the photon energy distribution because the photodisintegration reaction of deuterium, which was used to analyze the polarization, has a threshold of 2.2 MeV.

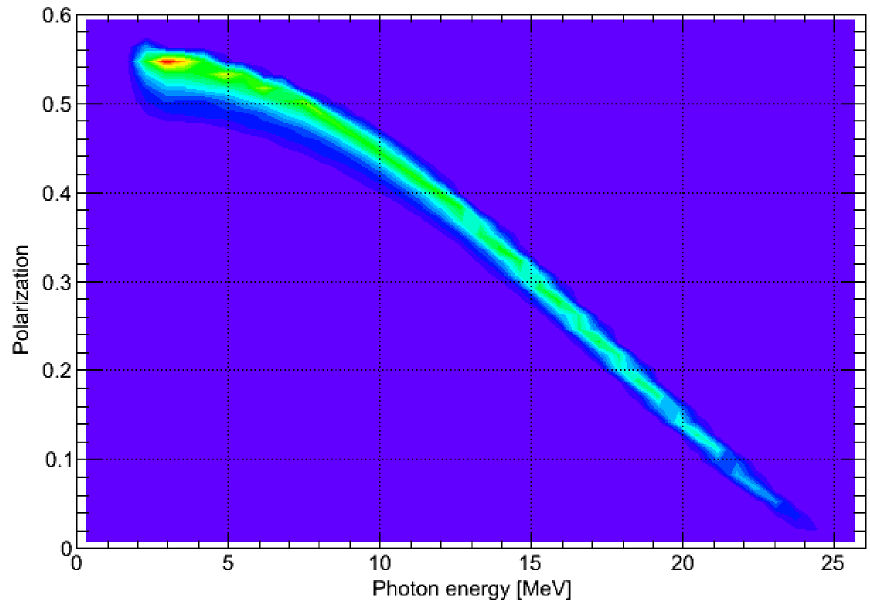

Fig. 4.19. Polarization *versus* photon energy after taking into account corrections due to the collimation, bremsstrahlung angular distribution and bremsstrahlung yield.

By doing the Monte-Carlo procedure, the photons were selected for which the angle of emission and the energy had allowed values. After the energy and the emission angle were obtained, the polarization of the photon was calculated. The reconstructed polarization as a function of the emission angle is shown in Fig. 4.18 and polarization as a function of the photon energy is shown in Fig. 4.19.

Finally, the spectrum of polarization of the incident photons is presented in Fig. 4.20. It can be concluded that the average polarization is around 39%. The experimentally measured neutron asymmetry which is proportional to the photon

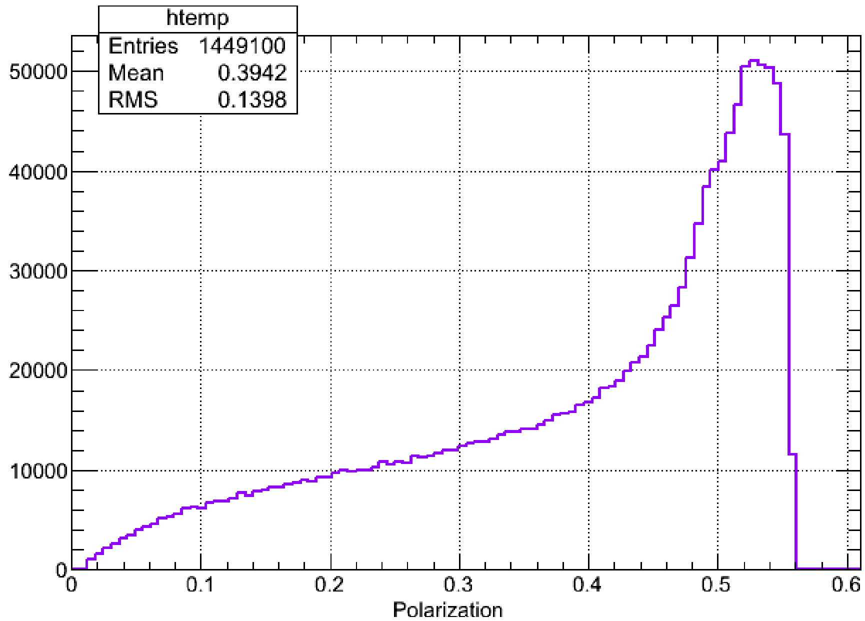

Fig. 4.20. The spectrum of polarization shaped by the acceptance of the collimator, bremsstrahlung photon angular distribution, and by the bremsstrahlung photon energy spectrum. Average polarization is 39%.

beam polarization is shown in Fig. 4.33, and will be discussed in more detail later in this chapter. The energy of the incident electrons was 25 MeV and the material of bremsstrahlung converter was Al ($Z = 13$). The maximum value of the average degree of polarization was found to be around 30%.

Electron Scattering in the Radiator

The production of linearly polarized photons relies on a correlation between the direction of the incident electron and that of the emitted photon. For an electron passing through matter, it is possible to interact with the atoms in the material in many ways. One of the possible interactions of the electron with matter is Rutherford scattering [56, p. 19]. If we assume that the scattering material is very thin, then the probability for the incident electron to scatter multiple times is low. In this case the electron undergoes Coulomb scattering from a single nucleus. The cross section for the electron elastic single scattering from a nucleus is given by the Rutherford scattering formula [56, p. 23]:

$$\frac{d\sigma}{d\theta} = \frac{0.8139 \cdot Z^2}{E^2(\mathrm{MeV})} \frac{\sin(\theta)}{\sin^4(\theta/2)}. \tag{4.21}$$

If the foil is relatively thick, the electron undergoes more than one collision inside the material of the foil. During the propagation inside the foil, the electron is deflected from its initial pass by many small angles. The final deflection angle will be determined by the sum of the individual small angles [56, p. 40] which are not correlated.

Moliere derived the number of electrons $f(\theta, t)$ scattered an angle θ after they passed a thickness t using standard transport equations and the following equation [57]:

$$f(\theta, t) = \int_0^\infty \eta d\eta J_0(\eta\theta) e^{-Nt(\int_0^\infty \sigma(\chi)\chi d\chi(1-J_0(\eta\chi)))}, \tag{4.22}$$

where N is the number of scattering atoms per cubic centimeter, $J_0(\eta\theta)$ is a Bessel function, $\sigma(\chi)\chi\, d\chi$ is the differential scattering cross section in the range of angles $d\chi$. This equation was derived assuming that scattering angles are small and $\sin(\theta) \approx \theta$.

The above results were used to calculate the scattering angle of the electrons after they pass through the material of a certain thickness. The number of electrons scattered in the angular interval $d\theta$ after passing through the thickness t is given by [57]:

$$f(\theta)\theta d\theta = \lambda d\lambda \int_0^\infty ydyJ_0(\lambda y)exp[\frac{1}{4}y^2(-b + ln\frac{1}{4}y^2)]. \tag{4.23}$$

We used Geant4 to determine the thickness of bremsstrahlung converter that is most effective for production of an off-axis polarized photon beam for an energy of the incident electrons 25 MeV. The electrons impinged on an aluminum converter of different thicknesses and the polar emission angle θ was detected for the primary electrons outside the slab. The total number of electrons which hit the converter was 10^6 per given thickness. The value of the resulting electron emission angle θ is the mean value of the total angular distribution of outgoing electrons.

Table 4.1. Electron emission angle for varying Al converter thicknesses.

Thickness of Al, mil	Emission angle, rad
0.1	0.0043 ± 0.0021
0.25	0.0071 ± 0.0032
0.5	0.010 ± 0.005
1.0	0.014 ± 0.007
2.0	0.02 ± 0.01
3.0	0.025 ± 0.011

The average emission angle for primary electrons outside the converter can be found in Table 4.1.

The critical angle for 25 MeV electrons is $\theta_{critical} = m_e/E_e = 0.511/25 = 0.0204$ rad. Hence, for twenty-five MeV electrons, we want to use an aluminum bremsstrahlung converter with thickness less than 2.0 mil (1.0 mil = 25.4 μm) to obtain $\theta_{emission} < \theta_{critical}$.

4.3.2 Experimental setup and development of polarized photons

Experimental setup for the asymmetry measurement of prompt neutrons in the photofission experiment

In order to produce a beam of polarized photons, an electron linear accelerator located at the Idaho Accelerator Center was used. The energy of the electron beam was 25 MeV, the electron pulse was 2 ns wide with a repetition frequency of 180 Hz. For this electron energy, the characteristic angle at which the bremsstrahlung radiation has a maximum polarization value is $m_e c^2/E_e = 1.17°$ (see the calculations in Sec. 4.3.1).

The electron beam was directed toward the bremsstrahlung converter made of a 5 mm$\times$25 mm$\times$25 μm of aluminum strip. The radiator strip was suspended via two thin wires 25 mm apart to prevent the beam from scraping the material and reducing the polarization. A weight attached to the suspending wires was used to stabilize the converter assembly. The radiator could be moved up and down to match the beam position. A schematic representation of the bremsstrahlung converter design is shown in Fig. 4.21. The vacuum pipe where the converter was positioned is hidden for clarity of view.

When the electron beam hit the radiator, the bremsstrahlung radiation was produced. The yield $dN/d\theta$ of bremsstrahlung photons as a function of emission angle θ is presented by Eq. (4.11).

A round evacuated beam pipe was used to deliver bremsstrahlung photons produced in the radiator as close as possible to the upstream collimator to reduce background counting rate due to the interactions of photons with air.

In order to produce polarized photons, the electrons were deflected by 1.17°

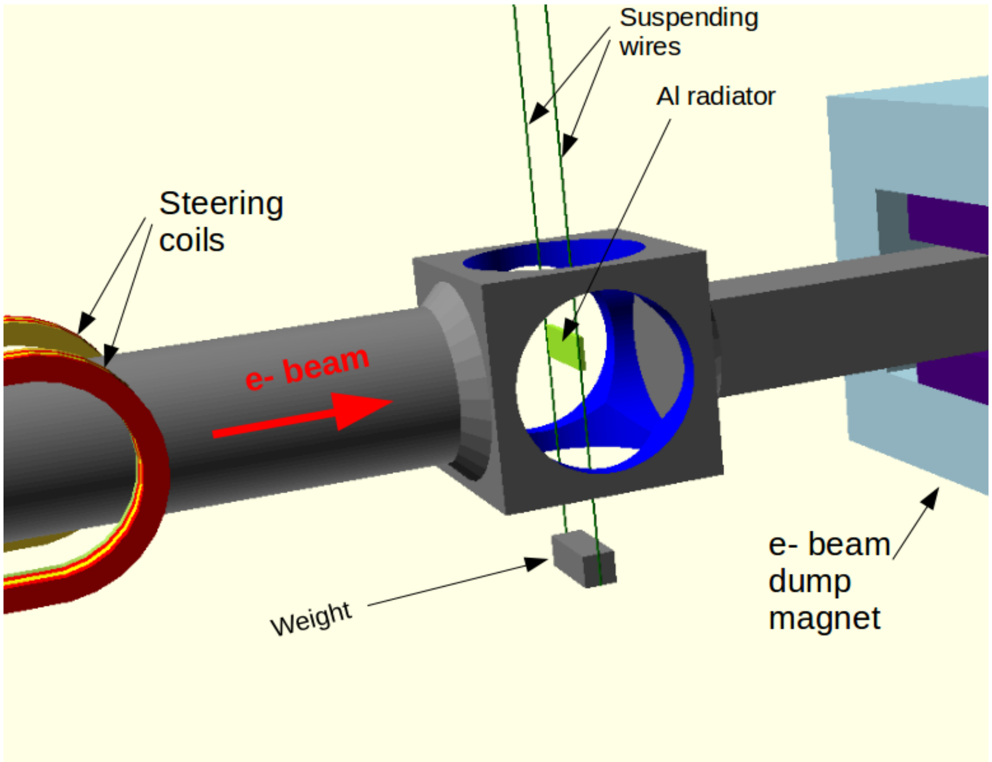

Fig. 4.21. The design of the bremsstrahlung converter for the production of polarized photons.

before hitting the radiator by steering coils placed upstream of the radiator (see Fig. 4.21). The principle of production of polarized photons is presented in Fig. 4.22.

In the experiment, two collimators were used upstream and downstream. The upstream collimator was made of iron and placed 280 cm away from the radiator and had a hole of 2 cm in diameter with the center drilled at a distance 4.13 cm from the beam center. The downstream collimator was also made of iron and placed 463 cm away from the radiator. This collimator had a hole of 4 cm in diameter with the center drilled at a distance 6.8 cm from the beam center. In order to make the bremsstrahlung emission angle equal to the critical emission

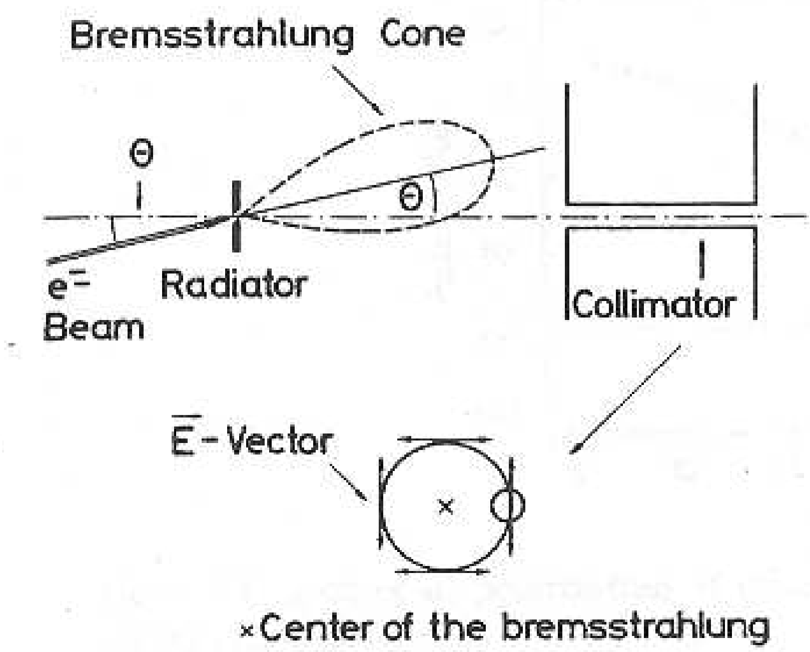

Fig. 4.22. Production of polarized off-axis photon beam. Picture was taken from [54].

angle at which the polarization is highest, it was necessary to bend the beam up/down by 0.84 degrees, which corresponds to the beam spot center moving up/down by 4.13 cm at the position of the upstream collimator. The kicker magnet current was calibrated by placing a phosphorous view screen at the position of the upstream collimator. It was determined that in order to get the maximum photon beam polarization for 25 MeV electrons, the value of the current flowing through the coils should be 90 A, which corresponded to the average on-beam-axis magnetic field 130 gauss. The power supply for the steering coils was placed at the accelerator hall and the current was controlled remotely from the counting room.

After production of the bremsstrahlung radiation, the scattered electrons were swept in the horizontal direction via a permanent magnet placed downstream of the bremsstrahlung radiator. As a dump material, carbon blocks and lead bricks were used.

The polarized photon beam was continuous in energy. In order to cut out the majority of the low-energy photons a one inch aluminium brick was used as a beam hardener. It was placed in front of the upstream collimator. The effect of the beam hardener was that it absorbed low energy photons created in the bremsstrahlung radiator. In order to get the same degree of beam hardening with less thickness of hardener, a material heavier than aluminum such as copper should be chosen.

In order to separate polarized bremsstrahlung photons with a known degree of polarization, two collimators with off-beam axis holes were placed in series downstream from the beam hardener. The position and geometry of the collimators were chosen to provide the highest possible value of the polarization of the photon beam for a given electron energy and the angular size of the aperture was chosen to be $0.5 m_e c^2/E_e$. The stability of the photon flux was monitored by a photon flux monitor which is discussed in Sec. 3.3.

A heavy water D_2O target in a plastic cylindrical container was used as a target. The dimensions of the D_2O target were the following: $1.25''$ in diameter and $6.7''$ in height. Deuteron photodisintegration allowed us to measure neutron ϕ-angular asymmetry and define the degree of polarization of the photon beam. For background measurements we used exactly the same plastic container filled with H_2O.

In the experiment we used nine detectors. The scintillating material, BC-420, was optically attached to a PMT without use of a light guide. For details on the neutron detector design see Sec. 3.2. The data acquisition system used in this part of the experiment to read-out the signals from the detector and to process and store the experimental data is described in Sec. 3.1. The detectors were centered on the target as shown in Fig. 4.23.

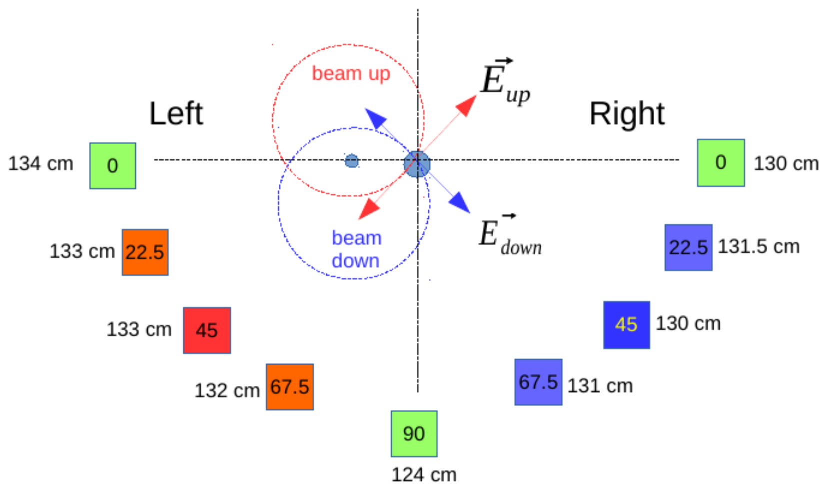

Fig. 4.23. Placement of the neutron detectors with respect to the beam line and collimator.

The azimuthal angular distribution of the prompt neutrons was detected via these detectors placed at different ϕ angles and at the angle $\theta = 90°$ with respect to the beam direction. A general view of the experimental setup placed in the accelerator hall is presented in Fig. 4.24, and a general view of the experimental setup placed in the experimental hall is presented in Fig. 4.25.

Before investigation of the neutron angular distribution from the main ^{238}U experimental target, the polarization of the photon beam was established by using the well known reaction kinematics of deuteron photodisintegration. The data were collected for both polarities of the kicking magnet (beam up/beam

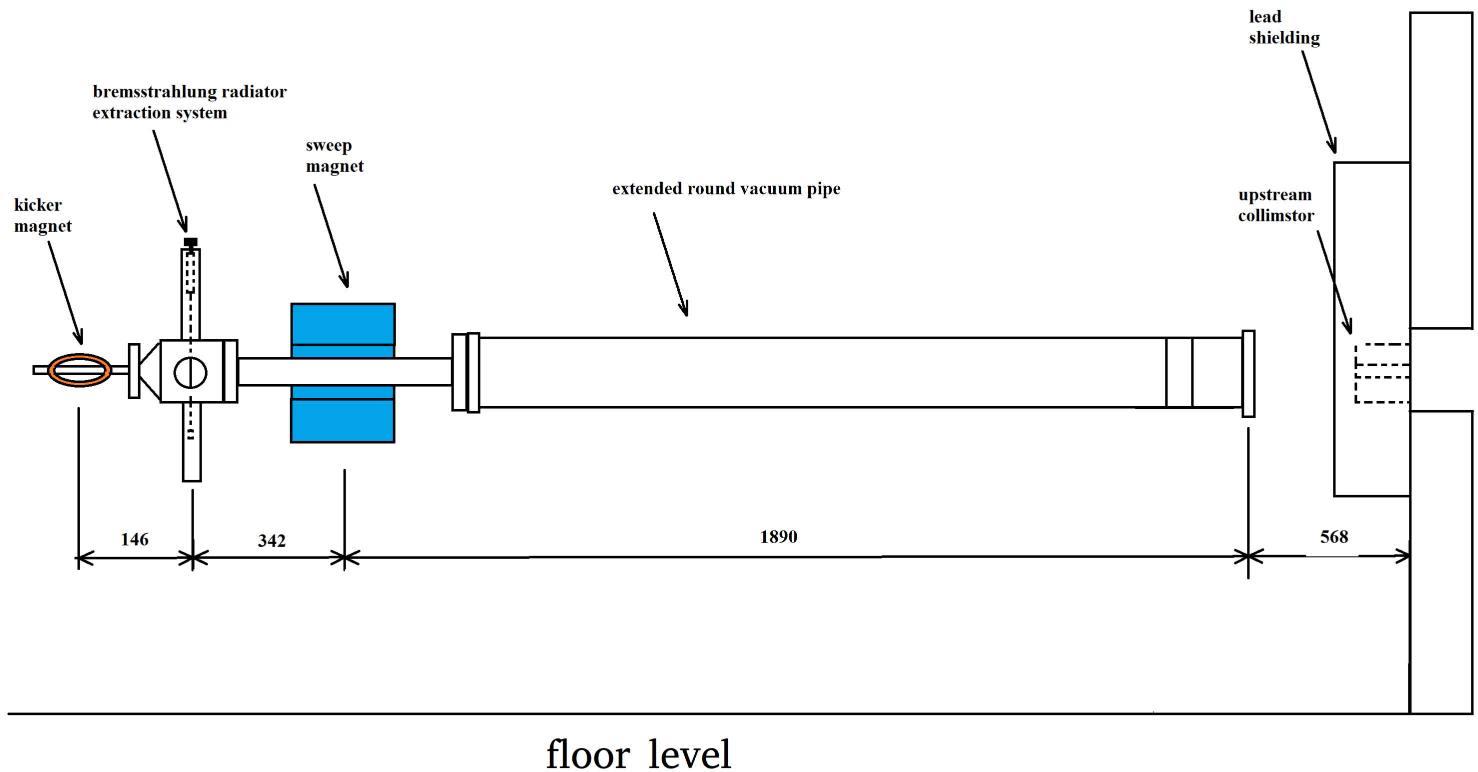

Fig. 4.24. Experimental setup in the accelerator hall. Side view.

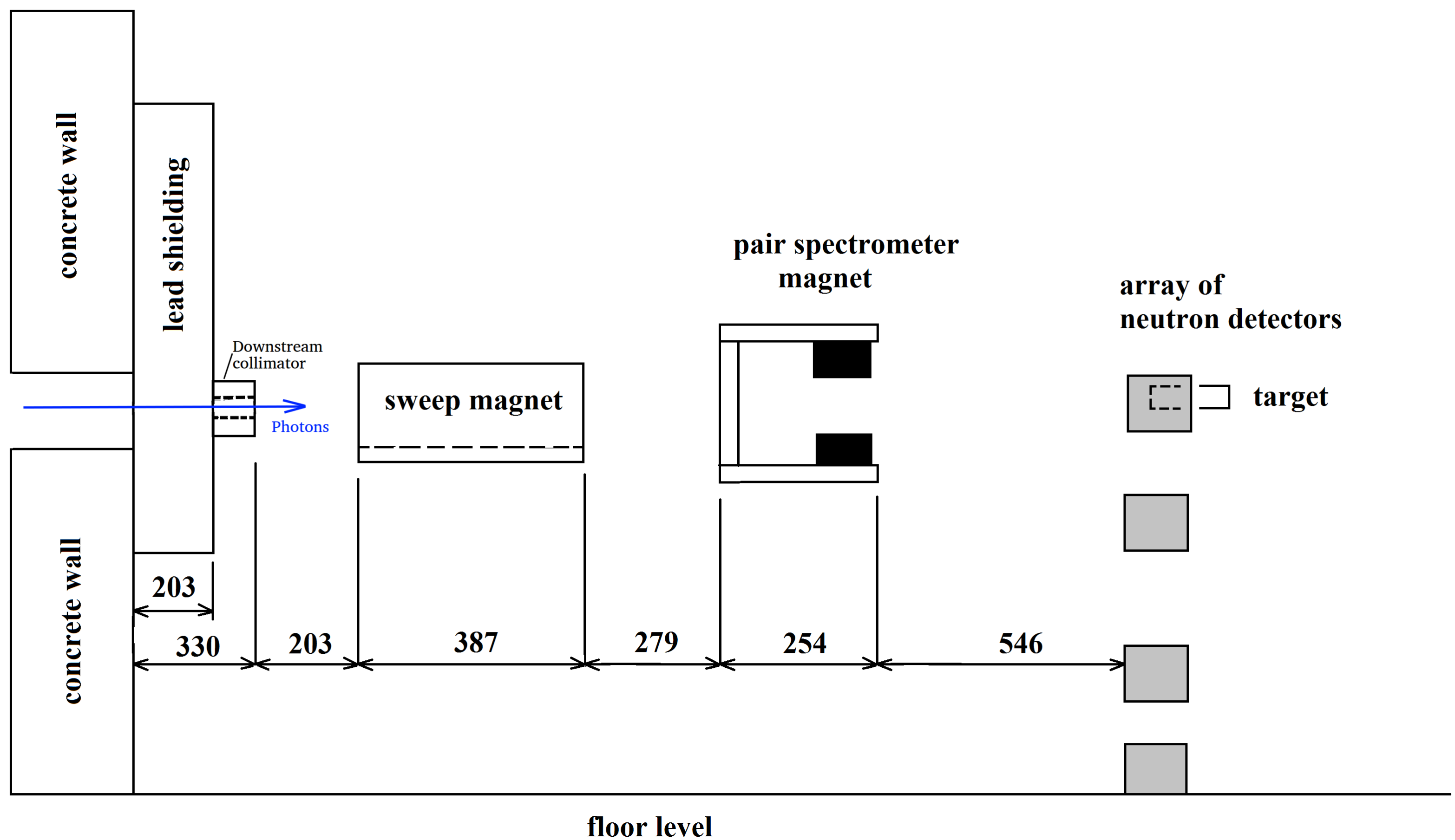

Fig. 4.25. Experimental setup in the experimental hall. Side view.

down). The ^{238}U experimental target had a cylindrical shape with the following dimensions: 1.2″ in diameter and 4.7″ in height. It was placed at the position of the D_2O target after the polarization of the photon beam was established. The upstream side of the target was moved three centimetres upstream with respect to the center of the active volume of neutron detectors. We investigated the neutron angular asymmetry created by linearly polarized photons during irradiation of a ^{238}U fissionable target. The results are discussed later in this paper.

4.4 Polarimeter

4.4.1 Photodisintegration reaction as a polarimeter

In this part of the thesis, the approach used to obtain and analyse the angular distribution of neutrons emitted by fission fragments will be described. An important part of the project is the production of a linearly polarized photon beam and the ability to determine the polarization produced.

In order to be able to measure the degree of the photon beam polarization, the process of photodisintegration of deuterium was used as an analysing reaction. There are no bound excited states for the deuteron and the only possible state is the state where neutron and proton are free. The incident polarized photons may be considered as a polarized electromagnetic waves. The direction of the electric force acting on the proton is along the direction of the polarization vector [58] of the polarized electromagnetic wave incident over the deuterium target. The asymmetry in the neutron angular distribution is caused by a combination of different physical effects of interaction of the incident photons with the deuteron such as [59] electric interaction, magnetic convection interaction, magnetic spin interaction, and magnetic exchange interaction (due to the charge exchange-nature of nuclear forces). Taking into account these effects, it is possible to calculate the cross section of photodisintegration as a function of the angle between the incident photon and outgoing neutron. The cross section for photodisintegration for an s-state nucleus with unpolarized photons can be calculated as:

$$\frac{d\sigma_0}{d\Omega}(\theta, E_\gamma) = A_\gamma + B_\gamma \sin^2(\theta) + C_\gamma \sin^2(\theta)\cos(\theta) + D_\gamma \sin^2(\theta)\cos^2(\theta). \quad (4.24)$$

The coefficients A_γ, B_γ, C_γ, and D_γ can be found in [60].

The differential cross section for deuterium photodisintegration with linearly polarized photons can be calculated according to Ref. [61] as a function of the differential cross section for unpolarized photons and a part that depends on the photon polarization:

$$\frac{d\sigma}{d\Omega}(\theta, \phi, E_\gamma) = \frac{d\sigma_0}{d\Omega}(\theta, E_\gamma)[1 + P_\gamma \Sigma(\theta, E_\gamma)\cos(2\phi)], \quad (4.25)$$

where P_γ is the photon polarization and $\Sigma(\theta, E_\gamma)$ is the asymmetry of the photodisintegration reaction. The degree of polarization of the photon beam is given by $P_\gamma = \frac{N_\perp - N_\parallel}{N_\perp + N_\parallel}$, where $N_\parallel$ is the number of photons whose electric field vector is parallel to the photon emission plane and $N_\perp$ is the number of photons whose electric field vector is perpendicular to the photon emission plane. The asymmetry determined experimentally can be expressed as:

$$A = \frac{N'_n - N_n}{N'_n + N_n} \sim \Sigma(\theta, E_\gamma)P_\gamma, \quad (4.26)$$

where N'_n and N_n are the number of neutrons detected by the experimental setup for different directions of deflections of the electron beam. The asymmetry function can be considered to be $\Sigma(\theta, E_\gamma) \sim 1$ for $E_\gamma \sim 25$ MeV and the experimentally measured neutron asymmetry is proportional to the photon beam polarization P_γ.

4.4.2 Deuterium photodisintegration kinematics

Under the interaction of the photon with the deuteron, the deuteron splits into a proton and a neutron, if the energy of the photon is higher than 2.2 MeV. Also there is a chance for quasi-free Compton scattering $\gamma d \to \gamma' np$ of the incident photon by neutron or proton which are bound inside the deuteron [62]. This reaction can be used to determine the electric polarizability of neutron. The Feynman diagrams for the Compton scattering are shown in Fig. 4.26. In order to observe the quasi-free Compton scattering, a higher energy of the incident photons is needed (hundreds of MeV) than in the case of the photodisintegration reaction ($\sim$ 2.2 MeV and higher) and will not be discussed further in this paper.

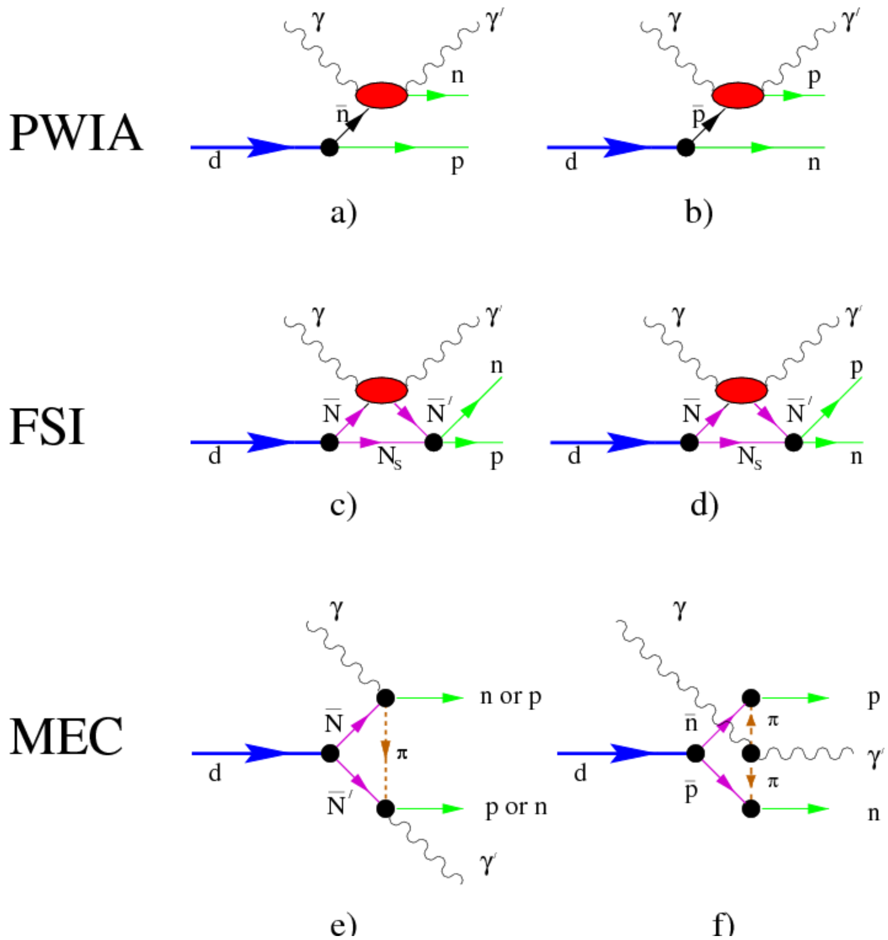

Fig. 4.26. The quasi-free Compton scattering process on the deuteron pictured using Feynman diagrams. a) and b) are the Compton scattering amplitudes calculated in plane wave impulse approximation (PWIA), c) and d) Feynman diagrams obtained by taking into account final-state interactions (FSI) of the nucleons, e) and f) Feynman diagrams describing meson exchange corrections (MEC). The figure was taken from [63].

The kinematics of deuteron photodisintegration is shown below in Fig. 4.27.

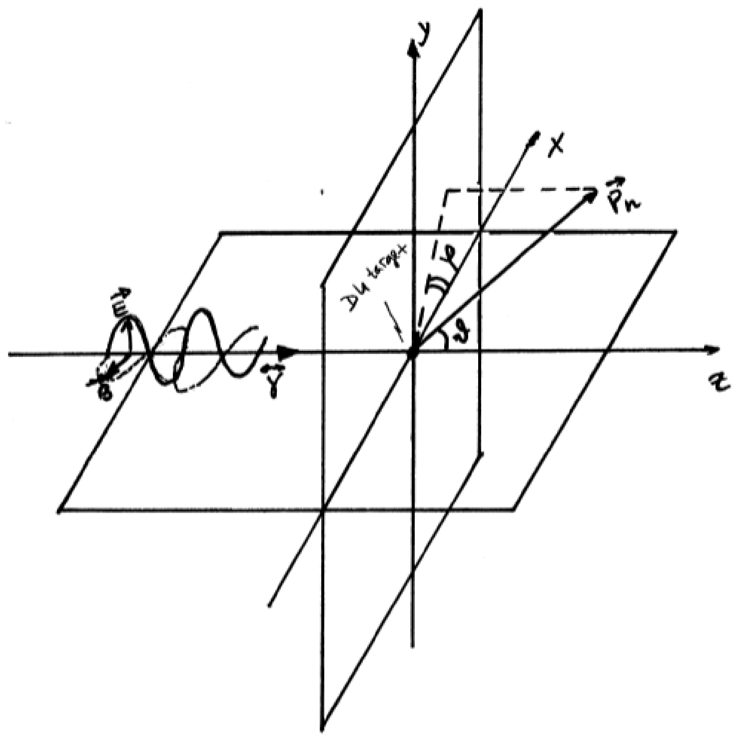

Fig. 4.27. Sketch of the deuteron photodisintegration kinematics.

The total center-of-mass (CM) energy in Lorentz invariant form can be written as:

$$W_{cm} = [m_\gamma^2 + m_d^2 + 2E_\gamma E_d(1 - \beta_\gamma \beta_d \cos\theta_{d\gamma})]. \tag{4.27}$$

The total CMS energy in the laborotory frame can be written as:

$$W_{cm} = [m_d^2 + 2E_\gamma^{lab} m_d]^{1/2}. \tag{4.28}$$

The total neutron energy in the CMS can be expressed in terms of Lorentz invariant Mandelstam variables as:

$$E_n^{cm} = \frac{s + m_n^2 - m_p^2}{2\sqrt{s}}. \tag{4.29}$$

Calculating the value of s, it can be obtained that $s = W_{cm}^2$. Hence, the total neutron energy in the CMS can be expressed as:

$$E_n^{cm} = \frac{W_{cm}^2 + m_n^2 - m_p^2}{2W_{cm}}. \tag{4.30}$$

The neutron kinetic energy in the CMS can be found from the expression for the total neutron energy in the CMS as:

$$T_n^{cm} = \frac{(W_{cm} - m_n)^2 - m_p^2}{2W_{cm}}. \tag{4.31}$$

Boosting the neutron kinetic energy into the laboratory frame enables one to find the relation between the neutron emission angle and its kinetic energy for a given incident photon energy.

The Lorentz transformation of the total neutron energy in CMS into the laboratory frame is:

$$E_n^{lab} = \gamma_{cm}(E_n^{cm} + v_{cm} p_{nz}^{cm}), \tag{4.32}$$

where $p_{nz}^{cm} = \sqrt{(E_n^{cm})^2 - m_n^2} \cos\theta_{cm}$. The dependence of the neutron kinetic energy on the neutron emission angle with respect to the direction of the incident photon in the laboratory frame is presented in Fig. 4.28.

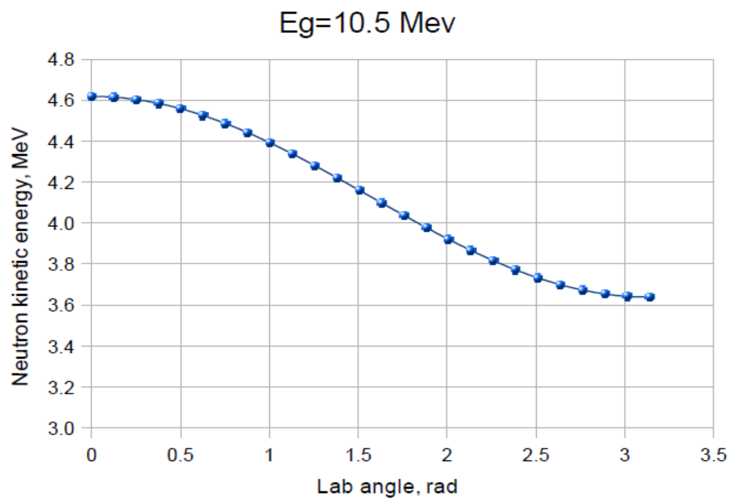

Fig. 4.28. Dependence of the neutron kinetic energy on neutron emission angle in the laboratory frame. The energy of the incident photon is $E_\gamma = 10.5$ MeV.

The dependence of the neutron kinetic energy on the incident photon energy in the laboratory frame is presented in Fig. 4.29.

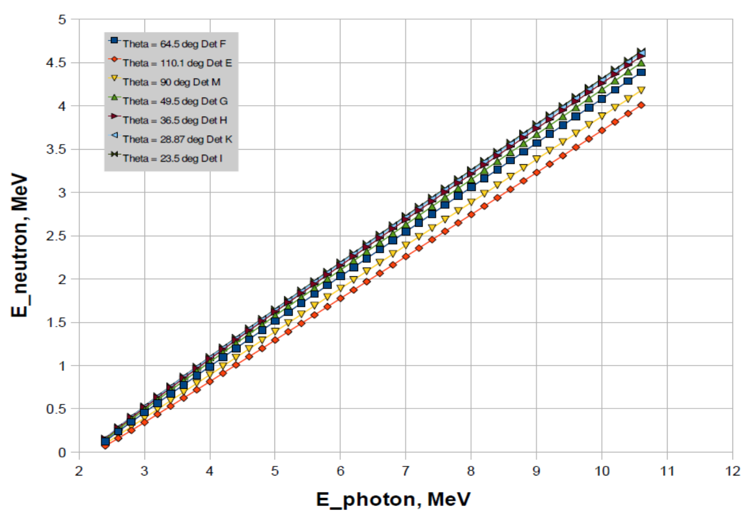

Fig. 4.29. Neutron kinetic energy *versus* photon energy in the laboratory frame for different emission angles θ.

4.5 Results and discussion

4.5.1 Studies of neutron energy uncertainties using polarized γ -beam

As mentioned above, we carried out an experiment on the measurement of the neutron emission angular asymmetry due to photodisintegration of deuterium and the angular asymmetry of prompt neutrons created in the process of ^{238}U photofission using a beam of a polarized photons.

During this experiment, we measured time-of-flight spectra of neutrons created in the deuterium photodisintegration reaction, photofission of depleted uranium and background neutrons. The time separation of the gamma flash peak and the neutron emission region in the time-of-flight spectra was observed. Data on the uncertainties in the neutron time-of-flight and neutron flight path in the case of photofission of the DU target are presented in Table 4.2 together with the calculated uncertainties on the neutron energy.

Table 4.2. Neutron energy uncertainties obtained in the photofission reaction on ^{238}U.

Detector	$\sigma \pm \delta\sigma$, ns	t^{RMS}, ns	l^{RMS}, cm	δE_9, %	δE_1, %
0° left	1.75 ± 0.01	1.9	0.75	11	4
22.5° left	1.50 ± 0.02	1.8	0.75	10	4
45° left	1.66 ± 0.02	1.9	0.75	11	4
67.5° left	1.36 ± 0.02	1.5	0.75	9	3
90°	1.72 ± 0.01	2.1	0.75	11	4
67.5° right	1.33 ± 0.02	1.6	0.75	9	3
45° right	1.59 ± 0.04	1.7	0.75	10	4
22.5° right	1.61 ± 0.03	1.9	0.75	10	4
0° right	2.44 ± 0.02	2.6	0.75	16	6

Data on the uncertainties in the neutron time-of-flight and neutron flight path in the case of photodisintegration of deuterium (D_2O target) are presented in Table 4.3 together with the calculated uncertainties on the neutron energy.

Table 4.3. Neutron energy uncertainties obtained in the deuterium photodisintegration reaction.

Detector	$\sigma \pm \delta\sigma$, ns	t^{RMS}, ns	l^{RMS}, cm	δE_9, %	δE_1, %
0° left	2.81 ± 0.07	3.0	0.75	18	6
22.5° left	2.56 ± 0.27	3.1	0.75	17	6
45° left	1.82 ± 0.15	2.6	0.75	12	4
67.5° left	1.55 ± 0.16	3.7	0.75	10	4
90°	2.21 ± 0.12	2.8	0.75	14	5
67.5° right	1.82 ± 0.26	2.5	0.75	12	4
45° right	3.23 ± 0.37	3.4	0.75	20	7
22.5° right	2.63 ± 0.15	3.0	0.75	17	6
0° right	1.74 ± 0.04	2.3	0.75	11	4

As a neutron time-of-flight uncertainty we used the value of sigma obtained from the Gaussian fit of the photon flash in the neutron time-of-flight spectrum. The value of sigma and its uncertainty are presented in the second column of the tables. The RMS value of the time distribution obtained for the whole photon region is presented in the third column. This value reflects the fact that the photon flash was well localized and corresponded to the declared electron pulse width of 2 ns. The fourth column represents the uncertainties on the neutron flight path. These values were obtained from a simulation using Geant4. The last two columns show the neutron energy uncertainties which were calculated using Eq. (2.12). The fifth column shows the uncertainty on the neutron energy 9 MeV. It gives an estimate of the highest expected uncertainty in the neutron energy spectrum since not many neutrons with energy above 9 MeV were detected (see Figs. 4.30, 4.31, 4.35, and 4.36). The last column gives the energy uncertainty on a neutron of energy 1 MeV. The neutrons with energy 1 MeV had the highest yield.

4.5.2 Data on the photon beam polarization

The polarization of the photon beam produced was measured with the help of the photodisintegration of deuterium reaction and compared with the one obtained with the regular H_2O.

Fig. 4.30 shows the energy spectrum of neutrons created during the H_2O target irradiation with the polarized photon beam. The unpolarized electron beam was bent down by directing DC current, flowing in the coils composing the kicker magnet which was placed upstream of the bremsstrahlung radiator, in a direction which produced a magnetic field deflecting the electron beam down with respect to the undeflected electron beam direction. In this configuration, bremsstrahlung photons produced in the converter formed a cone with the polarization vector tangential to the circumference of the cone section and the beam collimating system passed only that part of the photon cone which had the polarization vector aligned $\sim$45 degrees with respect to the horizontal plane. In this orientation, a neutron detector placed at an angle of 45 degrees with respect to the beam line should get more photodisintegration neutrons than the other detectors. The energy spectrum of neutrons created during the D_2O target irradiation is shown in Fig. 4.31. The electron beam was bent down in the same way and with the same effect on the direction of the polarization vector as explained above for the case with the H_2O target.

The resulting polarization asymmetry obtained with the H_2O target is plotted in Fig. 4.32. As expected, the asymmetry is zero.

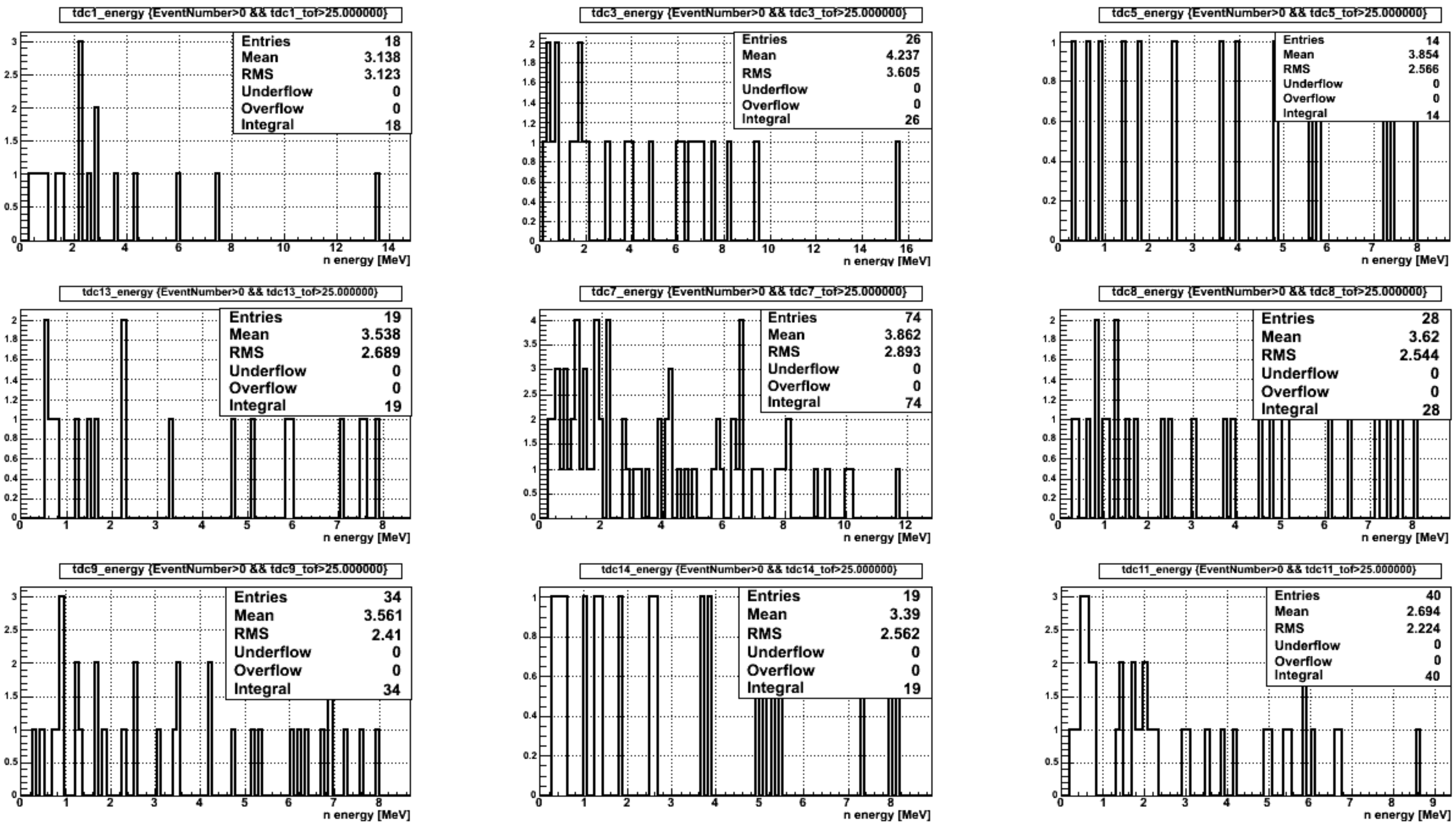

Fig. 4.30. Energy spectra of neutrons from H_2O target. Polarized photon beam is "down".

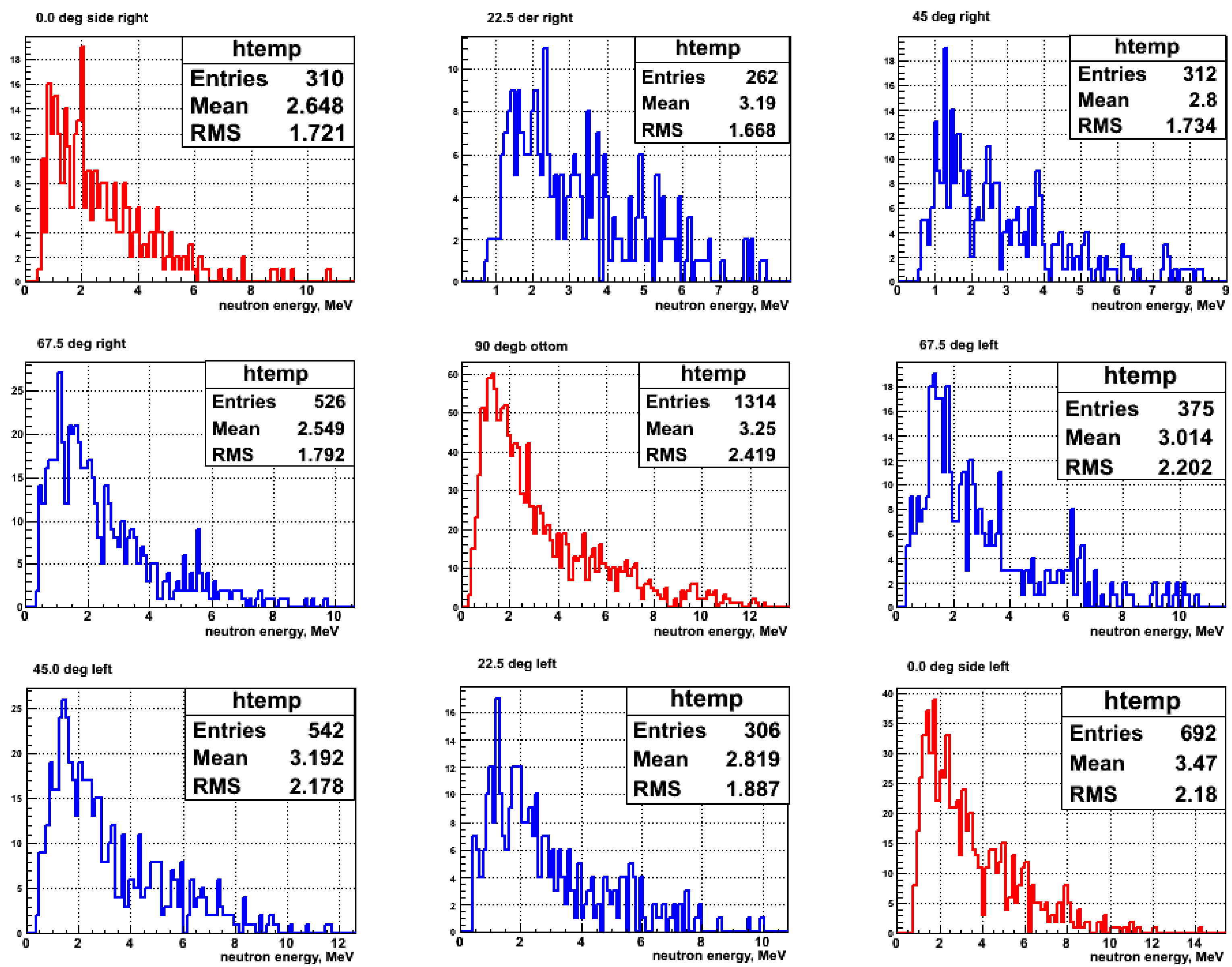

Fig. 4.31. Energy spectra of neutrons from D_2O target. Polarized photon beam is "down".

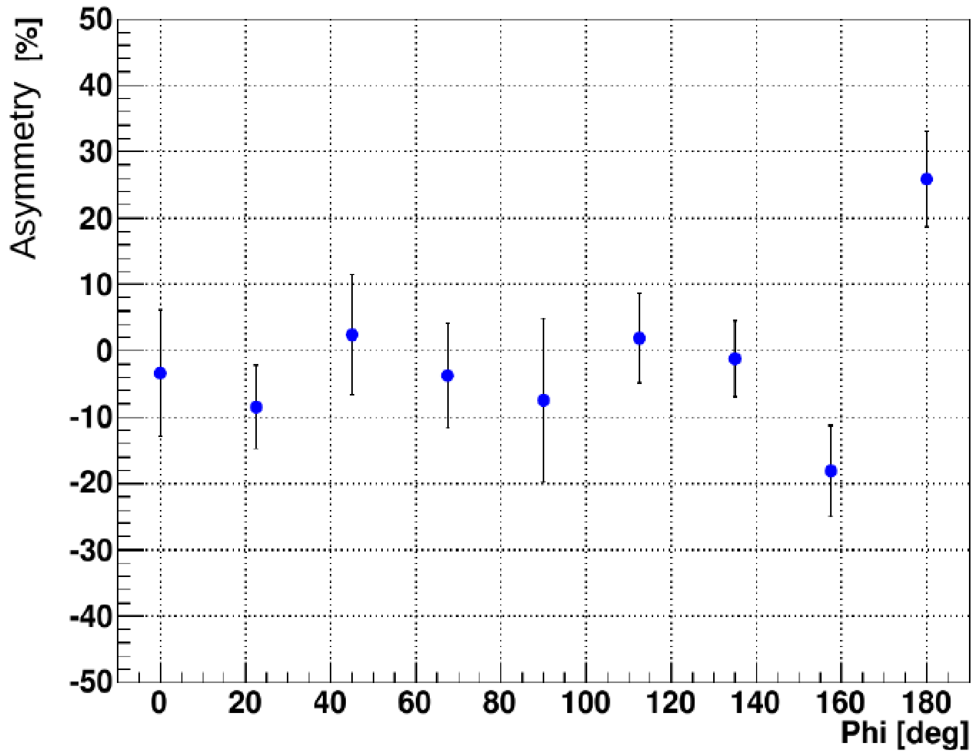

Fig. 4.32. Asymmetry of the neutron angular distribution obtained with H_2O target and polarized photon beam.

In a similar fashion, the photon beam polarization defined with the D_2O target is plotted in Fig. 4.33, where it can be seen that the peak linear polarization of the photon beam is measured to be about 25%.

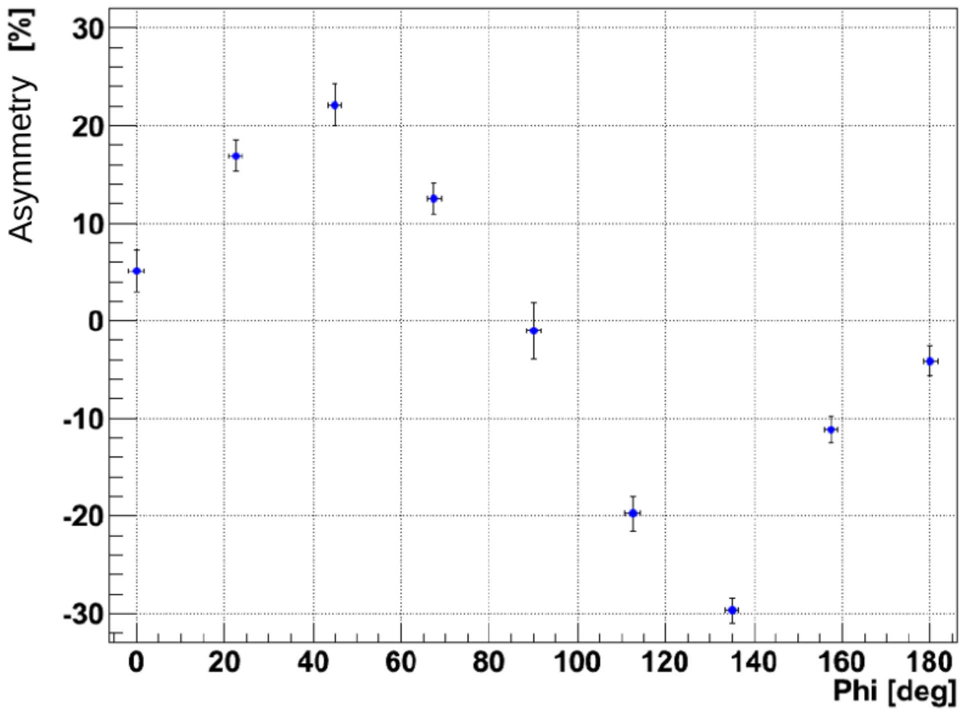

Fig. 4.33. Asymmetry of the neutron angular distribution obtained with D_2O target and polarized photon beam.

The data on the photon beam polarization presented in this section demonstrates the idea that the reaction of the photodisintegration of deuterium can be successfully applied to the photon beam polarization analysis. From the dependence of the neutron asymmetry as a function of azimuthal angle obtained with the D_2O target it can be concluded that the neutron yield depended on the direction of the electron beam bending and, hence, on the direction of the photon polarization vector. The neutron asymmetry changed its sign depending on the azimuthal angle because the difference of the neutron yields [see Eq. (4.26)] detected by a specific neutron detector placed at a specific azimuthal angle also changed sign. As an example, the neutron detector placed at $\phi = 45°$ on the left with respect to the beam (see Fig. 4.23) detected more neutrons for the configuration when the electron beam was bent upward than when it is bent downward. The difference $N^{up} - N^{down}$ for the detector under consideration, applying appropriate normalization, had a positive sign. The same difference for the neutron detector placed at $\phi = 45°$ on the right with respect to the beam had a negative sign.

4.5.3 Normalization procedure and neutron asymmetry calculation

The normalization procedure of the experimental data obtained with D_2O and depleted uranium (DU) targets was performed in order to take into account the possible instabilities of the photon beam flux. If the photon flux was changing during the run, then the neutron count rate would be changing correspondingly. This effect could produce false neutron asymmetries leading to an incorrect determination of the photon beam polarization and angular asymmetries of the prompt neutrons produced in DU photofission. To eliminate this effect, during the data analysis we calculated the sum of the neutron counts recorded by the three neutron detectors placed 0 degree left N_{0l}, 90 degrees bottom N_{90}, and 0 degree right N_{0r} with respect to the photon beam (see Fig. 4.34).

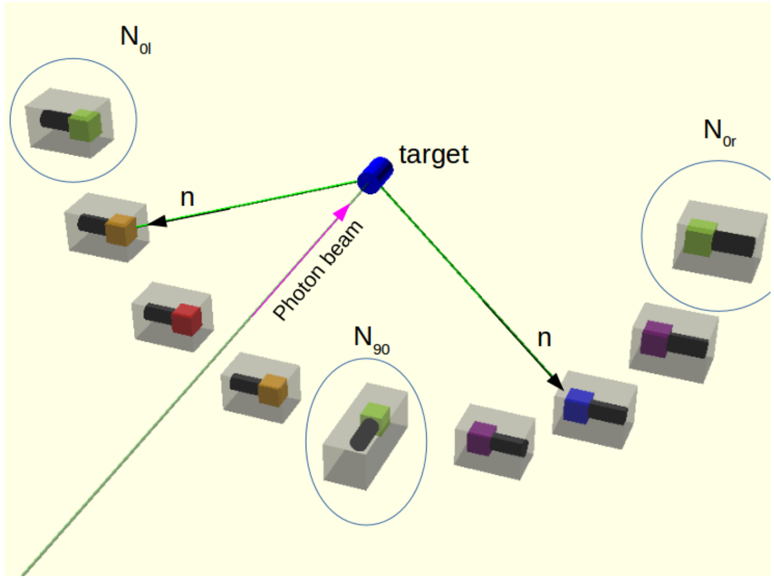

Fig. 4.34. Sketch of the relative detector placement. Neutron detectors circled were used for the normalization.

These three detectors were insensitive to the photon polarization direction because the photon polarization vector was aligned 45 degrees with respect to the vertical direction such that the number of neutrons detected would be the same. However, they were sensitive to the relative photon flux variations, if they occurred during the run. Using the sum of the neutron counts from the three neutron detectors as a normalization factor, the number of neutrons detected by a neutron detector sensitive to the polarization direction N^i corrected to the possible photon flux variations can be found as:

$$N^i_{norm} = \frac{N^i}{N_{0l} + N_{90} + N_{0r}}. \tag{4.33}$$

Also, the errors on the normalized number of neutron counts were calculated in the following way. The values of the neutrons produced in deuterium photodisintegration reaction or photofission reaction of the DU target and their statistical uncertainties can be represented as:

$$N^i \pm \delta N^i = N^i \pm \sqrt{N^i}, \tag{4.34}$$

and

$$N_{norm} \pm \delta N_{norm} = (N_{0l} + N_{90} + N_{0r}) \pm \sqrt{N_{0l} + N_{90} + N_{0r}}. \tag{4.35}$$

Hence the error on the ratio of these two numbers which is normalized to take into account the possible photon flux instabilities can be calculated for both orientations of the electron beam (up or down) as:

$$\delta N^i_{norm} = \frac{N^i}{N_{0l} + N_{90} + N_{0r}} \cdot \sqrt{\frac{1}{N^i} + \frac{1}{N_{0l} + N_{90} + N_{0r}}}. \tag{4.36}$$

Finally, the asymmetry of the neutron emission was calculated as a ratio of neutron number detected by a specific detector for two positions of the electron beam, up and down:

$$A^i = \frac{N^i_{norm\ Up} \pm \delta N^i_{norm\ Up}}{N^i_{norm\ Down} \pm \delta N^i_{norm\ Down}}. \tag{4.37}$$

The background cancels when the asymmetry of the neutron emission is calculated since for both beam orientations the background should have comparable rates.

4.5.4 Results and discussion of the data

Several approaches were followed to extract the information on the prompt neutron angular distribution created in the process of photofission with linearly polarized photons. First, the time-of-flight spectra of neutrons created in the photofission reaction of DU were analyzed and the cumulative energy spectra obtained with each detector in each run were extracted for both orientations of the electron beam and the bremsstrahlung converter strip (up or down). The energy spectra of prompt neutrons from the DU target for the electron beam/bremsstrahlung converter in "down" configuration is shown in Fig. 4.35. It can be seen that the most probable value for the energy of prompt neutrons is about 1 MeV. The effect of the analogue signal discrimination can be observed for the low energy prompt neutrons. The level of the constant fraction discriminator was set to 0 mV in all channels which corresponded to $\sim$10 mV minimum threshold. Similar information on the prompt neutron energy was obtained in the case of electron beam/bremsstrahlung converter in "up" configuration presented in Fig. 4.36. Using the ratios of the integral number of neutrons detected by each neutron detector placed at a specific angle with respect to the beam line obtained for different electron beam configurations and applying cuts on the separate regions of the neutron energy spectra, it was possible to investigate the dependence of the angular asymmetries of the prompt neutron emission as a function of the neutron energy. This is discussed in the next section.

Running asymmetry

A running asymmetry was calculated by binning the neutron energy spectra starting with the higher energy part of the spectrum and going to lower energies in 1 MeV increments, normalizing neutron counts using the technique described in the previous section, and taking a ratio for the case of two electron beam orientations. As can be seen in Figs. 4.35 and 4.36, the number of neutrons with energies in the range from 8 MeV to 7 MeV is relatively small. This makes the statistical error bars on Fig. 4.37 large for the first bin. We expected to see the

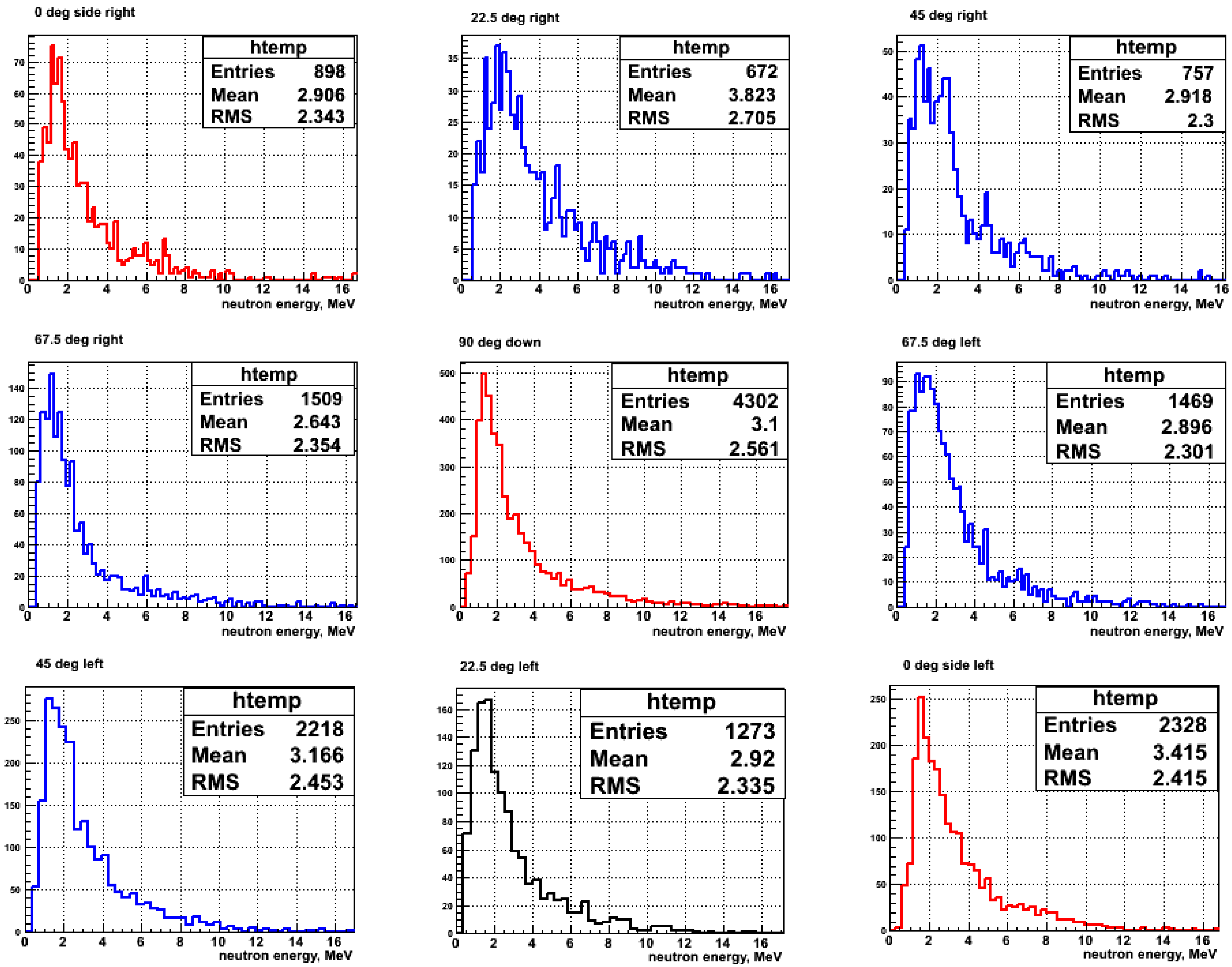

Fig. 4.35. Energy spectra of neutrons from the DU target. Polarized photon beam is ”down” configuration.

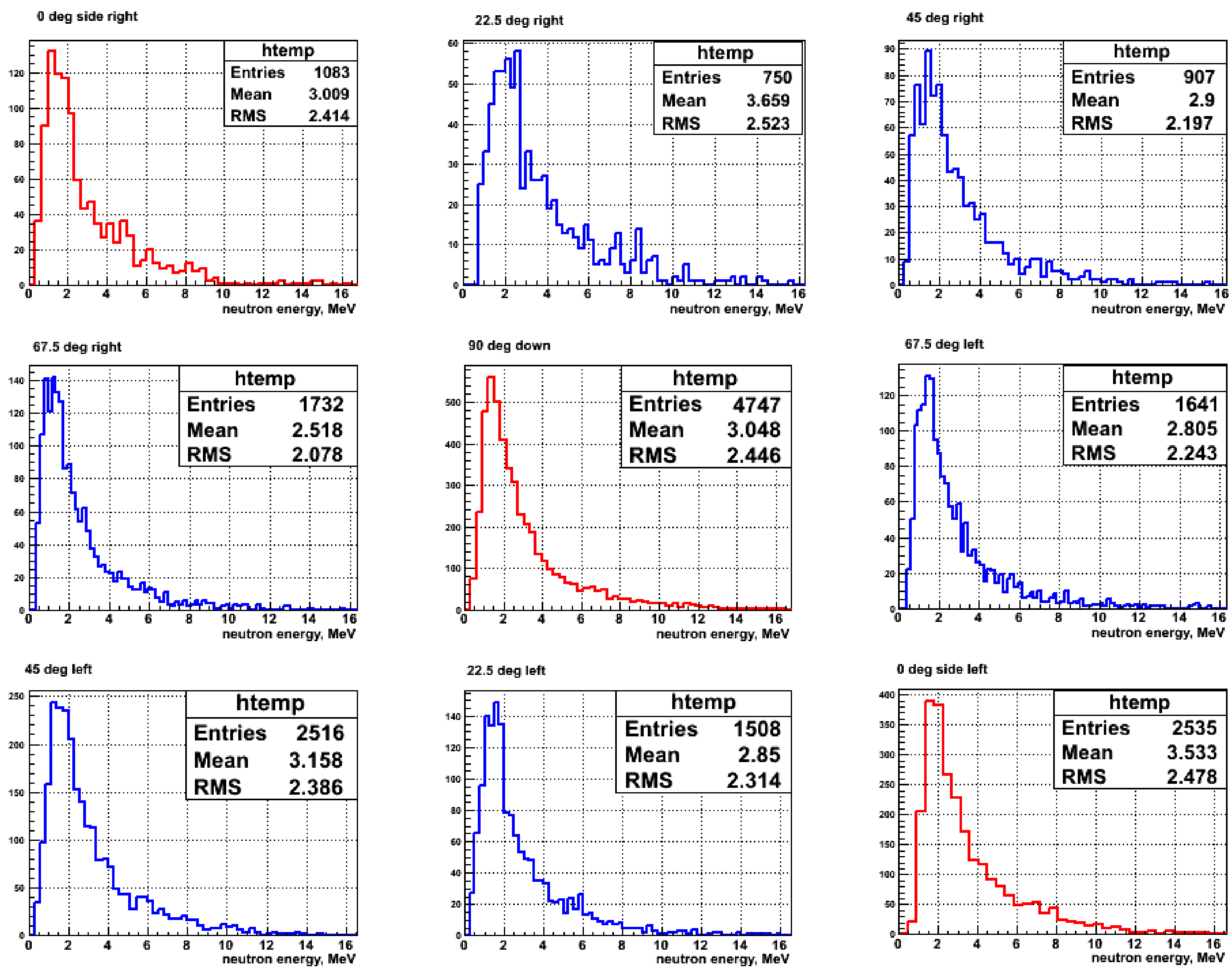

Fig. 4.36. Energy spectra of neutrons from the DU target. Polarized photon beam is in "up" configuration.

neutron emission asymmetry mostly in the detectors placed at 45 degrees with respect to the beam line. The data in the current energy bin did not show the expected degree of the asymmetry for the ∼25% polarized photon beam.

As the next step, the bin width was increased from 8 MeV to 6 MeV over the neutron energy spectrum and the relative asymmetry was calculated for each of the neutron detectors. The new bin content was added to the previous bin content (8 MeV to 7 MeV) and the corresponding point was plotted (see Fig. 4.37). Due to the increased number of neutrons in the bin 2 MeV wide, the statistical error reduced. However, the asymmetry in the neutron angular distribution did not improve much. Within statistical errors it was close to 1 which means that all detectors detected the neutrons at the same rates as would be in the case of unpolarized photons. The increase of the over all bin width was continued to the point where the whole energy spectrum of prompt neutrons was taken into account and the asymmetries for each neutron detector were observed to be close to 1.

Neutron asymmetry with eight energy bins

The test described above did not show the sign of the angular asymmetries of the prompt fission neutrons and, hence, the other approach was implemented. The neutron energy spectra were binned in eight channels with 1 MeV width of each bin. The asymmetry seen by each neutron detector for each energy bin was calculated and is presented in Fig. 4.38. As can be concluded no definitive sign of the neutron asymmetry was observed. The neutron asymmetries observed by the neutron detectors placed at 45 degrees with respect to the beam line and calculated using different ranges of neutron energy were close to 1 within statistical error bars.

Neutron asymmetry with four energy bins

Another attempt in the determination of the angular asymmetry of prompt fission neutrons was made. The neutron energy spectra were divided in 4 bins with bin width of 1 MeV. The main reason for the extension of the bin width and reduction in bin number was to increase the number of neutrons in each bin and, hence, reduce the uncertainty in the neutron asymmetry. The results on the neutron asymmetry in the case of the binning in four channels are presented in Fig. 4.39. It was observed that, as in the case with the running asymmetry data and eight channel binning data, no definitive asymmetry could be found. The values of the asymmetries in each energy bin in the case of detectors placed at 45 degrees with respect to the beam line were found to be close to 1 within statistical error bars.

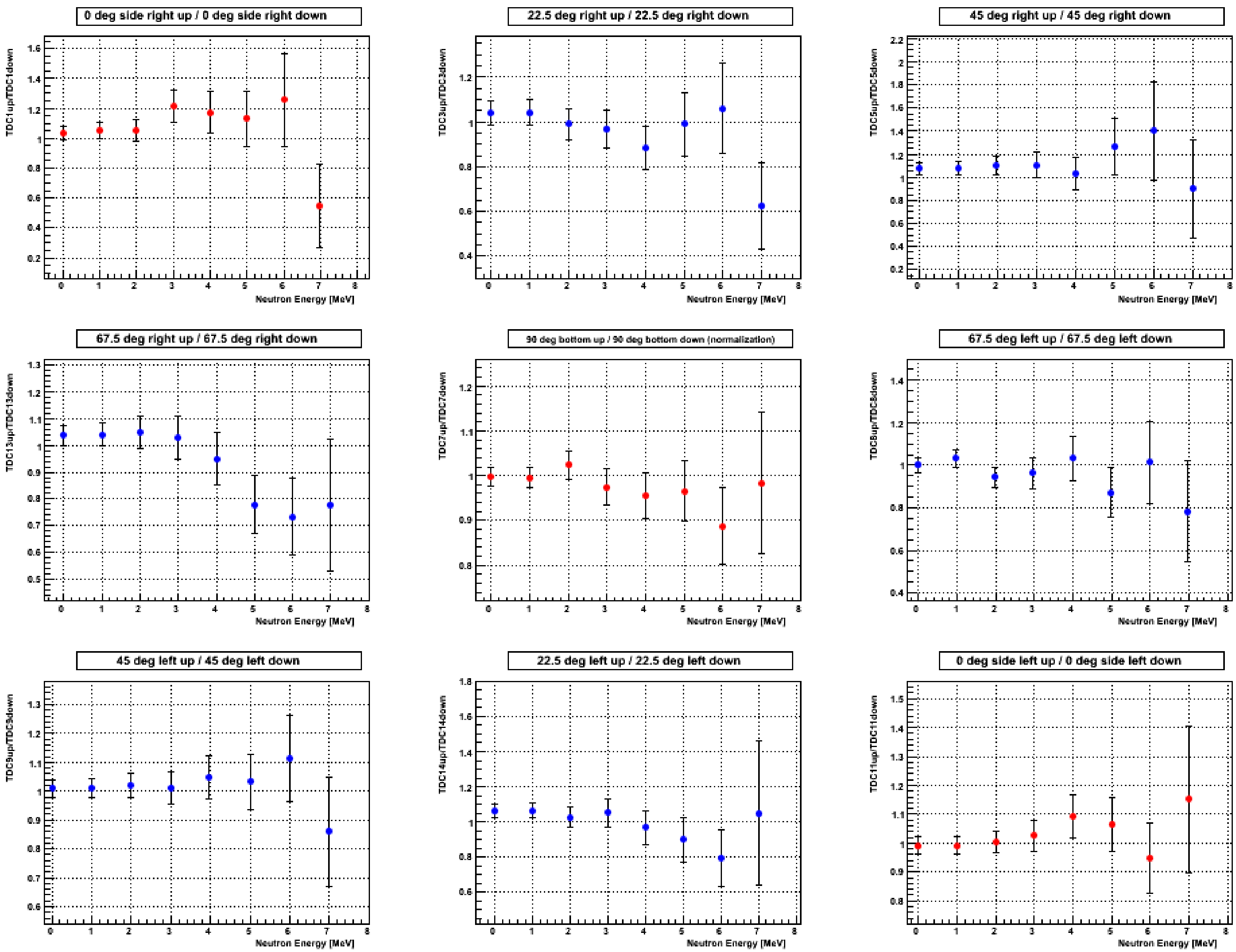

Fig. 4.37. Running asymmetry binned in 8 channels in case of the DU target.

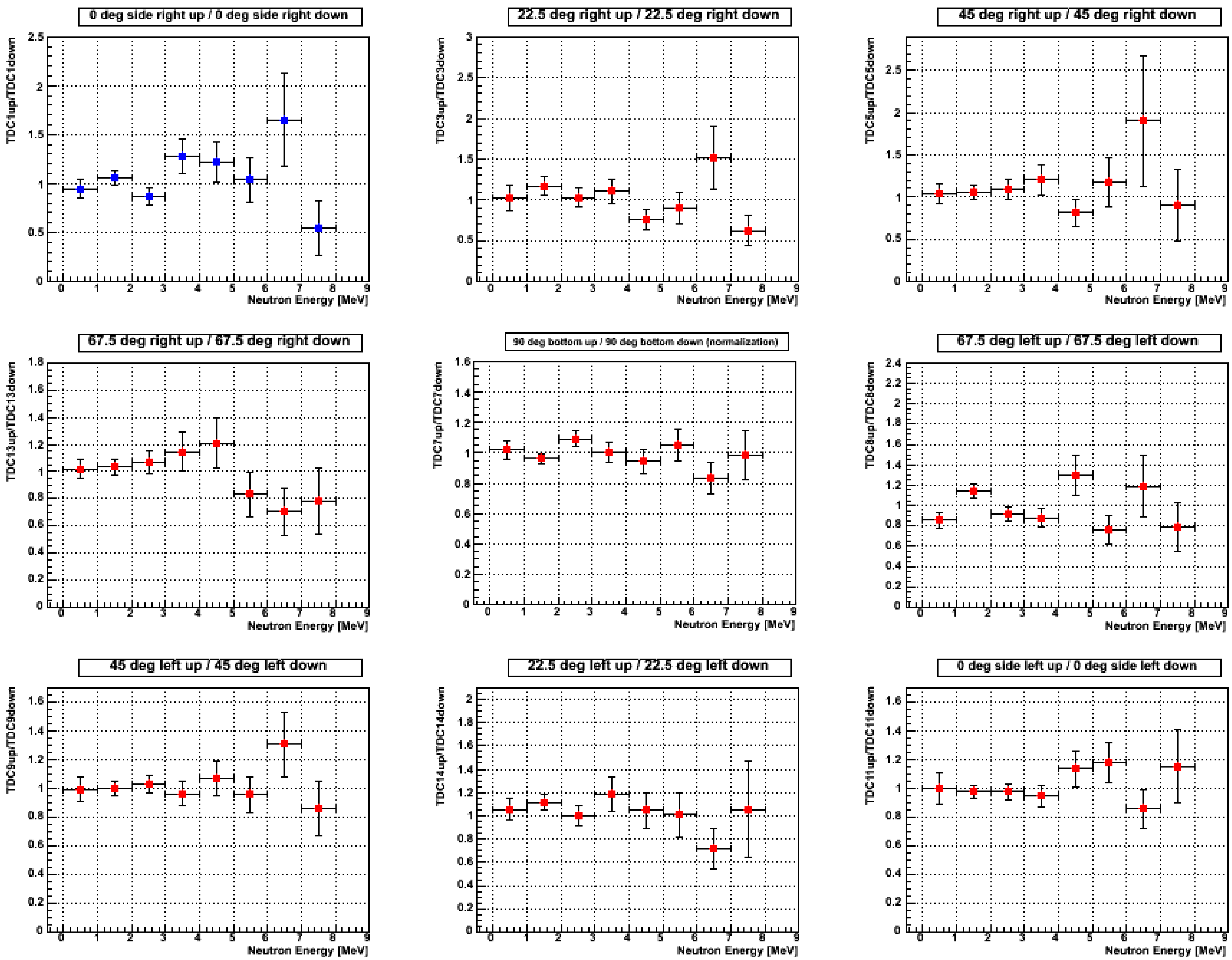

Fig. 4.38. The neutron asymmetry binned in eight channels in case of the DU target.

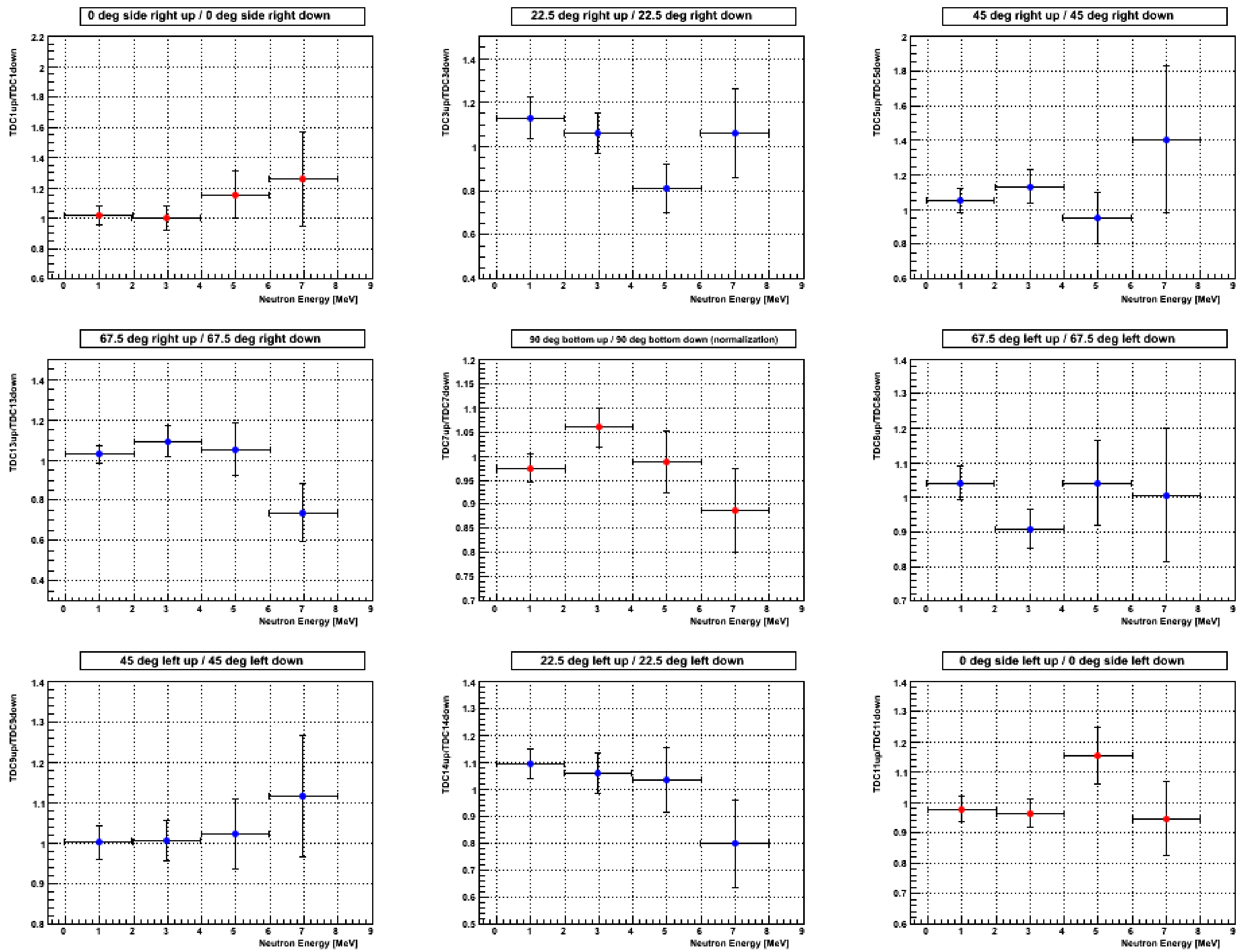

Fig. 4.39. The neutron asymmetry binned in four channels in case of the DU target.

Chapter 5

Summary and conclusions

In this work, we explored the effect of photofission of actinides with polarized and unpolarized photons. The angular distributions of prompt fission neutrons produced by photons both polarized and unpolarized were investigated using two different techniques. The first technique allowed us to observe the angular correlations of prompt neutrons produced in the process of photofission with unpolarized photons. The experiment on the two neutron correlations was performed at the Idaho State University High Repetition Rate Linear Accelerator. The energy of the photon beam was continuous with a maximum energy of 10.5 MeV which was chosen to prevent generation of two neutrons via the direct $(\gamma, 2n)$ reaction. The neutron detection system was composed of seven neutron detector paddles located in a plane at different distances from a target subtending different solid angles. Using the neutron time-of-flight technique, we obtained information on the energy distribution of prompt neutrons. It was also possible to retrieve information on the position of a neutron hit over the surface of a neutron detector because of the ability to read out the signal from the neutron detector at both ends. Software written for the two neutron correlation data analysis allowed us to separate true coincidence hits in the neutron time region detected by both PMT's of each detector from single hits seen by each PMT separately. The information on the distribution of the opening angles of two prompt fission neutrons detected by two different neutron detectors was extracted by taking a ratio of normalized correlated events over normalized uncorrelated events. The angular distribution of the opening angles was compared to the results of an experimentally based model of neutron induced fission which should provide qualitatively the same kinematic data as in the case of photofission with unpolarized photons. The experimental data on the two neutron opening angle qualitatively followed the results of the model with the main conclusion that the two prompt fission neutrons are most likely emitted either by two separate fission fragments (one neutron per fragment) or by one fission fragment resulting in greater yield of small opening angles around zero degrees. In this work, information obtained for the two neutron opening angle was observed only in the range up to 90 degrees because of the limitations implied by the detector setup. In order to explore the opening angles in a wider range, a modification of the detector system should be proposed. Future experiments probing the large opening angle kinematics are planned.

Theoretical calculations of the neutron angular asymmetry in the photodisintegration of the deuteron and the angular asymmetry of the fission fragments emission have shown that there are θ and ϕ-asymmetries in the reactions initiated by polarized photons. Also, experimental results obtained by many groups have shown that there is an angular anisotropy in the neutron emission and fission fragment angular distribution asymmetry. In the second part of this paper we proposed the idea of the detection of fissionable materials via investigation of angular distribution of prompt neutrons emitted by fission fragments from fissionable targets irradiated by linearly polarized photons. The results of the investigation of the deuteron photodisintegration were used in a technique to determine the degree of the photon beam polarization. They showed that there is an asymmetry in the neutron emission caused by linearly polarized photons. The value of the neutron asymmetry created in the photodisintegration reaction of deuterium was found to be around 25%. To estimate the polarization of the photon beam produced in the experiment, the polarization and angular distribution of bremsstrahlung photons for the given electron energy was obtained together with the energy spectrum of the bremsstrahlung photons. By implementing these distributions in Monte-Carlo calculations and applying the collimator geometry, it was possible to reconstruct the polarization spectrum of photons which produce the photodisintegration reaction, and thereby estimate the average polarization of photons. The neutron angular asymmetry observed in the experiments where one uses deuterium to determine the beam polarization degree, should be proportional to the value of the average polarization of bremsstrahlung photons. However, the analysis of the experimental data on the neutron asymmetry observed in the photofission reaction caused by the polarized photons showed no clear sign of the expected neutron asymmetry. Possible reasons for this could be the alternative reactions (γ, n) and $(\gamma, 2n)$ which have the thresholds of 6 MeV and 11.5 MeV, respectively. Polarized photons with energy of 25 MeV can produce neutrons in these reactions. These neutrons detected by neutron detectors together with the prompt neutrons produced in the reaction of photofission (γ, f) can smear out the asymmetry produced by the prompt neutrons only.

In summary, this work found clear evidence for kinematical correlations between fission fragments and prompt neutrons in the opening angle distribution of two neutrons in the photofission of depleted uranium. On the other hand, under the experimental conditions of these experiments, the signature for fission fragment − prompt neutron correlations for linearly polarized photons was consistent with zero.

Bibliography

1. Wagemans, C. *The Nuclear Fission Process* (CRC Press, Boca Raton, FL, 1991).

2. Vandenbosch, R. & Huizenga, J. R. *Nuclear Fission* (Academic Press, 1973).

3. Chadwick, J. Possible Existence of a Neutron. *Nature* **129,** 312–312 (Feb. 1932).

4. Meitner, L. & Frisch, O. R. Disintegration of Uranium by Neutrons: a New Type of Nuclear Reaction. *Nature* **143,** 239–240 (Feb. 1939).

5. Frisch, O. R. Physical Evidence for the Division of Heavy Nuclei under Neutron Bombardment. *Nature* **143,** 276–276 (Feb. 1939).

6. Karpov, A. V. *et al.* True ternary fission and quasifission of superheavy nuclear systems. *EPJ Web of Conferences* **17** (2011).

7. Tashkhodjaev, R. B. *et al.* A study of the almost sequential mechanism of true ternary fission. *Phys. Rev. C* **91** (Mar. 2015).

8. Brack, M. *Fundamentals of the Double-Humped Fission Barrier* (Notes of the Winter Course on Nuclear Theory for Applications held at the ICTP in 1978).

9. Preston, M. A. & Bhaduri, R. K. *Structure of the Nucleus* (Addison-Wesley Publishing Company, Inc, 1975).

10. DOE. *DOE Fundamentals Handbook: Nuclear Physics and Reactor Theory* (DOE-HDBK-1019/1-93, Jan. 1993).

11. Rubchenya, V. A. & Khlopin, V. G. The generalized model for the decription of prompt neutrons in the low energy fission. *Physics Procedia* **47,** 10–16 (2013).

12. Boikov, G. S. *et al. Z. Phys. A* **A 340** (1991).

13. Mueller, J. M. *et al.* Measurement of prompt neutron polarization asymmetries in photofission of U-(235,238), Pu-239, and Th-232. *Phys. Rev. C* **85,** 014605–1–014605–6 (Jan. 2012).

14. Baldwin, G. C. & Klaiber, G. S. Photo-fission in Heavy Elements. *Phys. Rev.* **71, 3** (1947).

15. Baldwin, G. C. & Klaiber, G. S. X-Ray Yield Curves for $\gamma - n$ Reactions. *Phys. Rev.* **73, 1156** (1948).

16. Goldhaber, M. & Teller, E. On Nuclear Dipole Vibrations. *Phys. Rev.* **74, 1048** (1947).

17. Brink, D. M. Individual Particle and Collective Aspects of the Nuclear Photoeffect. *Nucl. Phys.* **4,** 215–220 (Apr. 1957).

18. BNL. *Evaluated Nuclear Data File ENDF/B-VII.1* <`http://www.nndc.bnl.gov/sigma/`> (2011).

19. Private communication, Dale, Daniel. Ph.D., Professor at Department of Physiscs and Professor at Department of Nuclear Engineering, Idaho State University (921 South 8th Avenue, Pocatello, Idaho, 83209).

20. Kornilov, N. *Fission Neutrons: Experiments, Evaluation, Modeling and Open Problems* (Springer, 2015).

21. Carjan, N. & Rizea, M. Similarities between calculated scission-neutron properties and experimental data on prompt fission neutrons. *Phys. Lett. B* **747,** 178–181 (July 2015).

22. Talou, P., Becker, B., Kawano, T., Chadwick, M. B. & Danon, Y. Advanced Monte Carlo modeling of prompt fission neutrons for thermal and fast neutron-induced fission reactions on Pu-239. *Phys. Rev. C* **Vol. 83,** 064612–1–064612–2 (2011).

23. Jacobs, E. *et al.* Fragment mass and kinetic energy distribution for the photofission of 238-U with 12-, 15-, 20-, 30-, and 70-MeV bremsstrahlung. *Phys. Rev. C* **Vol. 20, No. 6,** 2249–2256 (1979).

24. Vogt, R. & Randrup, J. Application of Event-by-Event Fission Modeling with FREYA. *EPJ Web of Conferences* **Vol. 23, 08007** (2012).

25. Krane, K. S. *Introductory Nuclear Physics* (John Wiley and Sons, Inc., 1988).

26. Carjan, N., Talou, P. & Serot, O. Emission of Scission Neutrons in the Sudden Approximation. *arXiv:nucl-th/0701010v1* (Jan. 2007).

27. Pringle, J. S. & Brooks, F. D. Angular Correlation of Neutrons from Spontaneous Fission of Cf-252. *Phys. Rev.* **35,** 1563–1566 (Dec. 1975).

28. Sokolov, V. E. *et al.* Investigations of the Angular Dependences of Neutron-Neutron Coincidences from Cf-252, U-235, U-233 and Pu-239 Fission in Search of scission Neutrons. *Petersburg Nuclear Physics Institute, Gatchina, Leningrad District, 188300, Russia for ISINN-18* (May 2010).

29. Serebrov, A. P. Supersource of ultracold neutrons at the WWR-M reactor and the program of fundamental research in physics. *Crystallography Reports* **56,** 1230–1237 (7 Dec. 2011).

30. Pozzi, S. A. *et al.* Correlated Neutron Emission from Cf-252. *Nuclear Science and Engineering* **178,** 220–260 (2014).

31. Pozzi, S. A., Padovani, E., *et al.* MCNP-PoliMi: a Monte-Carlo code for correlation measurements. *NIM A* **513,** 550–558 (3 Nov. 2003).

32. Vogt, R. & Randrup, J. Event-by-Event Study of Neutron Observables in Spontaneous and Thermal Fission. *Phys. Rev. C* **87, 044621** (2011).

33. Vogt, R. *et al.* Event-by-Event Study of Prompt Neutrons from Pu-239(n,f). *Phys. Rev. C* **80, 044611** (2009).

34. Saint-Gobain Crystals. <`http://www.crystals.saint-gobain.com`> (17900 Great Lakes Parkway, Hiram, OH 44234).

35. Agostinelli, S. *et al.* Geant4 - a simulation toolkit. *NIM* **506,** 250–303 (July 2003).

36. Knoll, G. F. *Radiation Detection and Measurement* (John Wiley and Sons, Inc., 2010).

37. Press, W. H., Vetterling, W. T., Teukolsky, S. A. & Flannery, B. P. *Numerical Recipies in C++* (Cambridge University Press, 2002).

38. Pozzi, S. A. *et al.* The Effect of Neutron and Gamma Ray Cross Talk Between Plastic Scintillation Detectors. *ORNL/TM-2000/295* (Oct. 2000).

39. Private communication, Forest, Tony. Ph.D., Associate Professor at Department of Physics, Idaho State University (921 South 8th Avenue, Pocatello, Idaho, 83209).

40. Winhold, E. J. & Halpern, I. Anisotropic Photofission. *Phys. Rev.* **103,** 990 (1956).

41. Zhuchko, V. E. *et al.* Angular Distribution of Photofission Fragments of U-238 in the Region of the Isomer Shell. *Pis'ma Zh. Eksp. Teor. Fiz.* **24, No. 5,** 309–311 (1976).

42. Wilke, W. *et al.* Photofission of U-238 with Monochromatic Gamma Rays in the Energy Range 11-16 MeV. *Phys. Rev. C* **42, 2148** (1956).

43. Ratzek, R., Wilke, W., *et al.* Photofission with Linearly Polarized Photons. *Z. Phys. A* **308,** 63–71 (1982).

44. Kadmensky, S. G., Titova, L. V. & Khmelevskaya, O. S. Photofission Induced by Linearly Polarized Photons. *ISSN 1062 8738, Bulletin of the Russian Academy of Sciences: Physics* **Vol. 73, No. 6,** 831–834 (2009).

45. Tompkins, J. R. *Polarized Photofission Fragment Angular Distributions of Thorium-232 and Uranium-238* PhD thesis (University of North Carolina at Chapel Hill, 2012).

46. Mueller, J. M. *Prompt Neutron Polarization Asymmetries in Photofission of Isotopes of Thorium, Uranium, Neptunium, and Plutonium* PhD thesis (Duke University, 2013).

47. Haug, E. & Nakel, W. *World Scientific Lecture Notes in Physics, The elementary Process of Bremsstrahlung* (World Scientific Publishing Co. Pte. Ltd., 2004).

48. Jamnik, D. & Axel, P. Plane Polarization of 15.1 MeV Bremsstrahlung from 25 MeV Electrons. *Phys. Rev.* **117,** 194–206 (Jan. 1960).

49. Lanzl, L. & Hanson. *Phys. Rev.* **83** (1951).

50. Gluckstern, R. L., Jr., M. H. H. & Breit, G. Polarization of bremsstrahlung radiation. *Phys. Rev.* **90,** 1026–1031 (June 1953).

51. Laszewski, R. M., Rullhusen, P., Hoblit, S. D. & Lebrun, S. F. Enhanced Linear Polarization for Tagged Photon Beam. *NIM,* 334–342 (July 1985).

52. Motz, J. W. & Placious, R. C. Bremsstrahlung Linear Polarization. *Il Nuovo Cimento* **XV, N 4,** 571–598 (1960).

53. Olsen, H. & Maximon, L. C. Photon and electron polarization in high-energy bremsstrahlung and pair production with screening. *Phys. Rev.* **114,** 887–904 (May 1959).

54. Berg, U. E. P. & Kneissl, U. Recent Progress on Nuclear Magnetic Dipole Excitations. *Ann. Rev. Nucl. Part. Sci.* **37,** 33–69 (1987).

55. Matthews, J. L. & Owens, R. O. Accurate Formulae for the Calculation of High Energy Electron Bremsstrahlung Spectra. *Nuclear Instruments and Methods* **111,** 157–168 (1973).

56. Segre, E. *Nuclei and Particles, An Introduction to Nuclear and Subnuclear Physics* (W. A. Benjamin, INC, 1965).

57. Bethe, H. A. Moliere's Theory of Multiple Scattering. *Phys. Rev.* **89,** 1256–1266 (Mar. 1953).

58. Pedrotti, F. L., Pedrotti, L. S. & Pedrotti, L. M. *Introduction to Optics* (Pearson Education, Inc., 2007).

59. Berger, J. M. Deuteron Photodisintegration at Intermediate Energies. *Phys. Rev.* **94** (1954).

60. Partovi, F. *Ann. Phys* **Vol. 27, issue 1,** 79–113 (1964).

61. Likhachev, V. P. *et al.* Disintegration of the Deuteron by Tagged, Linearly Polarized Photons: Sensitivity of the Differential Cross Sections. *Braz. J. Phys.* **Vol. 27, No. 3** (1997).

62. Wissmann, F. *Compton Scattering. Investigating the Structure of the Nucleon with Real Photons.* (Springer, 2004).

63. Schumacher, M. Polarizability and of the nucleon and Compton scattering. *Prog. Part. Nucl. Phys.* **55,** 567–646 (2005).

Appendices

A.1 Normalization procedure

The combined neutron yield for the same pulse (sp) data set $Y^{sp}(\theta_{op})$ can be represented as a sum of the components:

$$\begin{aligned}
Y^{sp}(\theta_{op}) =& Y^{corr}_{nn}(\theta_{op}) + Y^{corr}_{\gamma n}(\theta_{op}) + Y^{corr}_{\gamma\gamma}(\theta_{op}) \\
&+ Y^{acc}_{nn}(\theta_{op}) + Y^{acc}_{\gamma n}(\theta_{op}) + Y^{acc}_{\gamma\gamma}(\theta_{op}) \\
&= Y^{SPD}(\theta_{op}) + Y^{corr}_{\gamma n}(\theta_{op}) + Y^{corr}_{\gamma\gamma}(\theta_{op}),
\end{aligned} \tag{i}$$

where

$$Y^{SPD}(\theta_{op}) = Y^{corr}_{nn}(\theta_{op}) + Y^{acc}_{nn}(\theta_{op}) + Y^{acc}_{\gamma n}(\theta_{op}) + Y^{acc}_{\gamma\gamma}(\theta_{op}). \tag{ii}$$

The total yield distribution of two uncorrelated events originating from two different pulses (dp) can be represented in the following way:

$$Y^{DPD}(\theta_{op}) = Y^{uncorr}_{nn}(\theta_{op}) + Y^{uncorr}_{n\gamma}(\theta_{op}) + Y^{uncorr}_{\gamma\gamma}(\theta_{op}). \tag{iii}$$

It is possible to extract the uncontaminated n-n correlated distribution as a function of the opening angle. First, correlated γ-n and γ-γ events need to be eliminated from $Y^{sp}(\theta_{op})$ data. This can be done by applying time cuts over the neutron time-of-flight spectrum. Then the net yield of correlated n-n can be calculated using Eq. (iv):

$$
\begin{aligned}
Y'(\theta_{op}) &= \frac{Y^{SPD}(\theta_{op}) - Y^{DPD}(\theta_{op})}{Y^{DPD}(\theta_{op})} \\
&= [Y^{corr}_{nn}(\theta_{op}) + Y^{acc}_{nn}(\theta_{op}) + Y^{acc}_{\gamma n}(\theta_{op}) + Y^{acc}_{\gamma\gamma}(\theta_{op}) \\
&\quad - Y^{uncorr}_{nn}(\theta_{op}) - Y^{uncorr}_{\gamma n}(\theta_{op}) - Y^{uncorr}_{\gamma\gamma}(\theta_{op})]/Y^{DPD}(\theta_{op}) \\
&= \frac{Y^{corr}_{nn}(\theta_{op})}{Y^{DPD}(\theta_{op})}.
\end{aligned}
\tag{iv}
$$

The proper normalization procedure and the procedure of extraction of the yields from two different data sets (same pulse data and different pulse data) was developed by [19] and done in the following way. The normalization factor for totally uncorrelated events was obtained by [19] in the form:

$$
N^{uncorr}_{norm} = \frac{\left(\frac{N_{wn}}{N_{wn}+N_{wno}}\right)^2}{4 \cdot \left(\frac{N_{wn}}{2}\right)}, \tag{v}
$$

where N_{wn} is the number of pulses out of the total number of pulses with only one neutron, N_{wno} is the number of pulses out of the total number of pulses with no neutrons. The number of neutron pairs obtained from the different beam pulses data is $N^{dp}_{wn} = 53422$ (see Fig. 2.14) and the number of pulses out of the total number of pulses with two neutrons detected by two neutron detectors in coincidence $N^{sp}_{wn} = 539$ (see Fig. 2.13). The factor of four in the denominator of Eq. (v) comes from the fact that the true two neutron coincidence rate is proportional to the photon intensity and the rate of random background coincidences is proportional to the photon intensity squared which is equal to four if we double the photon intensity. Taking coincidences between the events coming from the different pulses effectively doubles the photon beam intensity.

From the experimental data it was obtained that the total number of pulses that triggered our DAQ system $N_{tot} = 24692561$. The data analysis showed that we had $N_{wn} = 148216$ and $N_{wno} = 24544345$ and the normalization factor for the uncorrelated events was equal $N_{norm}^{uncorr} = 1.22 \cdot 10^{-10}$.

$$Y_{norm}^{SPD}(\theta_{op}) = Y^{SPD}(\theta_{op})/N_{tot} \tag{vi}$$

which is the normalized yield of two particle events obtained from the same beam pulse data analysis and

$$Y_{norm}^{DPD}(\theta_{op}) = Y^{DPD}(\theta_{op}) \cdot N_{norm}^{uncorr} \tag{vii}$$

which is the normalized yield of two particle events obtained from the different beam pulse data analysis and two neutron correlation function can be defined as (see Fig. 2.30):

$$Y_{corr}^{2n}(\theta_{op}) = \frac{Y_{norm}^{SPD}(\theta_{op})}{Y_{norm}^{DPD}(\theta_{op})}. \tag{viii}$$

A.2 Settings of delay/pulse generators DG535

We used two four channel digital delay/pulse generators DG535 in the experiment with the polarized photons to set the appropriate time delays between DAQ trigger signal and neutron signals produced by the neutron detectors. Both DG535 generators were triggered by the electron gun pulse which first arrived to channel #2 (from the top) of GG8000-01 octal generator and then supplied into the trigger connector of the generators. The following settings of the first DG535 gate and delay generator in the experiment with polarized photons were set:

(1) output $C \sqcap D$ was used as VME trigger. Plugged to "Control 1" input of

the VME crate.

(2) output $A \sqcup B$ was used as a fake stop. It was passed through a delay ORTEC 425A for the calibration purpose and plugged into one of the TDC channels.

Parameters of the other outputs are summarized below:

Channel $A = T + 110$ns, (load 50Ω, NIM, Normal);

Channel $B = A + 200$ns, (load 50Ω, NIM, Normal);

Channel $C = T + 3$ms201ns, (load 50Ω, VAR, A=+4V, offset=0.0V);

Channel $D = C + 30$ns, (load 50Ω, TTL, Inverted);

AB was set to HighZ, TTL and CD was set to 50Ω, TTL.

The settings of the second four channel digital delay/pulse generator DG535 are described below:

(1) Output $A \sqcap B$ was used as TDC module common start. Plugged to the upper "Gate comm".

(2) Output $A \sqcup B$ was supplied to the dual timer CAEN N93B and then used as common ADC start. Plugged to upper "Gate common".

T0 output was sent to the 4th channel of digital oscilloscope.

Parameters of the other outputs are summarized below:

Channel $A = T + 0$ns, (HighZ, TTL, Normal);

Channel $B = A + 270$ns, (HighZ, TTL, Normal);

Channel $C = T + 1$ms40μs, (HighZ, TTL, Inverted);

Channel $D = C + 50$ns, (HighZ, TTL, Inverted);

AB was set to 50Ω, NIM and CD was set to HighZ, TTL.